SETCOR
Conferences & Exhibitions

The SICT / Plasma Tech / Tribology 2023 International Joint Conferences

April 26 to 28, 2023, Lisbon, Portugal

Joint Conference Proceedings

DOI:
https://doi.org/10.26799/cp-sict-plasmatech-tribology-2023

Proceedings of the SICT / Plasma Tech / Tribology 2023 International Joint Conferences
Lisbon, Portugal – April 26 – 28, 2023
DOI: https://doi.org/10.26799/cp-sict-plasmatech-tribology-2023

Study of Wettability: Textured Surfaces Prepared with UV-Crosslinked Hybrid Solutions

Izabel Caldeira [1,2], Bérangère Toury[1], Mathieu Maillard[1], Valentin Gâté[2], Daniel Turover[2], Christian Brylinski[1]

[1] Laboratoire des Multimatériaux et Interfaces, UMR CNRS 5615
Univ Lyon, Université Claude Bernard Lyon 1, F-69622 Villeurbanne, France, izabel.moraes-caldeira@univ-lyon1.com ; berangere.toury-pierre@univ-lyon1.com ; christian.brylinski@univ-lyon1.fr ; mathieu.maillard@univ-lyon1.fr

[2] NAPA Technologies
382 rue Louis Rustin – Archamps Technopole, F-74160 Archamps, France,
izabel.moraescaldeira@napa-technologies.com ; valentin.gate@napa-technologies.com ; daniel.turover@napa-technologies.com

Abstract

The most recent developments around sol-gel processes to produce hybrid solutions (organic/inorganic) allowed us to find alternative routes to replace commonly used resins in nanoimprinting lithography processes. Another concern is the high temperatures needed in conventional reproduction processes, so the solution addressed in this work is using UV light to polymerize the coatings. Here, we present a study to compare the wetting of smooth and patterned sures. The latter has been obtained using a simple process to produce surfaces with superhydrophobic patterns via the Soft UV-NIL. The process involves the synthesis of a transparent hybrid silica-based solution that coats the substrate, structuration with micrometric patterns, and cross-linking under UV light. Finally, static and dynamic wetting characterizations were performed to understand wetting behaviors.

Keywords: nanoimprint, wettability, contact angle, hydrophobic, micropatterning, Wenzel, Cassie-Baxter, hybrid materials.

1. Introduction

Many applications require surface texturization. As primary examples, living organisms have evolved many strategies to change their color and appearance. Some of these characteristics are related to the physical and topographical properties of the surface, enabling color modifications or adding a surface functionalization such as hydrophobicity[1].

A surface to be considered superhydrophobic needs to present a water contact angle greater than or equal to 150°, combined with low surface energy (10 mN/m), which is defined as the surface free energy that quantifies the rupture of intermolecular bonds that occurs when a surface is created [2].

For instance [3], a patterned surface can provide hydrophobic behavior by mimicking [**Error! Reference source not found.**], the topographies of natural surfaces such as those mentioned above. Several techniques can be used to give a hydrophobic character to a surface, such as chemical vapor deposition (CVD) [4], plasma[5], direct laser interference (DLIP)[6], and, notably, nanoimprint lithography[7].

Chou proposed Nanoimprint lithography (NIL) [Figure 2] for the first time in 1995. NIL is a simple mechanical lithography technique in which a stamp or a template is pressed against a layer of deformable printed resist deposited on a substrate to create the template's outline. This low-cost technique is nowadays of the most used techniques for nanopatterning because it can easily and precisely reproduce micro and nanopatterning. [8]

DOI: https://doi.org/10.26799/cp-sict-plasmatech-tribology-2023

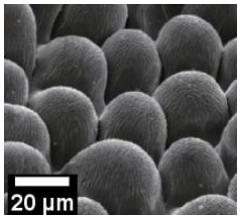

Figure 1: Scanning electron microscope image of Velvety leaves of a Dahlia flower with convex, structured cells.

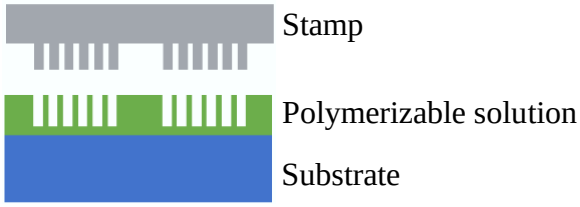

Figure 2: Principle of Nanoimprint technique.

It can be added that NIL can be achieved by using several development variations, such as Hot Embossing Lithography, UV-based Nanoimprint Lithography, roll imprint process, and laser-assisted direct imprint, among others [9]. In parallel, using soft lithography techniques, i.e., a replica impression using a silicone-based stamp, opened interesting alternative routes to replace the above-mentioned expensive and complex methods. However, two major challenges with the NIL technique are extending the size of the patterned area (from cm^2 to m^2) and achieving the patterning of complex surfaces (2.5-3D geometries), leading to hydrophobic surfaces. Another challenge is to replace thermally photopolymerizable resins with UV polymerizable ones, to broaden the variety of substrates which can be used and thus develop new applications.

This paper proposes a soft process to produce surfaces with super-hydrophobic patterns using the UV-NIL technique on hybrid solutions. To characterize and understand the hydrophobicity of the surfaces, wettability characterizations have been developed, and some modeling has been performed.

2. Wettability theories for material surface

A material's wettability is primarily characterized by a liquid's contact angle (CA) with respect to the solid surface (interfaces between the solid-liquid-gas phases). Further modeling and understanding of the adhesion and repellency characteristics on a surface have been mostly developed around the concepts describing the pinning of the droplet on the surface's patterns.

Four models for liquid spreading are commonly used: Young's, Wenzel, Cassie-Baxter, and Marmur models, which are schematized in the following Figure 3. [10]

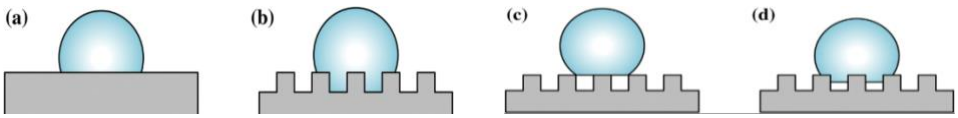

Figure 3: Four classic theoretical models: (a) Young; (b) Wenzel; (c) Cassie-Baxter; (d) Marmur model.

The Young model (a) describes the wettability of a flat or smooth surface in terms of the contact angle, the Wenzel model (b) is used to describe a surface in which droplets penetrate the rough structures leading to high adhesive forces, and the Cassie -Baxter Model (c) describes a rough surface that is non-penetrable by liquid droplets. The last model (d) is the intermediate state between Wenzel and Cassie, named Marmur Model [11]. These wettability models can evaluate a material's surface's hydrophilic/hydrophobic nature.

3. Experimental Techniques

The Soft UV-NIL is a well-known replication method that efficiently reproduces various patterns shapes and sizes, with lateral dimensions from a few hundred micrometers to the nanometer range. This technique differs from other classical lithography techniques since it uses UV light to cure a monomer, thus allowing the use of thermally sensitive substrates. Another important factor is the feasibility of using flexible and reusable molds instead of glass molds, which are more commonly used.

This technique demonstrates a high potential for application in solar cells, MEMS and NEMS, photovoltaics, micro-optics, wettability, etc. [12], [13].

A Soft UV NIL technology was chosen for our samples' surface structuration. Patterns (circles and squares) from 10-25µm in diameter were produced using a PDMS mold. Hybrid solutions with organic and inorganic components, solvent and photoinitiators were used to coat a transparent layer on a glass substrate. The solutions

DOI: https://doi.org/10.26799/cp-sict-plasmatech-tribology-2023

were deposited by spin coating and cured with UV light (HAMAMATSU Lightningcure LC8) for 10 minutes. The thickness of the coating obtained at the end of the process is around 40 µm, measured by a stylus profiler (DEKTAK 150). Static and dynamic wettability measurements (hysteresis angle) were performed with a goniometer equipped with a microscopic camera (KRUSS Easydrop FM40).

The dynamic wettability measurements were performed with the "ALPIN", a homemade device demonstrating a drop's angle to slide over a surface (water repellency angle). Anti-gel and anti-fog measurements were obtained with the BCBG bench created by NAPA, which shows the appearance of fog and ice and the total ice time of a coating.

4. Results and discussions

A first visual evaluation of the replicated patterns was performed by using a SEM (ZEISS Merlin Compact VP). Images confirmed the well-reproduced patterns, as shown in **Error! Reference source not found.**.

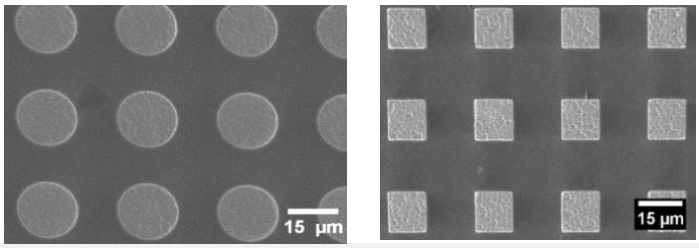

Figure 4: Examples of SEM images of textured surfaces with photocrosslinkable hybrid solution.

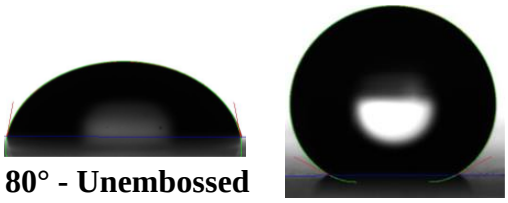

Figure 5: Contact angles for smooth and embossed surfaces based on a hybrid solution.

For contact angle measurements, the Figure 5 shows a significant increase in the contact angle value passing from a flat with 80° to a textured surface with 150° (average obtained between circles and squares with no significant difference in values between the two types), proving that the reproduction method is validate for reaching hydrophobic surfaces with CA of 150°.

The Owens, Wendt, Rabel, and Kaelble method is commonly used for calculating the surface free energy of solids. This method effectively separates interfacial interactions into polar and dispersive components. By applying the Owens-Wendt model, a surface free energy value of 45 mN/m is obtained for a flat surface. This value may be slightly less than the surface energy of an untreated sheet of glass, which is 49.7 mN/m, but it is still considered high. These high values can significantly reduce the mobility of liquid drops and make them more difficult to slide.

Using a goniometer with a microscopic camera, on a dynamic plateau, several tilts were reproduced up to an angle of 75° and measurements of the hysteresis angles were obtained as the difference between "forward" and "backward" sliding angles when the drop is subjected to variable inclination. Complementary measurements were also obtained using a home-made equipment by NAPA Technologies called "ALPIN". It uses lasers and photodetectors to capture the inclination angle value for which a drop starts to slide over the surface. The results are shown in Table 1.

Table 1: Values to Dynamic wettability

Dynamic wettability				
	Contact angle hysteresis		**Water repellency angle (ALPIN)**	
Coating	**Flat**	**Embossed**	**Flat**	**Embossed**
Glass	35 ± 4	na	14±5	na
Hybrid solution	19 ± 8	57 ± 19	26±1	35±5

Table 1 displays the findings that reveal a decrease in contact angle hysteresis on the hybrid coating in comparison to the bare substrate. Additionally, the hysteresis and repellency angle are heightened on textured surfaces. Overall, embossing enhances the static wettability behavior, while the dynamic wettability declines. The hindered movement of the drop can be attributed to the shallow water penetration of the patterning structures, creating significant resistance. As a result, we can conclude that our samples' wetting behavior aligns with the Marmur Model (as depicted in Figure 3d), representing an intermediate state between the Cassie and Wenzel models.

We've conducted a study on anti-frost measures, and the results are promising. Our hybrid solution, including a textured layer, has effectively delayed ice formation on treated glass surfaces. The delay time has increased significantly from 55 seconds to 10 minutes. We're dedicated to exploring the potential applications of this solution.

4. Conclusion and perspectives

In conclusion, we have produced surfaces with enhanced hydrophobic performance using UV-curable hybrid solutions with a fast and simple process. The wettability of the samples demonstrated so far behaves along the Marmur model. For reaching super-hydrophobic behavior, the surface energy must be further reduced, which may be pursued using other precursors or changing the topography of motifs. As for the understanding of the gliding properties of the textured surfaces, complementary analyses will be needed.

Acknowledgements

This work was carried out within the framework of the NAPASOL project, which received funding from the CIFRE (Industrial Agreements on Training through Research) program of the National Association for Technological Research (ANRT). This work is carried out by the company NAPA Technologies in collaboration with the University of Lyon 1 within the Multimaterials and Interfaces Laboratory (LMI).

References

1. C. Credi, M. Levi, S. Turri, and G. Simeone, "Stereolithography of perfluoropolyethers for the microfabrication of robust omniphobic surfaces," *Applied Surface Science*, vol. 404, pp. 268–275, May 2017, doi: 10.1016/j.apsusc.2017.01.208.
2. A. Mähringer, J. Rotter, and D. Medina, "Nanostructured and oriented metal–organic framework films enabling extreme surface wetting properties," *Beilstein Journal of Nanotechnology*, vol. 10, pp. 1994–2003, Oct. 2019, doi: 10.3762/bjnano.10.196.
3. W. Barthlott, M. Mail, B. Bhushan, and K. Koch, "Plant Surfaces: Structures and Functions for Biomimetic Innovations," *Nanomicro Lett*, vol. 9, no. 2, p. 23, 2017, doi: 10.1007/s40820-016-0125-1.
4. W. Tian *et al.*, "Fabrication of Transferable and Micro/Nanostructured Superhydrophobic Surfaces Using Demolding and iCVD Processes," *ACS Appl. Mater. Interfaces*, p. acsami.2c17613, Dec. 2022, doi: 10.1021/acsami.2c17613.
5. G. Primc and M. Mozetič, "Hydrophobic Recovery of Plasma-Hydrophilized Polyethylene Terephthalate Polymers," *Polymers (Basel)*, vol. 14, no. 12, p. 2496, Jun. 2022, doi: 10.3390/polym14122496.
6. A. I. Aguilar-Morales, S. Alamri, T. Kunze, and A. F. Lasagni, "Influence of processing parameters on surface texture homogeneity using Direct Laser Interference Patterning," *Optics & Laser Technology*, vol. 107, pp. 216–227, Nov. 2018, doi: 10.1016/j.optlastec.2018.05.044.
7. J. Durret, N. Frolet, and C. Gourgon, "Hydrophobicity and anti-icing performances of nanoimprinted and roughened fluoropolymers films under overcooled temperature," *Microelectronic Engineering*, vol. 155, pp. 1–6, Apr. 2016, doi: 10.1016/j.mee.2016.01.011.
8. M. Kwiat, S. Cohen, A. Pevzner, and F. Patolsky, "Large-scale ordered 1D-nanomaterials arrays: Assembly or not?," *Nano Today*, vol. 8, no. 6, pp. 677–694, Dec. 2013, doi: 10.1016/j.nantod.2013.12.001.
9. H. Lan, Y. Ding, H. Lan, and Y. Ding, "Nanoimprint Lithography," in *Lithography*, IntechOpen, 2010. doi: 10.5772/8189.
10. J. Zhao, X. Gao, S. Chen, H. Lin, Z. Li, and X. Lin, "Hydrophobic or superhydrophobic modification of cement-based materials: A systematic review," *Composites Part B: Engineering*, vol. 243, p. 110104, Aug. 2022, doi: 10.1016/j.compositesb.2022.110104.
11. A. Marmur, "Soft contact: measurement and interpretation of contact angles," *Soft Matter*, vol. 2, no. 1, pp. 12–17, 2006, doi: 10.1039/B514811C.
12. H. Lan and H. Liu, "UV-Nanoimprint Lithography: Structure, Materials and Fabrication of Flexible Molds," *Journal of nanoscience and nanotechnology*, vol. 13, pp. 3145–72, May 2013, doi: 10.1166/jnn.2013.7437.
13. "Imprint Lithography Equipment | SUSS MicroTec." https://www.suss.com/en/products-solutions/imprint-lithography (accessed May 04, 2023).

Proceedings of the SICT / Plasma Tech / Tribology 2023 International Joint Conferences
Lisbon, Portugal – April 26 – 28, 2023
DOI: https://doi.org/10.26799/cp-sict-plasmatech-tribology-2023

Reactive DCMS vs. reactive HiTUS of TiNbVTaZrHf-xN coatings

František Lofaj[1], Lenka Kvetková[1], Petra Hviščová[1],
Margita Kabátová[1] Tomáš Roch[2], V. Girman[1,3]

[1]Institute of Materials Research of the Slovak Academy of Sciences
Watsonova 47, Košice, Slovakia, flofaj@saske.sk
[2]Faculty of Mathematics, Physics and Informatics, Comenius University in Bratislava,
Mlynská dolina F2, Bratislava, Slovakia, tomas.roch@fmph.uniba.sk
[3]Faculty of Science, Pavol Jozef Šafárik University in Košice
Park Angelinum 9, Košice, Slovakia, vladimir.girman@upjs.sk

Abstract

The investigations of the reactive sputtering on the composite multicomponent TiNbVTaZrHf target in nitrogen containing sputtering atmosphere, in the plasma and of corresponding coatings revealed rapid target poisoning three regimes of working pressure changes and a significant suppression of hysteresis behaviour in both reference DC magnetron sputtering (DCMS) and relatively novel High Target Utilization Sputtering (HiTUS) cases. The obtained metallic coatings exhibited homogeneous distribution of all transition metal elements corresponding to high entropy alloys with bcc structure. The additions of nitrogen (x = nitrogen flow in sccm) caused slow decrease of deposition rates, increase of the nitrogen contents until stoichiometric limit, transition to fcc structure, increase of indentation hardness and modulus while preserving homogeneous structure corresponding to "high entropy nitrides". The critical nitrogen flows in DCMS and HiTUS, when stoichiometry was achieved, corresponded to the linear regime in working pressure changes and to the maximum mechanical properties. The highest hardness and indentation modulus values in the (near-)stoichiometric DCMS TiNbVTaZrHf-N coatings were around 40 GPa and 500 GPa, respectively, whereas the corresponding values in HiTUS TiNbVTaZrHf-N coatings were 33-35 GPa and ~400 GPa. The work demonstrated that reactive HiTUS is able to produce multicomponent nitride coatings analogous to high entropy nitrides and their properties can be controlled only via additions of nitrogen into sputtering Ar atmosphere. The mechanical properties of the studied HiTUS coatings were comparable to those achieved in similar DCMS coatings.

Keywords: reactive DC magnetron sputtering, reactive High Target Utilization Sputtering, multicomponent transition metal nitride coatings, target poisoning, hysteresis behaviour, mechanical properties.

1. Introduction

High entropy metal sub-lattice stabilized nitride coatings (sometimes called "high entropy nitrides") based on multicomponent refractory transition metals (TM = Ti, Nb, V, Ta, Zr, Hf**)** are promising candidates for extreme conditions due to their high thermal, mechanical and corrosion properties [1]. Their history is, however, relatively brief. Possibly the first 4-component TM+Cr coatings Hf-Ti-Zr-V-Cr-N were produced by reactive magnetron sputtering in 2011 [2]. The first TM only Ti-V-Zr-Nb-Hf-N and Ti-Zr-Nb-Hf-Ta-N coatings were deposited by the reactive arc in 2012-2013 [3-6]. The first 6-TM Ti-V-Zr-Nb-Hf-Ta-N coatings were produced by reactive arc in 2014 [7] and in 2015 [8], respectively. The studies on analogous coatings produced by High Power Impulse Magnetron Sputtering (HiPIMS) and/or High Target Utilization Sputtering (HiTUS) were very limited up to now. According to our current information, HiPIMS was successfully applied to AlCrTiVZr-N [9-10] and TiZrNbTFe-N systems [11] resulting in higher densities and hardness values than in the reference DCMS coatings. Reactive HiTUS-made TiNbVTaZrHf-N coatings were only recently described in our work [12]. It was found out that hysteresis behavior expected from target poisoning during reactive sputtering was greatly suppressed. It was rather surprising because the above TMs belong into a group of strong nitride formers [13] and therefore, well pronounced target poisoning could be expected to influence the process of reactive sputtering. The absence of hysteresis was related to low sensitivity of HiTUS to poisoning. However, our later investigations on the same system in DCMS also found suppression of hysteresis [14]. It was therefore concluded that the sputtering occurred only in poisoned regime.

DOI: https://doi.org/10.26799/cp-sict-plasmatech-tribology-2023

The aim of the current work was to compare the processes of reactive sputtering in the case of relatively novel High Target Utilization Sputtering (HiTUS) method with the case of DCMS in the deposition of multicomponent TiNbVTaZrHf–N coatings. The main tasks of the work involved the comparisons of the reactive processes - target poisoning, hysteresis behavior and pressure changes in the plasma, as well as resulting coating structure, composition, stoichiometry and mechanical properties. The work is based on the results reported in [12] and [14].

2. Experimental Procedure

2.1. Coating deposition

The reactive HiTUS TiNbVTaZrHf-xN coatings were deposited using TiNbVTaZrHf target with a diameter of 76.2 mm in an Ar atmosphere with the variable nitrogen flows, x, by High Target Utilization Sputtering (model S500, Plasma Quest Ltd., UK) on polished (0001) sapphire and (111) Si wafers. The constant deposition parameters involved RF power on the remote plasma source - 1800W; RF power on the target - 700W; RF bias on the substrate - 5W (corresponding to DC bias of -45 V); substrate temperature - 300^{O}C; Ar flow of 120 sccm resulting in an initial working pressure ~0.76 Pa, target–substrate distance - 17 cm and the deposition time - 90 min. The only variable of the reactive HiTUS included additions of nitrogen, x, in the range from 0 sccm up to 10 sccm in 2 sccm steps, which caused an increase in the working pressure to 0.82 Pa. The coating thicknesses were in the range 1.2 – 1.7 μm.

The reference reactive DCMS coatings were from the same target in the unbalanced DC magnetron sputtering system (model Cryofox 500, Polyteknik, Denmark). Although the size of the deposition chamber, pumping rate, power density on the target, substrate-target distance, etc., were different from those in the HiTUS system, the deposition parameters were optimized to provide fair comparison with the HiTUS coatings. They involved: DC power on the target - 500 W; substrate temperature - 500^{o}C, floating bias, target-substrate distance - 7 cm, 20 sccm Ar flow resulting in 0.53 Pa initial working pressure and deposition time - 20 min. The nitrogen additions into the Ar atmosphere varied from 0 sccm up to 11 sccm increased in the working pressures to 0.68 Pa (at 11 sccm N_2). The obtained coating thicknesses were ≥1 μm.

Hysteresis behavior during reactive DCMS and HiTUS were investigated under identical conditions (including substrate temperature) via measurement of pressure changes during a gradual nitrogen flow increase/decrease cycle. The reference pressures in the chamber during the nitrogen cycle were obtained without DC power.

2.2. Structure, chemistry and nanoindentation

The coating structure observations were performed on the fractured cross sections of the coatings on Si substrates using scanning electron microscopy (SEM, models Auriga Compact and EVO MA15, Zeiss, Germany). Their chemical compositions were primarily measured by Energy Dispersive Spectroscopy (EDS) with an SDD detector (Oxford Instruments, 80 mm^2).

The details of coating structures were investigated by high resolution transmission electron microscopy (TEM, model JEM 2100F, Jeol, Japan) on thin foils. The foils were prepared from two as-deposited coatings glued together using a standard procedure involving polishing, dimpling, and ion milling.

The measurements of mechanical properties of all coatings were based on nanoindentation with diamond Berkovich tip (G200, Agilent, USA) and Continuous Stiffness Method for Thin Films (CSMTF) method [15] in constant strain rate mode (0.05 s $^{-1}$) with the amplitude of the sinusoidal signal of 2 nm and frequency of 45 Hz. The measurements were performed on two sets of 16 indents up to a predefined depth of 800 nm in two locations approximately 2 mm apart on each coating. Further details can be found in [12]

3. Results and Discussion

3.1. Processes at the target and in the plasma

At first, the processes occurring on the target surfaces and in the corresponding plasma during reactive sputtering in DCMS and HiTUS were investigated. Despite no changes were visible by naked eye, EDS analysis confirmed the presence of relatively high amount of nitrogen in the surface layer on the target surfaces (Fig. 1) indicating their poisoning. It agreed with the fact that all TMs in the targets belong to strong nitride formers.

DOI: https://doi.org/10.26799/cp-sict-plasmatech-tribology-2023

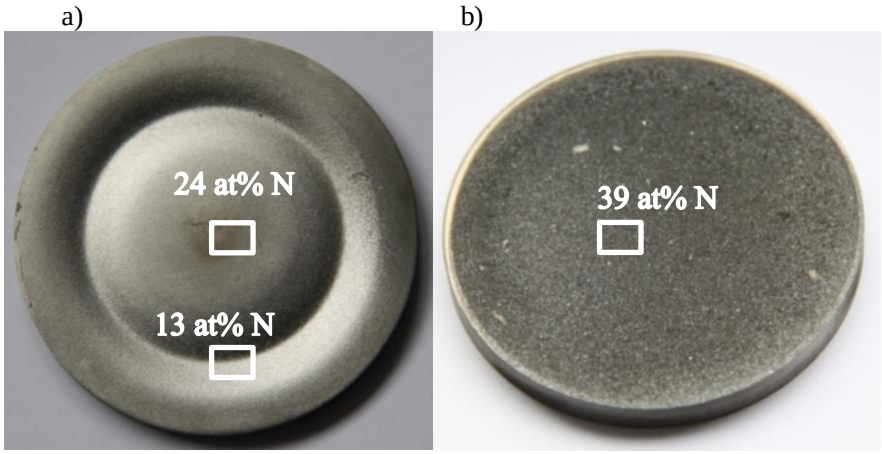

Fig. 1: The appearance of the targets after reactive a – DCMS (500 W, 8 sccm N_2, 20 min) and b – HiTUS (1800/700 W, 15 sccm N_2, 15 min). Nitrogen concentrations indicating target poisoning were determined by top-view EDS from the areas of around 400 x 600 mm^2.

The changes of the working pressure in the plasma discharge in comparison with the pressure without discharge, Δp, which corresponds to the amount of nitrogen consumed in the formation of nitrides on the surface of the target substrate and chamber walls, are shown in Fig. 2 during the increase/decrease of nitrogen flow cycle. Relatively small differences between both parts of the cycle suggested that hysteresis behaviour was significantly suppressed both in DCMS and HiTUS. Moreover and despite small variations, three regimes of nitrogen consumption were identified in both cases [12, 14]:

1. linear regime with increasing nitrogen until a maximum at a certain critical nitrogen flow. This regime seemed to be controlled by the amount of nitrogen and the maximum occurs when the amount of active TMs (on the target surface and in the plasma or substrate) are equal;
2. Non-linear transition with the decreasing nitrogen consumption
3. Gradual decrease and saturation of the consumption approaching zero.

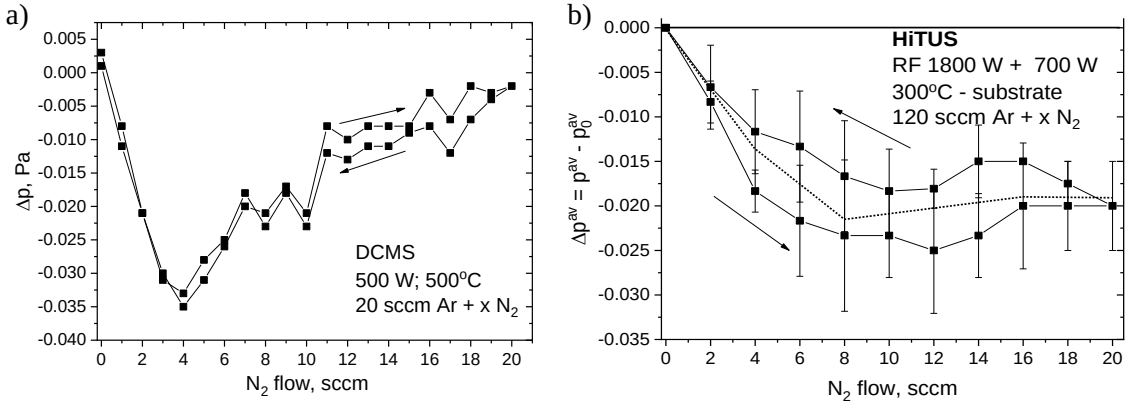

Fig. 2: Working pressure difference, □p, corresponding to nitrogen consumption during reactive a – DCMS and b – HiTUS, during the increase/decrease of nitrogen flow cycle. Negligible difference between the curves during nitrogen cycle indicates suppression of hysteresis behavior [12, 14].

The transition and saturation regimes can be attributed to the reduction of the supply of transition metals across the poisoned layer on the surface of the target. Further details and a phenomenological model of reactive sputtering without hysteresis based on the sputtering only in the poisoned regime can be found in [14].

3.2. Coating preparation

Two series of coatings with different nitrogen flows, x, were deposited using DCMS and HiTUS, respectively (Tab. 1). The coating thicknesses were measured on the fractured cross sections in SEM.

DOI: https://doi.org/10.26799/cp-sict-plasmatech-tribology-2023

Table 1: The list of the studied TiNbVTaZrHf-xN coatings deposited using a - reactive DCMS and b - reactive HiTUS.

a)

DCMS coatings	N_2 flow, sccm	Thickness, nm
dc-6TM-0N*	0	3350/3100*
dc-6TM-2N	2	2840
dc-6TM-3N	3	2600
dc-6TM-5N*	5	1965/2390*
dc-6TM-7N	7	1400
dc-6TM-9N	9	1120
dc-6TM-11N	11	975

b)

HiTUS coatings	N_2 flow, sccm	Thickness, nm
HT-6Me-0N	0	1705
HT-6Me-2N	2	1780
HT-6Me-4N	4	1610
HT-6Me-6N	6	1620
HT-6Me-8N	8	1420
HT-6Me-10N	10	1210

3.3. Coating structure, composition and mechanical properties

SEM, TEM as well as X-ray diffraction investigations in [12, 14] showed that the DCMS TM coating without nitrogen exhibited (110) bcc textured columnar structure whereas that of HiTUS coating was amorphous. The reason seems to be related to lower substrate temperature in HiTUS (300ºC) than in DCMS (500ºC). After 2 sccm nitrogen additions, mixed phase compositions were observed and at the flow above 4 sccm, textured fcc structures consisting of columnar grains with the (111) and later (200) orientations were present in both types of coatings. Fig.3a and 3b show the changes of coating stoichiometry at different nitrogen flows. Moreover, EDS mapping illustrated the absence of TM segregation and homogeneous distributions of all TMs and nitrogen in all coatings regardless of deposition technique. Thus, the deposited coatings can be attributed to the class of ceramics with metallic sub-lattice stabilized by high entropy [1, 16]. Despite limited accuracy of semi-quantitative EDS measurements of light elements, the results clearly demonstrated rapid increase of the nitrogen concentrations in the coatings during flow increase up to the stoichiometric limit and then a transition to saturation. The transition part was more pronounce in HiTUS than in DCMS case but the dependencies were principally identical. The flows when saturation was achieved reasonably well agreed with the maxima of Δp at the end of linear regime of nitride consumption. (see Fig. 2a and 2b).

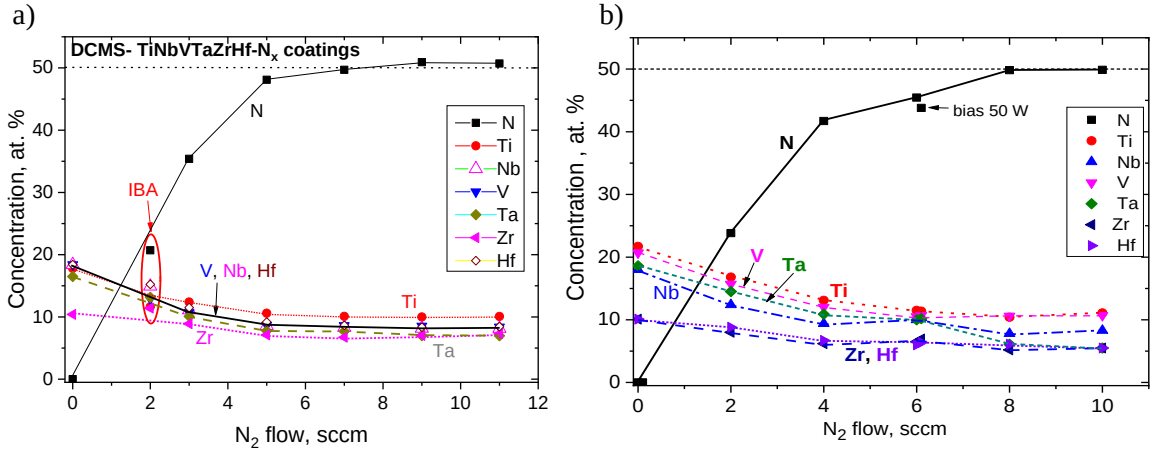

Fig. 3: The average concentrations of nitrogen and transition metals a function of N_2 flow into Ar atmosphere in a - DCMS and b – HiTUS TiNbVTaZrHf-xN coatings [12, 14].

Fig. 4a and 4b illustrate indentation hardness and indentation modulus at different nitrogen concentrations in the DCMS and HiTUS coatings, respectively. In both cases, nitrogen additions caused rapid and approximately linear increase of the values of corresponding mechanical properties. When nitrogen concentrations exceeded around 45 at% and approached stoichiometric limit, saturation occurred. Further nitrogen flow increase caused only the degradation. The difference between DCMS and HiTUS coatings was only in slower degradation in the latter case, most probably due to lower relative flow changes in much larger HiTUS chamber. The degradation was attributed to the increase of the working pressure due to the excess amount of unreacted nitrogen. It would correspond to the third stage in the Δp changes and increase of the number of scattering events of the sputtered species on their way toward the substrate. Lower mechanical

properties could be explained by lower densities of the coatings due to reduction of the energy of the impinging species.

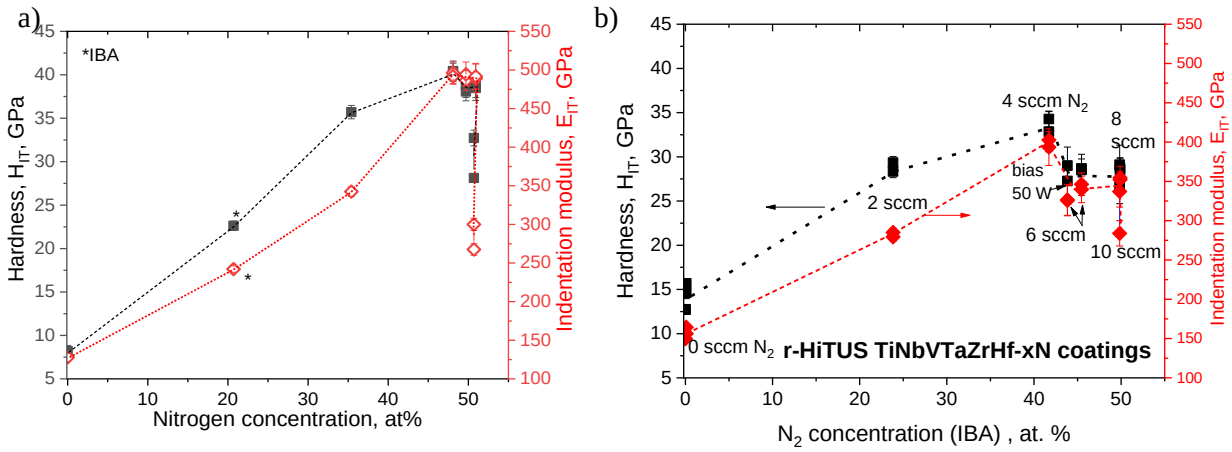

Fig. 4: The average values of indentation hardness and indentation moduli in a - DCMS and b – HiTUS TiNbVTaZrHf-N coatings a function of N_2 concentrations [12, 14].

The highest values of hardness in the DCMS coatings were around 40 GPa whereas 33-35 GPa was achieved in the HiTUS-made coatings. Indentation moduli showed similar differences – 500 GPa vs. 400 GPa, respectively. However, despite that, reactive HiTUS was able to produce multicomponent TM-nitride coatings with the mechanical properties approaching those of the DCMS coatings.

4. Conclusions

The work confirmed that reactive HiTUS can produce homogeneous multi-element transition metal solid solution nitride coatings analogous to high entropy nitrides with the structure and mechanical properties similar to those obtained by reactive DCMS. Despite high affinity of all TM to nitrogen, reactive HiTUS and DCMS processes occurred without hysteresis behaviour which was attributed to the reactive sputtering occurring only in the poisoned regime. As a result and regardless of the technique of sputtering (DCMS or HiTUS), the coating (nitrogen) stoichiometry and mechanical properties can be controlled only by the amount of nitrogen in the Ar sputtering atmosphere without a need for the feedback prevention of target poisoning.

Acknowledgements

This work was supported by the International Visegrad Fund [project JP39421, V4-Japan Joint Research Program], by the Slovak Research and Development Agency [projects APVV APVV-21-0042] and by the Research Agency of the Ministry of Education, Science, Research and Sport of the Slovak Republic [project VEGA 2/0083/23]. The contributions of Maksym Lisnichuk (P.J. Šafárik University) to TEM observations and Alexandra Kovalčíková and Marek Vojtko to SEM studies are also acknowledged.

References

1. A.Kirnbauer, A. Kretschmer, et al., “Mechanical properties and thermal stability of reactively sputtered multi-principal-metal Hf-Ta-Ti-V-Zr nitrides,” *Surf. Coat. Technol.*, vol. 389, e 125674, 2020. doi:10.1016/j.surfcoat.2020.12
2. S.-C. Liang, Z.-C. Chang, et al., “Structural and mechanical properties of multi-element (TiVCrZrHf)N coatings by reactive magnetron sputtering,”. *Appl. Surf. Sci.* vol. 258, pp. 399 – 403, 2011. doi: 10.1016/j.apsusc.2011.09.006
3. V. Braic, M. Balaceanu, et al., “Characterization of multi-principal-element (TiZrNbHfTa)N and (TiZrNbHfTa)C coatings for biomedical applications,” *J. Mech. Behav. Biomed. Mat*., vol. 10, pp. 198-205, 2012**.** doi: 10.1016/j.jmbbm.2012.02.020
4. O. V. Sobol’, A. A. Andreev, et al., “Reproducibility of the single phase structural state of the multielement high_entropy Ti–V–Zr–Nb–Hf system and related superhard nitrides formed by the vacuum arc method,” *Techn. Physics Lett., vol.* 38, pp. 40–47, 2012. doi: 10.1134/S1063785012070127

5. V. Braic, A. Vladescu, et al., "Nanostructured multi-element (TiZrNbHfTa)N and (TiZrNbHfTa)C hard coatings," *Surf. Coat. Technol*., vol. 211, pp. 117-132, 2012. doi: 10.1016/j.surfcoat.2011.09.033
6. A.D. Pogrebnjak, I.V. Yakushchenko, et al., "The effects of the deposition parameters of nitrides of high-entropy alloys (TiZrHfVNb)N on their structure, composition, mechanical and tribological properties," *J. Superhard Mate*r., vol. 35, pp. 356-368, 2013. doi: 10.3103/S106345761306004X
7. S. N. Grigoriev, O.V. Sobol, et al., "Tribological characteristics of (TiZrHfVNbTa)N coatings applied using the vacuum arc deposition method," *J. Friction Wear, vol.* 35, pp. 359–364, 2014. doi: 10.3103/S1068366614050067
8. A. D. Pogrebnjak, I. V. Yakushchenko, et al., "Influence of implantation of Au– ions on the microstructure and mechanical properties of the nanostructured multielement (TiZrHf VNbTa)N coatings", *Phys. Solid State*, vol. 57, 1559–1564, 2015. doi: 10.1134/S1063783415080259
9. Y. Xu, G. Li, et al., "Effect of bias voltage on the growth of super-hard (AlCrTiVZr)N high-entropy alloy nitride films synthesized by high power impulse magnetron sputtering," *Appl. Surf. Sci*., vol. 564, e150417 2021. doi: 10.1016/j.apsusc.2021.150417
10. Y. Xu, G. Li, and Y. Xia, "Synthesis and characterization of super-hard AlCrTiVZr high-entropy alloy nitride films deposited by HiPIMS," *Appl. Surf. Sci*., vol. 523, e146529, 2020. doi: 10.1016/j.apsusc.2020.146529
11. S.K. Bachani, C.-J. Wang, et al., "Fabrication of TiZrNbTaFeN high-entropy alloys coatings by HiPIMS: Effect of nitrogen flow rate on the microstructural development, mechanical and tribological performance, electrical properties and corrosion characteristics," *J. Alloys Compounds,* vol. 873, e159605, 2021. doi: 10.1016/j.jallcom.2021.159605
12. F. Lofaj, L. Kvetková, et al., "Reactive HiTUS TiNbVTaZrHf-N_x coatings: structure, composition and mechanical properties," *Materials*, vol. 16, e563, 2023. https://doi.org/10.3390/ma16020563
13. E. Lewin, "Multi-component and high-entropy nitride coatings - a promising field in need of a novel approach," *J. Appl. Phys.,* vol. 127, e160901, 2020. doi: 10.1063/1.5144154
14. F. Lofaj, P. Hviščová, et al., "Reactive DC magnetron sputtered TiNbVTaZrHf-xN coatings: hysteresis behavior vs. coating structure and mechanical properties," under review, *Surf. Coat. Technol*., 3-2023.
15. J. Hay and B. Crawford, "Measuring substrate independent modulus of thin films," *J. Mater. Res.,* vol. 26, 727-738, 2011. doi: 10.1557/jmr.2011.8
16. J.M. Schneider, How high is the entropy in high entropy ceramics?, *J. Appl. Phys*., vol. 130, e150903, 2021. doi: 10.1063/5.0062523

Proceedings of the SICT / Plasma Tech / Tribology 2023 International Joint Conferences
Lisbon, Portugal – April 26 – 28, 2023
DOI: https://doi.org/10.26799/cp-sict-plasmatech-tribology-2023

Development Process, Structure and Performance Parameters of a Shielded 433 MHz Plasma Jet with 600W

H. Heuermann [1], St. Terbrack [1]
[1] Institute of Microwave and Plasma Technology (IMP),
University FH Aachen, Aachen, Germany, heuermann@fh-aachen.de

Abstract

In this article, we introduce the world's first 433 MHz plasma jet that has been successfully developed. We begin by explaining the current state of the art at this frequency. Next, we present the hot-S measuring station that was specifically built for the development of this plasma jet. It is only through the use of such a measuring station that plasma sources in the microwave range can be developed with high quality. Finally, we provide a detailed account of the development of this plasma jet, accompanied by pictures of different plasmas for a comprehensive understanding.

Keywords: Microwave plasma, plasma jet, hot-S parameter, microwave ignition, torch, atmosphere plasma, chamber plasma, plasma treatment

1. Introduction

Plasma jets have traditionally been used for surface activation and welding processes, predominantly operating on AC signals in the lower MHz range. However, recent advances have introduced plasma jets in the GHz range, which rival lasers in many applications [1]. This paper presents a plasma jet that falls between these two classes, operating at 433 MHz. While some research has been conducted on GHz plasma jets [2-3], this particular frequency has not been extensively studied.

This new plasma source uses high-frequency electromagnetic fields to generate and sustain a plasma discharge, producing reactive species and intense plasma densities. It has great potential for surface modification, thin film deposition, and plasma etching, but its capabilities have not yet been fully investigated.

Before delving into the development of the 433 MHz plasma jet, this paper outlines the importance of constructing a hot-S measuring station as the primary measuring equipment. Such a station is essential for developing high-quality plasma sources in both the MHz and GHz range and verifying their efficiency. The measurements obtained from this station form the basis for necessary field simulations.

This article covers the initial part of the development process for creating an automatic ignition using internal coaxial line components with a high-voltage construction. To ensure power matching during operation via the same unit, the frequency needs to be slightly adjusted, requiring a semiconductor amplifier. Measuring the plasma at full power (600 W) and 433 MHz requires a specially built hot-S-parameter for the plasma jet development. Matching elements for the operation were developed based on plasma modeling of the spatially distributed electrical conductivity. However, the ignition network is affected, and simulation optimizations for both operating points and optimum operating frequencies are necessary for further work. The continuous operation should be at 433 MHz for legal approval reasons. Shielding is also necessary to protect users from the excessive radiation of the large plasma achieved. The article concludes with information on the applications of the 433 MHz plasmas generated.

2. Hot-S Parameter Measurement

2.1. Overview Hot S-Parameter Measurement Technique

A commonly used and precise method for measuring RF amplifiers is the hot S-parameter or Large-Signal S-parameter technique [4]. This technique is designed to explain the interaction of nonlinear devices in realistic operating conditions [5]. It has also been employed in measuring microwave plasma [6]-[8] that involves ionizing gas through microwave energy. However, solid-state amplifiers used in the process limit the power coupled into the plasma to less than a kilowatt, making it impractical for industrial applications where processing speed is proportional to plasma power. To address this limitation, a novel hot S-parameter

DOI: https://doi.org/10.26799/cp-sict-plasmatech-tribology-2023

measurement system for 433 MHz applications has been developed. This system characterizes and accurately describes the device under test (DUT) during operating conditions by measuring its input matching hot-S11 and transmission hot-S21 at 433 MHz center frequency and 60 MHz bandwidth. It is essential to consider this when modeling the equivalent circuit of the DUT and designing a matching network to improve efficiency. Additionally, monitoring the S-parameters over time can help control the system. The system is particularly ideal for industrial use, facilitated by its utilization of a self-manufactured semiconductor power amplifier (PA) that operates at 433 MHz and delivers 800 W of power. Additionally, this measurement system has already been utilized to develop a novel 600 W self-igniting microwave plasma jet (MPJ) for industrial applications.

2.2. Measurement Hardware Set-Up

In Figure 1, the hot-S is depicted and comprises a power signal generator (1), a test-set (5) that includes a power amplifier, an isolator, two directional couplers, and a DUT-connector, a 1 kW power load (6), attenuators, cables, a power meter, a PC (2), and a VNA (3).

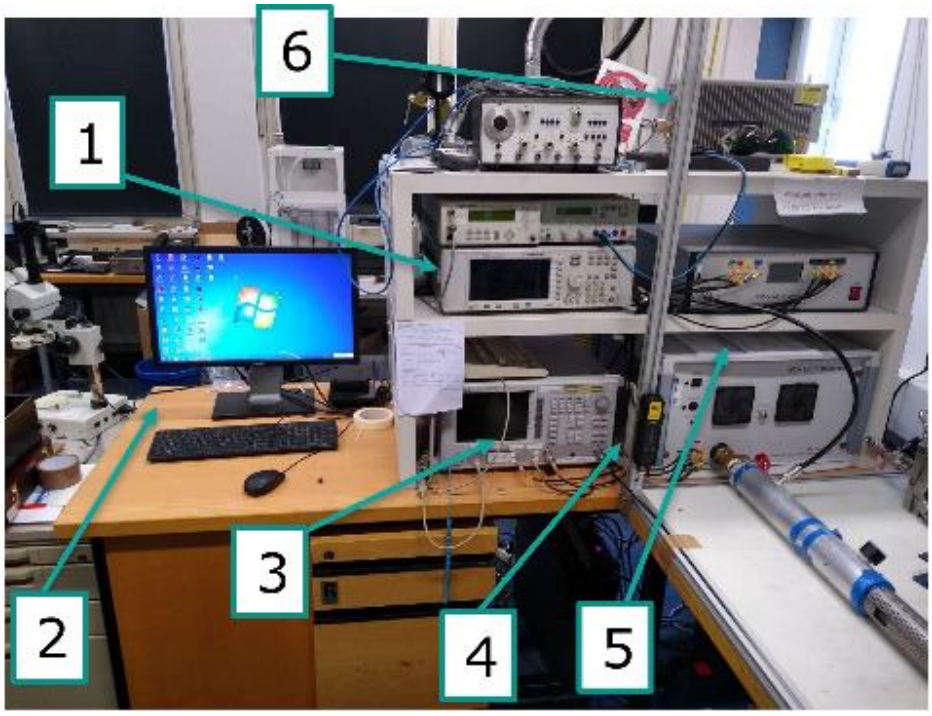

Fig. 1: Special hot-S11 measurement place for 433 MHz with the 6 modules:
1: Signal generator, 2: PC, 3: VNA, 4: EMV tester, 5: Hot-S test-set (upper one), 6: Dummy-load

DOI: https://doi.org/10.26799/cp-sict-plasmatech-tribology-2023

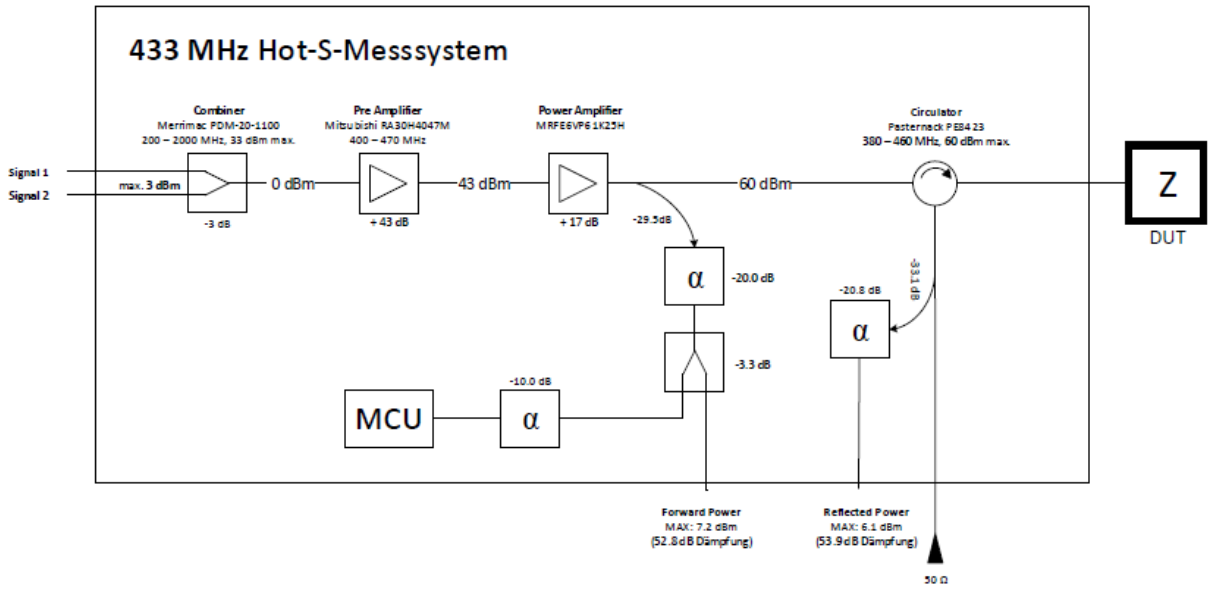

Fig. 2: Units of the hot-S test-set including power level plan of the 433 MHz hot-S11 test-set for the presented plasma jet (DUT for Device Under Test = plasma load)

The VNA's small Signal 1 has a power output of only 0.01 mW (-20 dBm). However, a large signal generated by generator 1's plasma jet semiconductor at f0 = 433 MHz and power level up to 800 W is protected by an isolator from any reflected power and connected to the PA. A small percentage of the small signal is injected into the DUT using a directional coupler. The incident and reflected waves, a1 and b1 are coupled by the first and second directional couplers respectively. In case the DUT is a two-port network, the transmitted power b2 at port 2 is absorbed by a power attenuator or load. Each signal, a1, b1, and b2, is attenuated to a maximum power level of 0 dBm, corresponding to the PA power level of 800 W. The VNA measures the phase and magnitude of forward and reflected waves, corresponding to a1 and b1, and calculates S11 = b1/a1. The results are sent directly to a laptop using a USB cable. The program, which is coded in Python and utilizes the Scikit-rf Open-Source package [11], manages the VNA, processes and rectifies raw data by applying error coefficients derived from the calibration process, and exhibits the S-parameters outcomes.

To avoid generating undesirable harmonics, it is crucial to use the VNA source signal in its linear region. At port 1 of the DUT, there is a significant difference of about 40 dB between the large and small signal which helps minimize the impact of the small signal on the DUT and results in fluctuations of ±1% in the output power level. When it comes to PA parameters, it's important to focus on the level of noise, the bandwidth of the output power, and the smoothness of output power control. The noise level must be at least 20 dB lower than the small signal to prevent any distortion. The vector network analyzer used comprises of a transmitter (TX) and receiver (RX).

DOI: https://doi.org/10.26799/cp-sict-plasmatech-tribology-2023

2. The 433 MHz Plasma Jet

2.1. Overview Plasma Jets

Plasma emitters and jets for the GHz range, particularly around 2.45 GHz, have been extensively developed and are available in the market. The power range varies from 10 W to kW-level jets. Among the different constructions available, a straight copper electrode with a hollow core that allows direct coupling of fiber or powder into the plasma is highly recommended [9].

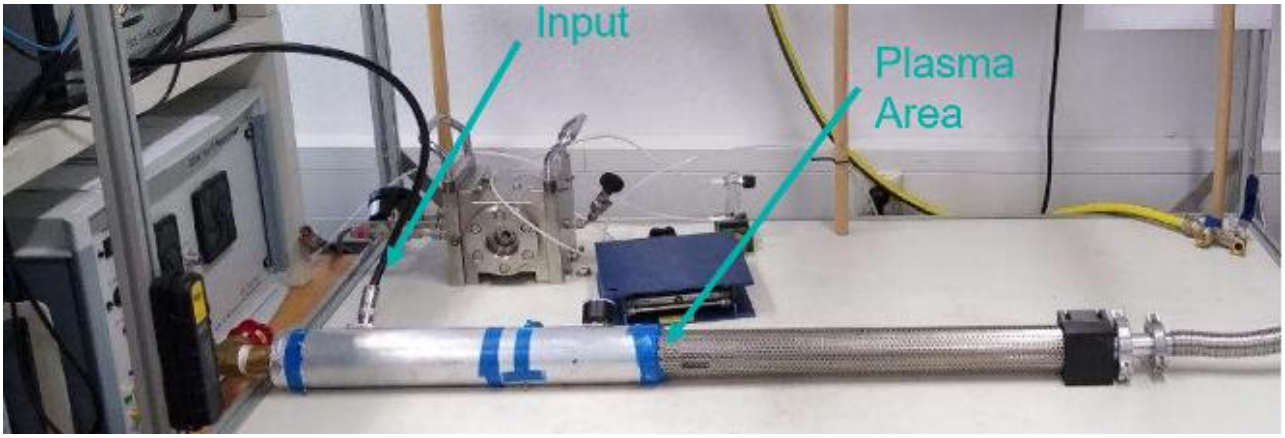

Fig. 3: 433 MHz jet with shielded plasma at the hot-S11 measurement system

The plasma jet in Fig. 3 is displayed in its entirety, encompassing the shield section surrounding the plasma beam. A scientific conference published the creation of a GHz plasma jet with high voltage at one frequency and exceptional matching for high efficiency operation at another frequency in [7]. Further elaboration on the subject is provided in [10]. Additionally, the book will be available in English in 2024.

2.2. Construction of the Plasma Jet

Fig. 4 displays the physical implementations of the internal components. They were each simulated and enhanced using HFSS. These assemblies operate in two ways: Firstly, the series lines and shunt inductors generate high voltage at a specific frequency denoted as f_{ignite}. Secondly, the same assemblies transform the intricate impedance of the plasma foot point to a 50 Ohm level for the microwave assemblies, but at a different frequency known as $f_{operate}$.

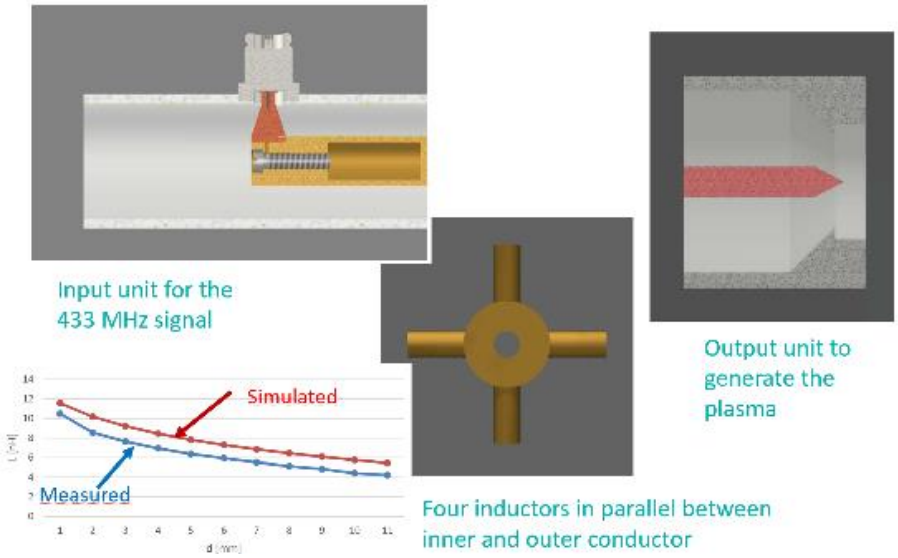

Fig. 4: Drawings of the assemblies: Coaxial input with the transition to the coaxial inner conductor, shunt inductance realized from 4 single inductors and output electrode forming a capacitive load as well as the measured and simulated inductance value.

DOI: https://doi.org/10.26799/cp-sict-plasmatech-tribology-2023

2.3. Simulation Results of the Plasma Jet

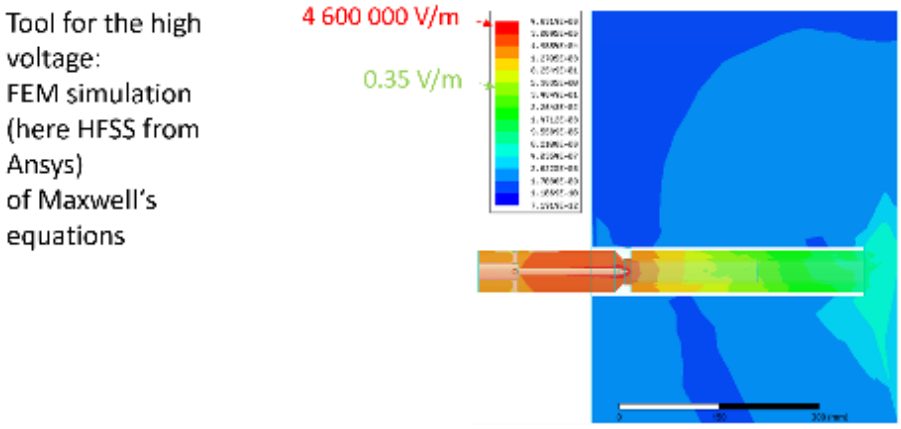

Fig. 5: Simulation results of the electrical field from HFSS for an input power of 200W

In the results displayed in Figure 5, the finite element numerical electromagnetic simulation demonstrates the effective generation of high voltage. The electrode tip is observed to have the highest field strengths, while the contact points experience only low field strengths. It is worth noting that this high-voltage generation does not result in any electric shock issues.

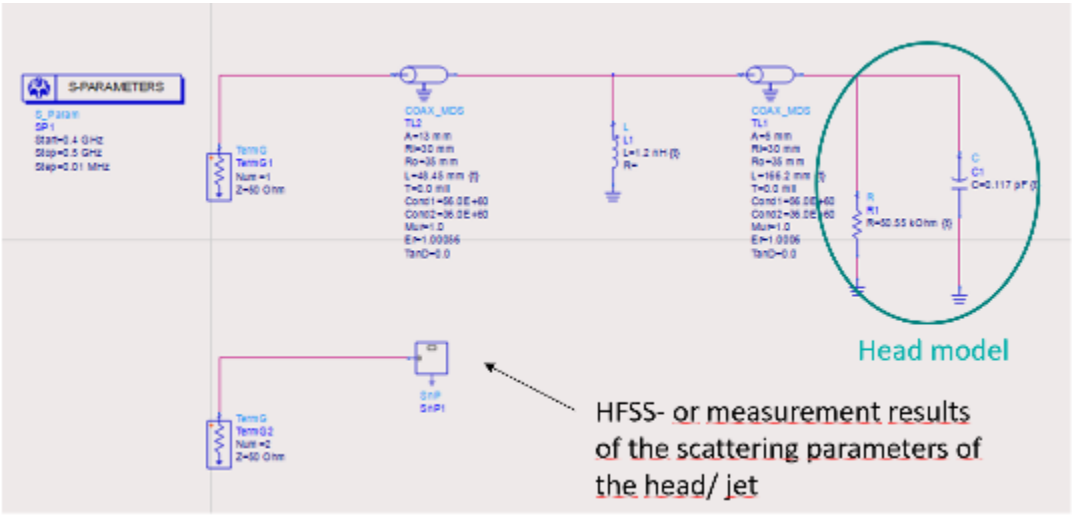

Fig. 6: Simulation model to extract from the HFSS simulation / measurement of the complex impedance of the head

In order to provide a comprehensive comparison, Fig. 6 displays the lumped element/coaxial line circuit model with port 1 and the HFSS, and the measurement result at port 2. The results are further elaborated in the subsequent section. Additionally, Fig. 7 demonstrates the comparison between the lumped elements and the electromagnetic HFSS simulation, which indicates a good overlay.

DOI: https://doi.org/10.26799/cp-sict-plasmatech-tribology-2023

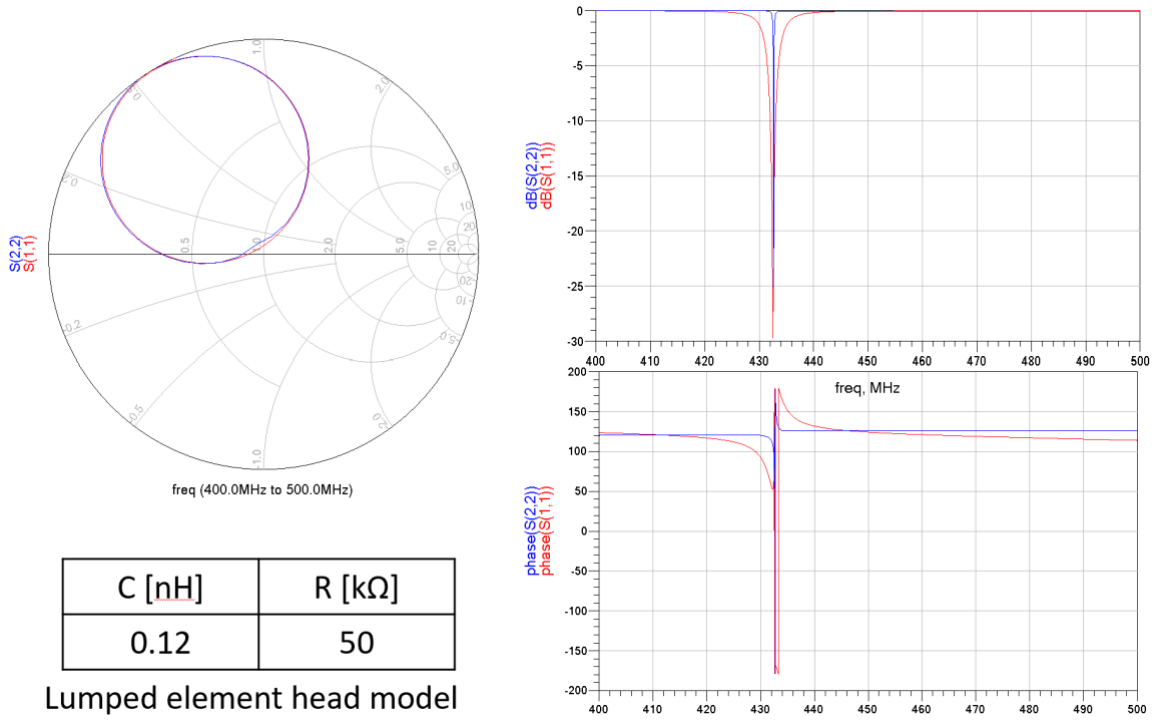

C [nH]	R [kΩ]
0.12	50

Lumped element head model

Fig. 7: Complex results of HFSS and the circuit model over the frequency.

2.4. Measurement Results of the Plasma Jet

All of the measurements were conducted at the Institute for Microwave and Plasma Technology (IMP). The generator of the hot-S measuring station served as the power source.

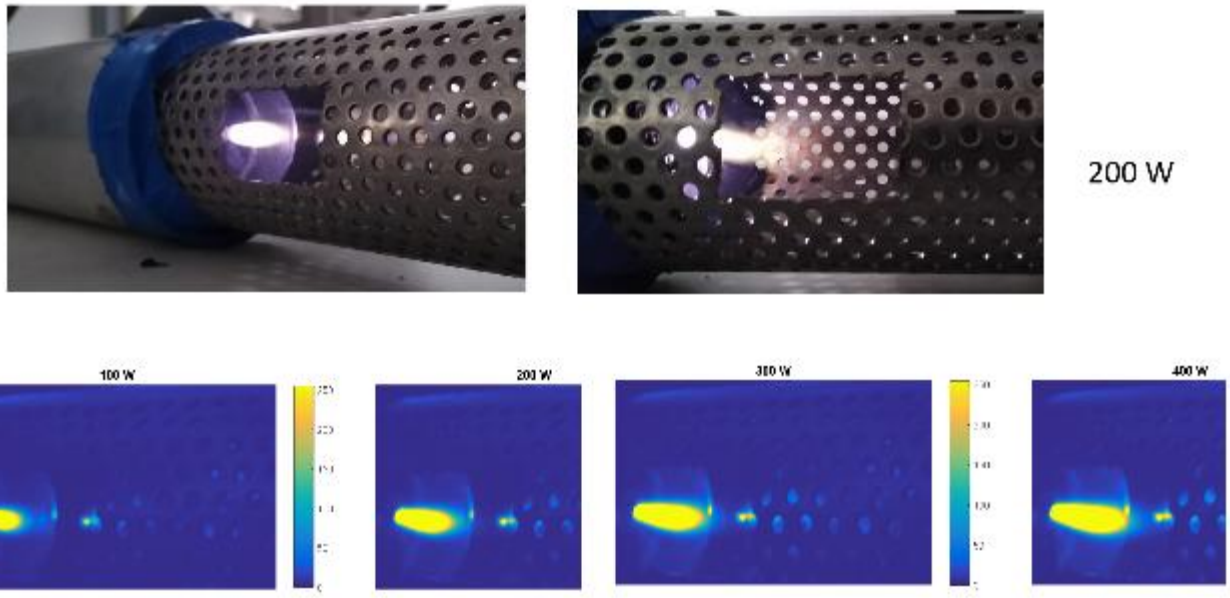

Fig. 8: Pictures with the monochrome camera (sensor IMX 249 without infrared filter) for different power level.

In Figure 8, there are photographs of the shielded plasma jet at different powers operating at 433 MHz, along with infrared photographs at varying power levels.

DOI: https://doi.org/10.26799/cp-sict-plasmatech-tribology-2023

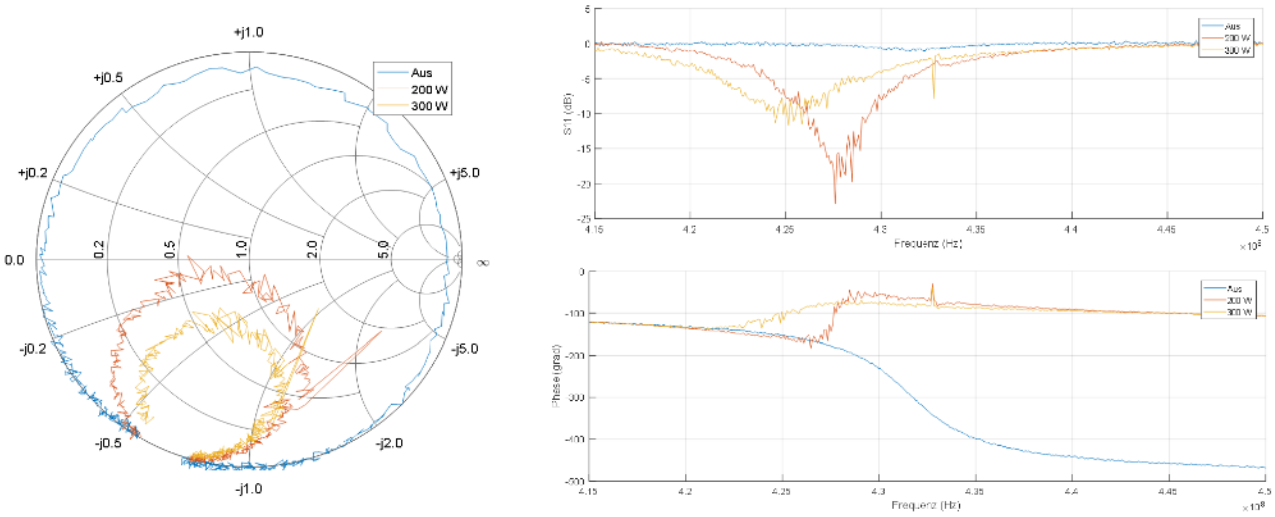

	Off	200 W	300W
R_1 [kΩ]	65	4.0	2.9
C_1 [pF]	0.130	0.188	0.252

Lumped element head model for operation mode

Fig. 9: Complex results of the operation mode after optimization process.

The jet exhibits exceptional performance, with a matching value of over 6 dB at 300 W and an impressive 16 dB at 200 W. Furthermore, the lumped element values of the head's equivalent circuit are illustrated in Figure 9.

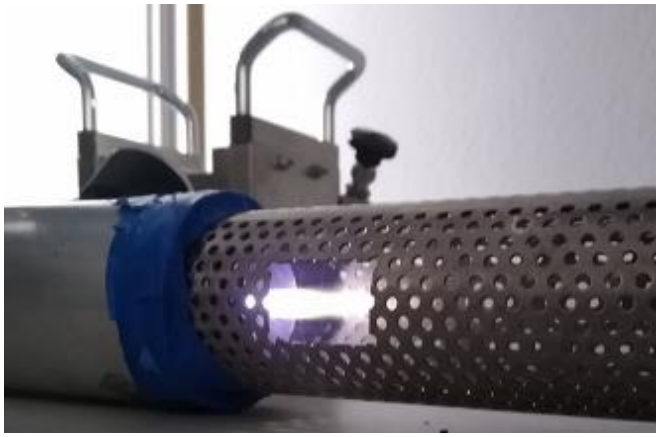

Fig. 10: Largest plasma at a input power of 600W.

According to Figure 10, the plasma jet has a maximum power capacity of 600 W. However, within this power range, its adaptation decreases gradually. If a redesign was feasible, it could result in a plasma of ten times larger capacity, but this was beyond the scope of the project.

DOI: https://doi.org/10.26799/cp-sict-plasmatech-tribology-2023

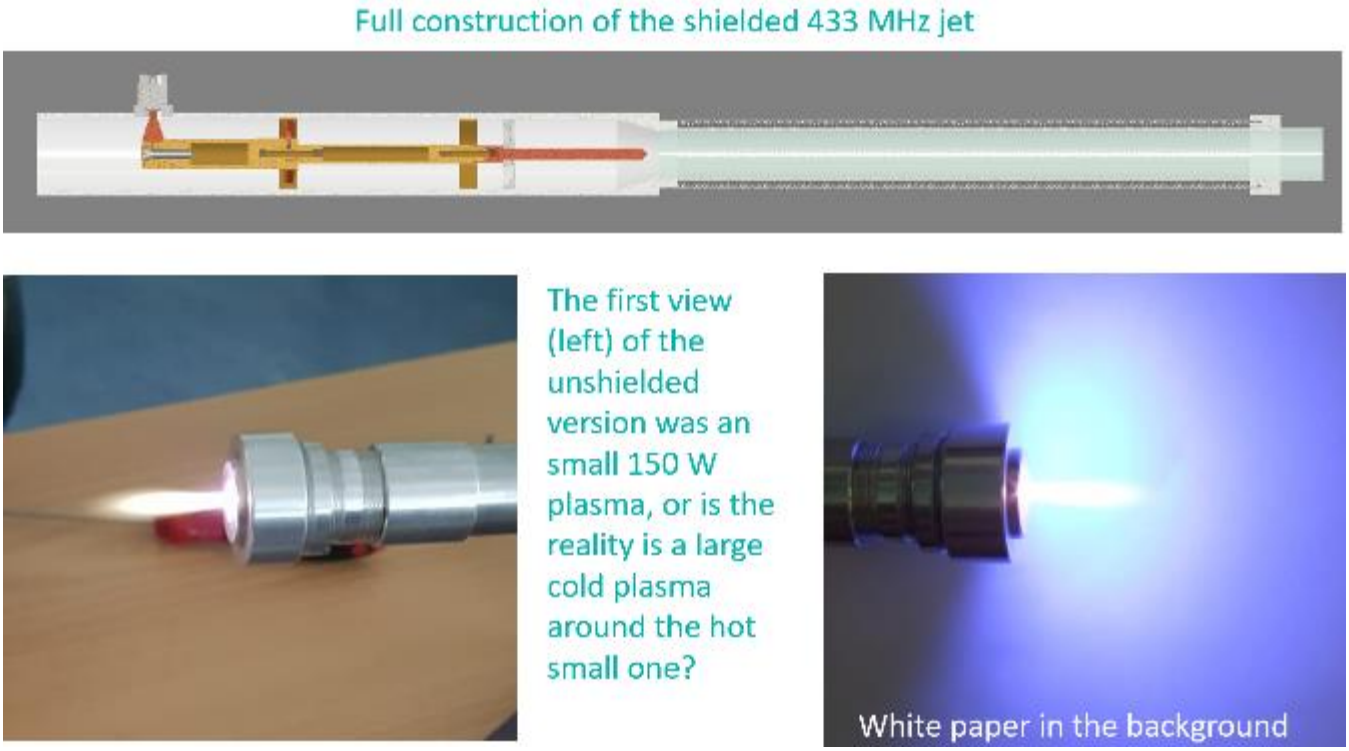

Fig. 11: Unshielded plasma at an input power of only 150W in free-space and with background.

Figure 11 illustrates the full construction and shows the 433 MHz plasma of a well-matched 150W operation.

4. Conclusion

In this paper, we explored the basics of microplasma functioning at 433 MHz and its self-ignition technology. Additionally, we discussed the importance of having a hot-S11 measurement setup for this unique frequency band, and shared details about the internal technology used to measure the 433 MHz plasma. The internal lumped element network of the 433 MHz plasma jet is a crucial component in this process. Through circuit and FEM simulation, as well as measurement results, we have demonstrated that this jet operates smoothly. As a previously unexplored frequency range, this jet is now open for further scientific investigation.

Acknowledgements

The two authors would like to express their sincere gratitude to Samat Turdumamatov for his assistance in the preparation of this publication.

References

1. Datasheets of 2.45 GHz cannula plasma jets, Available: https://hhft.de/jets-pc-serie.
2. Schopp, C., Nachtrodt, F., Heuermann, H., Scherer, U. W., Mostacci, D., Finger, T., Tietsch, W., (2012) A novel 2.45 GHz/200 W Microwave Plasma Jet for High Temperature Applications above 3600 K, *Journal of Physics Conference Series*, (http://iopscience.iop.org/1742-6596/406/1/012029).
3. Wu, L., Zhang, W., Liu, Z., Yu, J., Huang, K., Tao, W., (2020) Experimental Investigation of Microwave Frequency Effects on the Discharge Properties in an Atmospheric-Pressure Coaxial Plasma Jet, *2020 IEEE International Conference on Plasma Science (ICOPS)*.
4. T. Gasseling, D. Barataud, S. Mons, J. . Nebus, J. P. Villotte, J. J. Obregon, and R. Quere, "Hot Small-Signal S-Parameter Measurements of Power Transistors Operating under Large-Signal Conditions in a Load-Pull Environment for the Study of Nonlinear Parametric Interactions," IEEE Transactions on Microwave Theory and Techniques, March 2004.
5. J. Verspecht, D. Barataud, J. Teyssier, and J. Nebus, Hot S-Parameter Techniques: 6 = 4 + 2, in 2005 66th ARFTG Microwave Measurement Conference (ARFTG), Dec 2005, pp. 1–9.
6. H. Porteanu, S. Kuhn, and R. Gesche, Low-Power Microwave Plasma Conductivity, IEEE Transactions on Plasma Science, Jan 2009.
7. H. Heuermann, S. Holtrup, A. Sadeghfam, M. Schmidt, R. Perkuhn, and T. Finger, Various Applications and Background of 10–200W 2.45GHz Microplasmas, in 2012 IEEE/MTT-S International Microwave Symposium Digest, June 2012, pp. 1–3.
8. Elgamal, A., Heuermann, H., Design and Development of a Hot S-Parameter Measurement System for Plasma and Magnetron Applications, German Microwave Conf., Cottbus-Senftenberg, Mar. 2020.
9. H. Heuermann and L. Langer, Atmospheric Plasma Jet Having a Straight Cannula Tube, WO/2019/149897 PCT/EP2019/052518, Aug. 8, 2019.
10. H. Heuermann, Mikrowellentechnik: Feldsimulation, nichtlineare Schaltungstechnik, Komponenten und Subsysteme, Plasmatechnik, Antennen und Ausbreitung. Book, Wiesbaden: Springer Fachmedien Wiesbaden GmbH, 2020.
11. Scikit-rf open source package. [Online]. Available: http://scikit-rf.org

Proceedings of the SICT / Plasma Tech / Tribology 2023 International Joint Conferences
Lisbon, Portugal – April 26 – 28, 2023
DOI: https://doi.org/10.26799/cp-sict-plasmatech-tribology-2023

Polymer Surface Characterization Improved by DCSBD Plasma Technique

Mariana Pajtášová[1], Silvia Ďurišová[1], Darina Ondrušová[1], Petra Skalková[1], Róbert Janík[1], Simona Brigantová[1]
[1]Alexander Dubček University of Trenčín, Faculty of Industrial Technologies in Púchov 491/30, Púchov 020 01, Slovakia, mariana.pajtasova@tnuni.sk

Abstract

The plasma treatment based on diffuse coplanar surface barrier discharge (DCSBD) reflects a modern and low-cost method of surface materials treatment due to its possibility of working in artificial air within regular conditions. In this work, the material referencing the polymer composite system consisting of mixed styrene butadiene rubber/butadiene rubber/natural rubber filled with carbon black and other ingredients was subjected to the DCSBD plasma for two exposure times, briefly, 10 s and 30 s. The presented work was focused on changes in rubber blend morphology studied via SEM and modifications in topography studied by AFM with regards on surface roughness and fragmentation of surface relief. Also wetting characteristics were studied via contact angle measurements by sessile drop method. Furthermore, modified rubbers were characterized by infrared spectroscopy.

Keywords: DCSBD plasma, rubber, surface characteristics, morphology, roughness, topography

1. Introduction

Nowadays, synthetic rubbers such as styrene butadiene rubber SBR and butadiene rubber BR plays an important role in the tire production industry. In many ways synthetic rubbers substitute the processing of natural rubber due to its enhanced performance properties. Thus, in case of SBR, there is the possibility of no premastication during rubber compounding due to its lower viscosity than in case of natural rubber, also styrene butadiene rubber indicates better heat and abrasion resistance comparing to the natural rubber [1]. However, mostly polymers in general are hard to adhere and are non-wettable [2, 3]. To perform changes onto the rubber surface are widely used chemical treatments including abrasion processes, solvent cleaning or acid etching and more important physical treatments including plasma modification [4]. Historically, plasma itself is referred to the fourth state of matter. Herein, the ionization process of gas molecules leads to their excitation and formation of various reactive species, ions, free radicals and unstable particles. Generally, by the equilibrium state of charged particles inside plasma, the plasma can be classified into two categories, respectively, thermal or equilibrium plasma and non-thermal or non-equilibrium plasma [5]. One of these treatment reflects atmospheric plasma source such as diffuse coplanar surface barrier discharge, DCSBD, working in the artificial air. Additionally, the DCSBD represents a novel type of the CBD plasma of surface dielectric barrier discharge (SDBD) plasma source [3].

2. Materials and Methods

The un-vulcanized rubber blend based on polymer matrix consisting of styrene butadiene rubber/butadiene rubber/natural rubber was subjected to the plasma DCSBD discharge. The rubber blend was filled with carbon black. The filler was mechanically conditioned using a Cutting mill SM300 at 1000 rpm, using 6 disc rotor with a 0.25 mm mesh trapezoidal screen. As an activator was used ZnO and stearic acid. Also, plasticizers in the form of oils were added, then, curing agent, accelerator, antioxidants, antidegradants and aliphatic/aromatic resins.

2.1. Plasma reactor KPR 200 mm

An in-line plasma laboratory device generating diffuse coplanar surface barrier discharge KPR 200 mm was used to modify the rubber surface. The operating conditions were set up to power of 375 W with the application of two exposure times, 10 s and 30 s. The rubber blend position was defaulted on 0.5 mm distance above the Al_2O_3 electrode at the active space area of 80 x 200 mm.

DOI: https://doi.org/10.26799/cp-sict-plasmatech-tribology-2023

2.2. Scanning electron microscopy

A scanning electron microscope TESCAN VEGA 3 in the mode of secondary electrons was used to characterize morphology of plasma treated rubbers. Plasma treated rubbers of 0.5 x 0.5 mm were cleaned inside ultrasonic cleaner, then coated with Au-Pa using SC7620 Mini Sputter Coater by Quorum Technologies.

2.3. Atomic force microscopy

The topography and roughness of plasma modified rubber blends was studied by atomic force microscope Belarus NT206.

2.4. Infrared spectroscopy

A Fourier transform infrared spectrometer Nicolet iS50 Thermoscientific was used to study chemical structure of plasma treated rubber blends using ATR technique with the diamond crystal.

2.5. Contact angle measurements

Wetting characteristics were measured by a contact angle measurements using sessile drop method. Herein, two testing liquids were applied, one as a polar liquid (distilled water) and one as a non-polar liquid (diiodomethane). Testing was performed for each rubber specimen ten times to achieve good repeatability.

3. Results

3.1. Scanning electron microscopy of plasma treated samples

The SEM images for 10 s plasma treatment at Fig. 1a) revealed significant morphology forming various globular particles covering the whole rubber treated surface area. As can be seen, these formations are at various dimension with no specific configuration. Additionally, these peculiarities were not observed in the case of untreated rubber. As can be seen at the Fig. 1b) the 30 s treatment revealed way more significant morphology comparing to the 10 s treatment. The ability of forming small globular formations moved to the background and took a more oval shape than globular. Also, as in previous case, formations are in different parameters and with no specific arrangements.

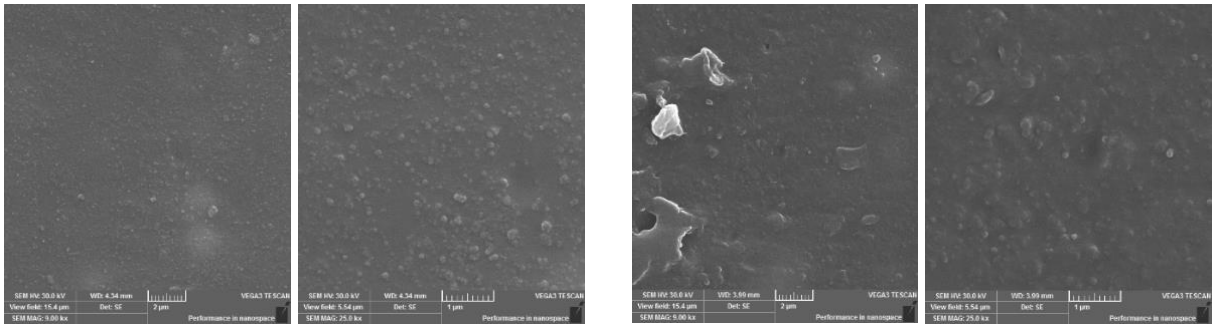

a) b)

Fig. 1: SEM images of a) 10 s and b) 30 s treatment of rubber surface at 9 kx and 25 kx

3.2. Topography and roughness of plasma treated rubbers

The method of atomic force microscopy was used to study the topography and the height of inequalities caused by the plasma treatment. As can be seen from Fig. 2a), a 10 s treatment revealed certain fragmentation of the surface with smoothed wide protrusions reaching a height of 160 nm. However, the protrusions are rather flat in nature without sharp ends. On the other hand, 30 s treatment in Fig. 2b) revealed quite similar relief, by forming adequately flat surface area. However, the protrusions reached the height of 170 nm. In comparison with the untreated rubber, characteristic is the fragmented relief of the sample with a number of wide and irregularly shaped formations rising from the surface to a height of more than 300 nm.

DOI: https://doi.org/10.26799/cp-sict-plasmatech-tribology-2023

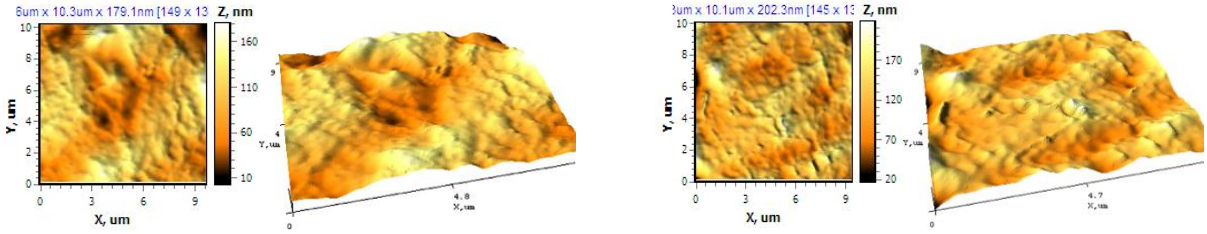

a) b)

Fig. 2: 2D and 3D scans of AFM plasma treated rubbers a) 10 s treatment, b) 30 s treatment

The roughness R_q measurement was performed for five times for each sample. As can be seen in Fig. 3, the plasma treatment smothered the surface and lowered the roughness values almost twice comparing to the untreated rubber, wherein the R_q was 52.59 nm. Although, in the case of 10 s treatment, the roughness was 31.51 nm and for 30 s treatment 28.39 nm.

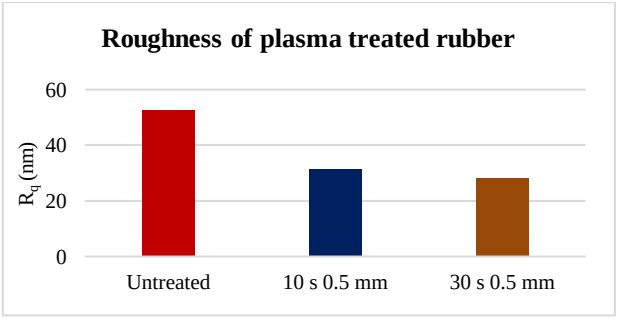

Fig. 3: Illustration of roughness values before and after plasma treatment

3.3. Determination of surface wettability by contact angle measurements

As can be seen in Fig. 4 the contact angle decreased in the direction of higher exposure time of the sample surface to the plasma discharge. In this direction, the surface of the sample showed a higher wettability with both liquids. Namely, the lowest wettability was determined for 30 s treatment in case of diiodomenthane of 34.37% and 40.23% for distilled water. It was followed by 10 s treatment, which reached a slightly higher value of contact angle for diiodomethane of 36.09% and for distilled water of 43.25%.

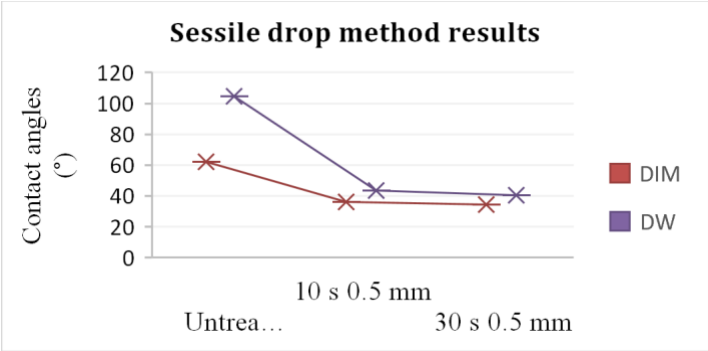

Fig. 4: Contact angle measurements for plasma treated samples

3.4. Characterization of plasma treated rubber by IR spectroscopy

In the infrared spectra at Fig. 5 both plasma treated rubbers revealed the stretching vibrations of ν(C-H) of around 3001 cm^{-1}, and the stretching vibrations of ν(C-H) of around 2950 cm^{-1}, additional stretching vibrations ν(CH_3) can be seen at 2905 cm^{-1} and 2906 cm^{-1}, symmetric stretching ν(C-H) of around 2840 cm^{-1}. The γ(–CH_3) can be seen at the 1428 cm^{-1} and γ(OH) can be seen of around 955 cm^{-1} in each spectrum.

DOI: https://doi.org/10.26799/cp-sict-plasmatech-tribology-2023

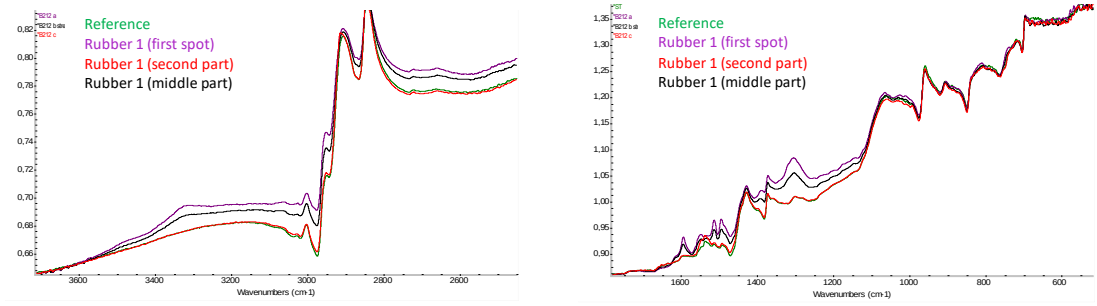

a)

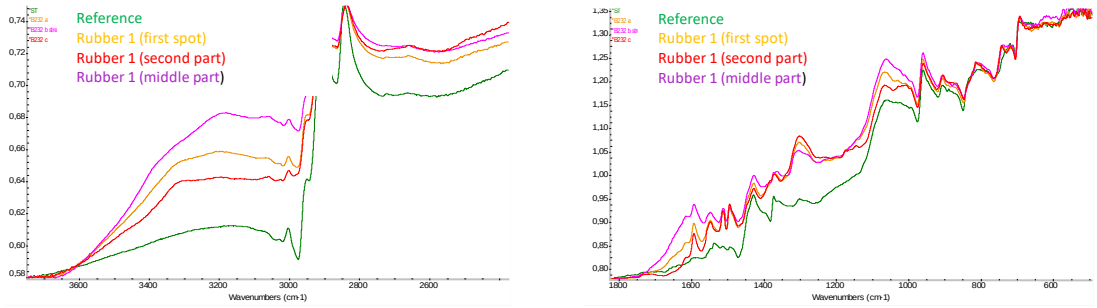

b)

Fig. 5: IR spectra of plasma treated rubbers a) 10 s treatment, b) 30 s treatment

4. Conclusions

The DCSBD plasma source was applied to modify un-vulcanized rubber blend directly onto the surface. Within this study, it was found out, that the plasma exposure time had an effect on the plasma treatment efficiency, however, the most significant impact on the plasma efficiency has the given rubber formulation and the ratio of mixed ingredients. The modified rubber surface was studied by various microscopic techniques and surface characteristics. It was proven, that DCSBD plasma causes significant changes in the morphology, roughness and wettability of examined samples.

Acknowledgements

The work has been supported by the Operational Program Integrated Infra-structure, co-financed by the European Regional Development Fund by the project: Advancement and support of R&D for "Centre for diagnostics and quality testing of materials" in the domains of the RIS3 SK specialization, Acronym: CEDITEK II., ITMS2014+ code 313011W442.

References

1. V.C. Chandrasekaran, *Rubber Seals for Fluid and Hydraulic System*. USA, Elsevier: William Andrew, 2010.
2. M. Berczeli and Z. Weltsh, "Enhanced Wetting and Adhesive Properties by Atmospheric Pressure Plasma Surface Treatment Methods and Investigation Processes on the Influencing Parameters on HIPS Polymer," *Polymers*, vol.13 (6), 901, 2021.
3. M.D. Romero Sánchez, J.M. Martín-Martínez, "Surface modifications of vulcanized SBR rubber by treatment with atmospheric pressure plasma torch," *Int. J. Adhes. Adhes*., vol. 26, pp. 345-354, 2006.
4. K.S. Johansson, "Surface Modification of Plastics," in *Applied Plastics Engineering Handbook*, M. Kutz, Cambridge: William Andrew, 2017, pp. 443-487.
5. U.S. Annapure and T.K. Ranjitha Gracy, "Plasma Modification," in *Physicochemical and Enzymatic Modification of Gums*, H.H. Gahruie, M.H. Eskandari, A. Mousavi Khaneghah and F. Ghiasi, Springer, 2022, pp. 193-211.

Proceedings of the SICT / Plasma Tech / Tribology 2023 International Joint Conferences
Lisbon, Portugal – April 26 – 28, 2023
DOI: https://doi.org/10.26799/cp-sict-plasmatech-tribology-2023

Sensor- Plasma Coupling Resistance: Model and Measurements in the Earth Ionosphere

Elena Seran [1], Sebastien Hess [2], Michel Godefroy [1]

[1] LATMOS/UVSQ/Sorbonne University,
Paris, France, seran@latmos.ipsl.fr
[2] ONERA, Toulouse, France

Abstract

Measurements of the electric potentials and currents in the ionosphere can be perturbed by a plasma sheath formed around the satellite and on-board sensors. Such a sheath is formed around a body to neutralize the electric charging of its surface in contact with the plasma. In the ionosphere, the sheath thickness is expected to be few centimetres and populated with slightly different plasma with respect to the ambient unperturbed plasma. Thus, a characterization of the sheath electrical properties can be essential for the interpretation of the on-board observations. In our paper we analyse a set of the plasma and electric field measurements performed in the ionosphere at the altitude of 700 km on-board the CNES DEMETER micro-satellite. The considered observations were collected during specific orbits when the plasma and electric field instruments were operated in the calibration mode and provided quick plasma measurements together with the wave form electric field records. The electric currents injected from the electric field sensors to plasma during the calibration sequences allow an estimation of the sensor-plasma coupling resistance. The collected data set is used to justify a recently developed analytical model to calculate the sensor-plasma coupling resistance from the measured ion thermal plasma parameters.

Keywords: Earth ionosphere, thermal plasma, sensor-plasma coupling resistance.

1. Introduction

In this paper we analyze a set of the plasma and electric field measurements performed in the ionosphere at the altitude of 700 km onboard the CNES DEMETER micro-satellite. These measurements depend on a number of parameters such as the electric field, the density, temperature and ion composition of thermal plasma, the ratio between the thermal velocities of different plasma species, the plasma kinetic and the satellite velocities, as well as the intensity of the photo-electron emission from the surface materials exposed to the sunlight [3-9]. The onboard measurements can be perturbed by a plasma sheath that envelopes the satellite and onboard sensors. Such a sheath is formed around a body to neutralize the electric charging of its surface in contact with the plasma. In the ionospheric plasma, dominated by the electron current, the body is charged negatively and is enveloped with a thin layer of plasma with the properties slightly different from those of the ambient unperturbed plasma. Thus, a characterization of the electrical properties of the sheath can be essential for the data interpretation. The plasma and electric field observations performed during specific calibration orbits are analyzed and used to justify a recently developed analytical model that provides the relationship between the ion plasma parameters and the sensor-plasma coupling resistance.

2. Instruments

DEMETER (**D**etection of **E**lectro-**M**agnetic **E**missions **T**ransmitted from **E**arthquake **R**egions) is the French CNES (Centre National d'Etudes Spatiales) micro-satellite, placed in 2004 on a quasi-polar heliosynchronous orbit with an inclination of 98°. The satellite performed the plasma and electro-magnetic observations at the altitude of 700 km till 2010 with six scientific instruments on its board. Two instruments of the DEMETER scientific payload, i.e. the ICE (**I**nstrument de mesure du **C**hamp **E**lectrique) and APR (**A**nalyseur à **P**otentiel **R**etardateur), that are sensitive to the satellite electric charging and satellite-plasma interaction are in scope of this paper.

2.1. ICE

DOI: https://doi.org/10.26799/cp-sict-plasmatech-tribology-2023

The ICE is the instrument to measure the electric field in the frequency range from DC (Direct Current) to MHz. The instrument consists of 4 spherical electrically conducting sensors, each of them 6 cm in diameter is accommodated on a 4-m boom [2]. Each sensor measures the electric potential with respect to the satellite potential. With aim to get some understanding about the properties of plasma in the sensor vicinity, two types of currents are injected through the sensor to the ambient plasma, i.e. a DC current which is injected permanently and an alternative current at a calibration frequency which is generated occasionally along the orbit and during calibration sequences. The DC current, which is usually fixed along the orbit at a value ranged between ~0 and 450 nA, partially compensates the current carried by the thermal electrons and thus limit the sensor potential caused by the electron current. Such limitation is important for the measurements in a low density plasma, where the sensor-plasma resistance is high and is not negligible with respect to the sensor electronics resistance. During the calibration sequences, presented in this paper, the value of DC current was swept through a range of possible values. The electric potential, measured at the calibration frequency during each sweeping step, provides an estimation of the sensor-plasma coupling resistance. The knowledge of this parameter is important for two reasons, i.e. (i) the frequency response of the ICE pre-amplifier depends on the value of this resistance, (ii) the value of this resistance is a function of the plasma parameters and can be, in principle, used for the plasma diagnostic.

2.2. APR

The APR retarding analyzer is designed to measure the positively charged ions with relative masses up to ~56. The entrance of different charged species into the analyzer is controlled by a number of polarization grids. One of them is polarized at −12V in order to prevent (i) the photo-electron escape from the analyzer or (ii) the thermal electrons collection. During each measurement sequence, a positive potential applied to another couple of grids is swept between 0 and 20 V. The current collected by the analyzer versus the grid potential is used to deduce the ion composition, density and temperature, as well as the satellite potential [1, 7]. The APR analyzer is accommodated on the satellite ram side and thus measures the one-dimensional ion distribution parallel to the satellite velocity.

3. Sensor-plasma coupling resistance model

In the Earth ionosphere at the altitudes of ~700 km, the potential of an electrically conducting sensor, φ, is mainly determined by a balance between the currents carried by the thermal electrons, thermal ions (principally by O+ and H+) and photoelectrons. This balance reads as

$$f(\eta) = I_e - I_i - I_{ph} - I_{inj} = 0, \quad (1)$$

here $\eta = \frac{e\varphi}{kT}$, I_e, I_i, I_{ph} and I_{inj} are, respectively, the currents carried by thermal electrons, ions and photoelectrons and current injected from sensor to plasma; T is the plasma temperature, e is the electron charge, k is the Boltzmann constant. In case of the negative body potential, the currents carried by the plasma populations can be written in the following forms [4]:

$$I_e = \frac{1}{2\sqrt{\pi}} e n_0 V_{Te} \exp(\eta) S_e, \quad (2)$$

$$I_i = e n_0 V_0 \left\{ 1 + \mu \frac{V_{TO+}^2}{V_0^2} \eta + (1-\mu) \frac{V_{TH+}^2}{V_0^2} (\eta + 0.5) \right\} S_i, \quad (3)$$

$$I_{ph} = j_{ph} S_{ph}. \quad (4)$$

Here n_0 is the plasma density, V_{Te} and V_{Ti} are the thermal velocities of the electrons and ions, V_0 is the body speed with respect to the plasma, μ is the relative concentration of O+ ions, S_e, S_i and S_{ph} are the collection areas for the electrons, ions and photoelectrons, respectively, j_{ph} is the photoelectron current density. The equation (1) can be easily solved by using Newton's method, i.e.

DOI: https://doi.org/10.26799/cp-sict-plasmatech-tribology-2023

$$\eta^{l+1} = \eta^{l} - \frac{f}{f'}\ , \qquad (5)$$

which in few iterrations, *l*, gets sufficiently precise estimation of the η (and thus φ) value.

4. Model and measurements

The plasma parameters together with the sensor-plasma coupling resistance measured during the calibration sequences in July 15-16 of 2004 are presented in the Table 1. One can note that the coupling resistance decreases with an increase of the plasma density and temperature. Its values in the sunlit ionosphere are estimated to be 3-4 times lower than those measured on the night-side orbits.

Table 1: Parameters deduced from the ion analyzer and electric field observations in the dark and sunlit equatorial ionosphere

MLT	Geo Latitude	Density, m^{-3}	Temperature, eV	% O+	Satellite potential, V	Resistance, MΩ
22	-8°…0°	2.8e+09-2.3e+10	0.05-0.1	62-94	-0.03… -0.4	0.1-4
10	+2°…+10°	2.6-4.7e+10	0.17-0.24	78-85	-0.19…-0.5	0.3 - 1

We use the model (1) to calculate the plasma currents and the sensor potential versus the current injected from sensor to plasma and vary the plasma parameters to get the best fit of the measured values of the sensor-plasma coupling resistance. This is done separately for the measurements performed near the equator during three consecutive orbits. The measured and modeled resistances are presented in the Fig. 1. The plasma parameters used for the best fit of the coupling resistances are found to be very close to those measured with the ion analyzer (Table 1).

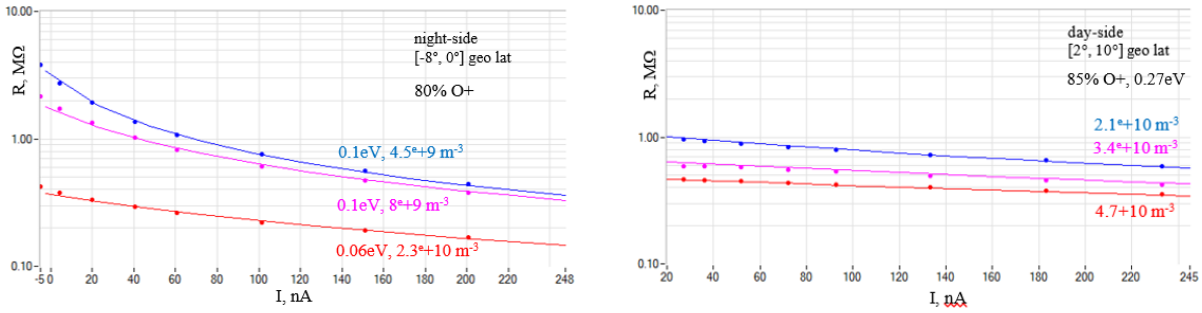

Fig. 1: Sensor-plasma coupling resistance versus injected DC current measured (dots) in the night (left) and day-side (right) ionosphere together with the modelled resistance (lines) calculated for the ion plasma parameters indicated in the figure for each measurement sequence.

5. Conclusion

We have presented the observations performed with the ion plasma and electric field instruments in the Earth ionosphere and used these measurements to validate newly developed model which allows to calculate the electric currents that circulate between sensor and plasma and to estimate the sensor-plasma coupling resistance. Measurements performed in the equatorial regions during three consecutive orbits demonstrate that the coupling resistance is lower in the sunlit part of the ionosphere and is inversely proportional to the plasma density and temperature. The measurements and modeling of this resistance is important not only for the correct understanding of the electric field sensor functioning, but can be used for the estimation of thermal plasma parameters. More comprehensive discussion and results will be presented in future publication.

References

1. Berthelier, J.-J., Godefroy, M., Leblanc, F., Seran, E., et al., (2006a), IAP, the thermal plasma analyzer on Demeter, Planet. Space Sci., 54, 487–501.

DOI: https://doi.org/10.26799/cp-sict-plasmatech-tribology-2023

2. Berthelier, J.J., M. Godefroy, F. Leblanc, M. Malingre, M. Menvielle, D. Lagoutte, J.Y. Brochot, F. Colin, F. Elie, C. Legendre, P. Zamora, D. Benoist, Y. Chapuis, J. Artru, R. Pfaff, (2006b), ICE, the electric field experiment on DEMETER, Planetary and Space Science, 54, 456–471, doi:10.1016/j.pss.2005.10.016
3. Grard, R. J.L., (1973), Properties of the Satellite Photoelectron Sheath Derived from Photoemission Laboratory Measurements, JGR, 78, 2885-2906.
4. Jorba-Ferro, O., (2018), Etude de l'influence de la propreté électrostatique du satellite sur les mesures du champ électrique basse fréquence de TARANIS, PhD Thèses, Université de Toulouse.
5. Hastings, D.E., (1995), A review of plasma interactions with spacecraft low Earth in orbit, Journal of Geophyisical Research, 100, 14447.
6. Mozer, F.S., (1973), Analysis of techniques for measuring DC and AC electric fields in the magnetosphere. Space Sci. Rev. 14, 272.
7. Seran, E., (2003), Reconstruction of the ion plasma parameters from the current measurements: mathematical tool, Annales Geophysicae, 21, 1159–1166.
8. Seran, E., J.-J. Berthelier, F.Z. Saouri, J.-P. Lebreton, (2005) The spherical segmented Langmuir probe in a flowing thermal plasma: numerical model of the current collection, *Annales Geophysicae*, 23, 1723- 1733.
9. Whipple, E.C., (1981), Potentials of surfaces in space. Reports on Progress in Physics, 44 (11), 1197.

Proceedings of the SICT / Plasma Tech / Tribology 2023 International Joint Conferences
Lisbon, Portugal – April 26 – 28, 2023
DOI: https://doi.org/10.26799/cp-sict-plasmatech-tribology-2023

Effect of curing methods on the abrasive and corrosion wear resistance of organic coating systems

Ivan Stojanović[1], Mirta Logar[1], Ivan Fatović[1], Ivan Juraga[1], Vesna Alar[1], Marin Kurtela[1]
[1]Faculty of Mechanical Engineering and Naval Architecture, University of Zagreb
Ivana Lučića 5, Zagreb, Croatia, istojanovic@fsb.hr

Abstract

Nowadays, corrosive destruction of metal machine parts occurs easily, due to increased corrosiveness of the environment as a consequence of increased pollution of water, soil and air. Organic coatings are often used to protect the surface from harsh external factors. Except for the purpose of improving corrosion resistance of metal parts, coatings are used for aesthetic purposes, reduction of mechanical wear, such as due to abrasion and erosion, etc. In order for the coatings not to wear out too quickly, they must be durable. Coating systems based on epoxy and polyurethane are often used, because they create durable, high-quality surfaces that are resistant to wear and tear. With the aim of reducing negative impact on the environment and drying time, IR (infrared) technology can be used for drying the coatings. To simulate the effects of atmospheric corrosion on metal machine parts, testing chambers, such as humidity chamber (simulates an atmosphere of warm air saturated with moisture in the presence of condensed water) and salt spray chamber (simulates a marine atmosphere using dispersed droplets of NaCl solution) are used.

In this paper, solvent-borne 3-layer coating systems from different manufacturers, with and without Zinc in the primer, dried by catalytic IR technology and under atmospheric conditions were studied. Abrasion, hardness, and adhesion tests were performed. Anticorrosion performance of the coatings was characterized using a humidity chamber. The results show that IR-dried coating systems display higher abrasion resistance. The accelerated corrosion test in humidity chamber showed better or equal properties of IR-dried coatings compared to atmospherically dried ones, while reducing drying time considerably.

Keywords: coating systems, abrasion, coating hardness, coating resistance, IR drying

1. Introduction

The biggest cause of steel material destruction is corrosion. Today, the most common way of protecting steel materials is by protective coating, which, in addition to corrosion protection as a primary function, should satisfy some other functions like appearance, resistance to abrasion, hardness and adhesion. Without the satisfactory mentioned secondary properties, the primary protection against corrosion would not be long-lasting, especially in the demanding exploitation conditions in which the steels are found [1,2]. In this work, a comparison of coatings that were dried traditionally atmospherically and with the use of IR drying (Figure 1.) was carried out. In addition to accelerating the drying process of the coating, IR drying also leads to the improvement of physical and chemical properties [3]. Solvent coatings from two manufacturers used in power transformer industry were compared, with and without Zn in primer.

DOI: https://doi.org/10.26799/cp-sict-plasmatech-tribology-2023

Figure 1. IR drying chamber

2. Materials and methods

Solvent coating systems in three layers: epoxy primer with zinc (Zn(R) EP) and without zinc (EP), intermediate epoxy coating (EP) and polyurethane topcoat (PUR), dried in standard atmosphere and with infrared radiation, were tested. Coating systems from German and Danish manufacturers were used and applied to steel test plates (Figure 2.). For the abrasion test, dry sand was used with a rubber wheel at intervals of 3 and 5 seconds with a force of 45 N (Figure 3.). The mass of the test samples before and after the abrasion test was measured and the difference in mass was related to the loss of volume. A humidity chamber was used to demonstrate the effect of moisture on the coating. After 620 h humidity chamber testing, the hardness was tested with the pencil test (Figure 4.) and the adhesion properties were tested with the Pull-off test (Figure 5.).

Figure 2. Samples preparation

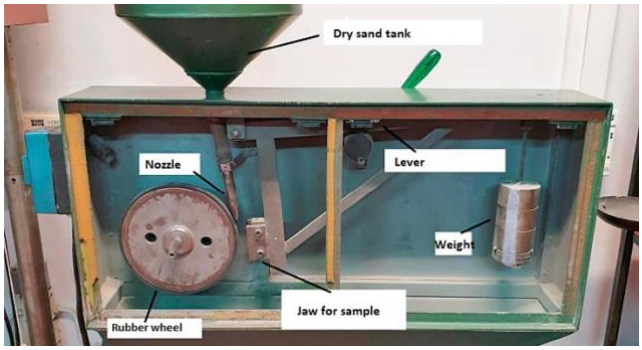

Figure 3. Abrasion test resistance device

DOI: https://doi.org/10.26799/cp-sict-plasmatech-tribology-2023

Figure 4. Pencil test

Figure 5. Adhesion test

3. Results and discussion

Abrasion testing (Figure 6. and 7.) showed slightly better resistance to abrasion of coatings that were IR dried (smaller loss of coating volume) and significantly better resistance to abrasion of coatings that had a Zn rich primer coating.

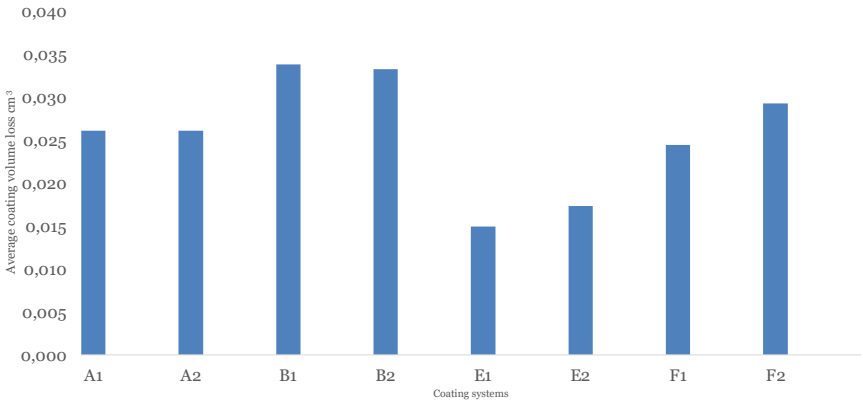

Figure 6. Average loss of coating volume during abrasion resistance test

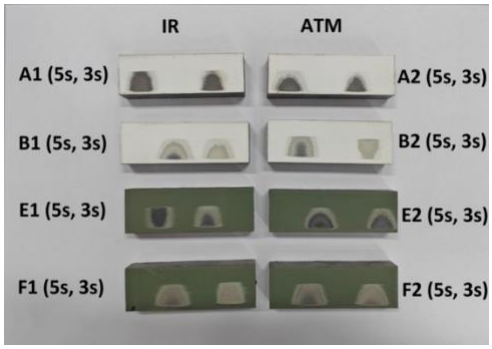

Figure 7. Abrasion test results

The coating systems were kept for 620 h in a humidity chamber, after which the hardness with the pencil test and the adhesion with the Pull-off test were tested. The results show equal hardness in all cases, while adhesion is slightly better in IR-dried systems (Table 1.).

DOI: https://doi.org/10.26799/cp-sict-plasmatech-tribology-2023

Table 1. Hardness and adhesion tests after 620 h in humidity chamber

Coating system		SB: Zn(R) EP-EP-PUR		SB: EP-EP-PUR		SB: Zn(R) EP-EP-PUR		SB: EP-EP-PUR	
		IR	Atm	IR	Atm	IR	Atm	IR	Atm
		A1	**A2**	**B1**	**B2**	**E1**	**E2**	**F1**	**F2**
Pencil test	before humidity chamber	H	B	HB	HB	HB	HB	HB	HB
	after humidity chamber	HB	HB	HB	HB	HB	HB	HB	HB
Pull-off (Mpa)	before humidity chamber	16.43	12.83	17.51	15.29	19.83	15.69	14.95	14.25
	after humidity chamber	16.03	15.13	14.99	14.31	21.98	17.99	19.21	18.78

4. Conclusion

It can be concluded that the systems that have Zn in the primer have much better resistance to abrasion while IR drying does not give any significant improvements in this regard. It can be assumed that Zn in the primer gives better tribological properties. Regarding hardness, no improvement or deterioration of properties was observed between IR-cured and atmospheric-cured coatings. Adhesion properties are somewhat better with IR-dried coatings, although atmospherically dried ones are also satisfactory. The conclusion is that during IR drying, there is no deterioration in abrasion or adhesion properties, i.e., they are the same or better, while the drying time of the coating is significantly shortened.

Acknowledgements

This study is part of the project “Smart plant for drying liquid coatings” which is co-financed within the Operational Programme Competitiveness and Cohesion from the European Regional Development Fund under reference number KK.01.2.1.02.0030. The content of the published materials is the sole responsibility of the Faculty of Mechanical Engineering and Naval Architecture.

References

1. Levy A.V. (1988). The Erosion-Corrosion Behavior of Protective Coatings. Surface and Coatings Technology 36 (1988), pp. 387 – 406.
2. Zhang S.W., Renyang He, Deguo W., Qiyun F. (2001). Abrasive erosion of polyurethane. Journal of Materials Science 36, pp. 5037 – 5043, Kluwer Academic Publishers.
3. Stojanović I., Cindrić I., Janković L., Šimunović V., Franjić H. (2022). Performance Assessment of Differently Dried Coating Systems for Potential Application in the Power Transformer Industry // Coatings, 12 (2022), 3; 1-17 doi:10.3390/coatings12030331

Proceedings of the SICT / Plasma Tech / Tribology 2023 International Joint Conferences
Lisbon, Portugal – April 26 – 28, 2023
DOI: https://doi.org/10.26799/cp-sict-plasmatech-tribology-2023

Capabilities of multiphysics simulations for thrust bearings

Samuel Cupillard[1]
[1]Institut de recherche d'Hydro-Québec
(IREQ, Hydro-Québec's research institute)
1800 boul. Lionel-Boulet, Varennes, QC, Canada, cupillard.samuel@ireq.ca

Abstract

Despite their old design, spring-supported thrust bearings are still used in the hydropower industry to support the weight of rotating parts. Predicting the performance of these components is complex, however, as multiphysics comes into play in a multiscale environment and all elements must be considered to obtain accurate predictions. The different physical phenomena involved were thus coupled in high-fidelity thermo-elasto-hydrodynamic (TEHD) simulations of the thrust bearings under normal operating conditions. First a high-fidelity model was developed and validated, and then a ROM (reduced order model) was built based on the high-fidelity simulations. The ROM was coupled with the continuous monitoring system of the hydropower units to obtain live predictions of thrust-bearing performance that can help identify abnormal behaviours and notify the operator. This paper describes the two models and compares ROM predictions with live temperature monitoring at the resistance temperature detector (RTD) probe inside the pad. Agreement was generally good.

Keywords: thrust bearing, TEHD simulations, fluid-structure interaction, reduced order model (ROM), live prediction.

1. Introduction

A good portion of Hydro-Québec's hydraulic turbines are equipped with spring-supported thrust bearings. Though these bearings operate adequately most of the time, unexpected behaviours and failures do occur from time to time and tracing the cause of failure is not an easy task. Thermocouples placed in the bearing pads are usually the only available monitoring points for assessing the health of a bearing, limiting diagnosis to reactive situations where damage may have already occurred. Numerical analyses that can predict the thrust-bearing performance and possibly catch early symptoms of abnormal behaviours is thus an excellent option.

Complex physical phenomena take place in thrust bearings and they need to be considered to get accurate predictions. Thermal effects and deformations could simultaneously be taken into account starting at the turn of the century thanks to the development of computing capacities, and TEHD (thermo-elasto-hydrodynamic) models have been used extensively since that time as they give accurate results [1]. In fact, in large thrust bearings, pad deformation is of the same order of magnitude as oil film thickness [2]. Soon more and more emphasis began to be placed on fluid and structure coupling to solve TEHD problems [3], [4]. Most thrust-bearing studies deal with pivoted pads, however, with few focusing on spring-supported pads [5], [6].

This paper describes the development of a high-fidelity TEHD model to predict the performance of spring-supported thrust bearings of different designs. High-fidelity models yield highly accurate predictions but require superior computer resources and qualified experts to build them. A ROM (reduced order model) was created to obtain predictions of the bearings in real time. The paper closes with a comparison and discussion of ROM predictions and live temperature monitoring at the resistance temperature detector (RTD) probe in the bearing pad.

2. TEHD high-fidelity model

A TEHD model was developed with ANSYS 19.0. Since the fluid and solid mechanics physics involved in a thrust bearing have a strong interaction, a two-way coupling was set up as extensively described in [7]. One sector was modelled with the use of periodic boundary conditions on circumferential end faces.

2.1. Fluid model

The Navier-Stokes, continuity and energy equations were solved using the finite volume method for an ISO VG 46 laminar oil with temperature-dependent viscosity. The fluid domain encompassed the oil tank in which the bearing is submerged. An opening boundary condition was specified at the outer radius of the oil tank,

DOI: https://doi.org/10.26799/cp-sict-plasmatech-tribology-2023

where the temperature of the incoming cooled oil is set. A force balance between the applied load and the pressure force developed in the oil film drives the axial displacement of the runner. Cavitation is accounted for in the fluid film force by setting negative pressures to zero. Film thickness is a result of runner movement and pad deformation. Accordingly, a mesh deformation technique was used to manage the movement of wall interfaces and the core of the mesh. Care was taken to ensure mesh quality during this process.

2.2. Solid model

ANSYS Mechanical was used to solve the structural and thermal fields with a finite element analysis. The model includes the pad with a babbitt layer, the springs, the runner and the support plate underneath the springs. For simplicity, the runner is considered a non-deformable block. To capture the uniformization of runner temperature due to rotation, a circumferential thermal conductivity a few orders of magnitude higher than that in the two other directions was selected. Two types of springs, helicoidal and polymeric, support the thrust-bearing pads. Both types have nonlinear stiffness-displacement curves that were measured on a hydraulic press and applied for each spring in the model. Dampers were attached at pad corners to keep numerical stability.

2.3. Solution procedure

At each coupling iteration, the fluid model sends heat fluxes and total forces to the solid model, which returns temperatures and displacements until the residuals reach an acceptable level of convergence and the engineering quantities stabilize.

2.4. Case study and validation

The TEHD model was applied to eight different thrust-bearing designs, for a total of 40 units. Table 1 shows the characteristics of three of the designs.

Table 1: Three of the thrust-bearing designs modelled.

	Design #1	Design #2	Design #3
Pad inner radius [m]	0.552	1.026	1.275
Pad outer radius [m]	1.06	1.426	1.86
Rotational speed [rpm]	75	120	100
Number of pads	12	18	12
Number of springs per pad	71	57	49
Type of springs	Helicoidal	Helicoidal	Polymeric
Simulated load [MN]	4.4–6.2	4.7–8.3	13.6–19.0

Results obtained for thrust-bearing design #1 were validated. Measurements taken from four proximity sensors located on one of the pads indicated good agreement with the numerical model in terms of film thickness and temperatures [7].

3. Reduced order model (ROM) for live predictions

ROMs were developed for thrust bearings equipped with the continuous monitoring system. Several TEHD simulations were carried out as a function of oil tank temperature and axial thrust for the eight designs. The limits of the parametric space were chosen based on minimum and maximum values recorded over the last few years during production time of the hydraulic unit. Since each simulation typically requires three to four days of computing on 272 CPU cores, only 15 to 20 operating points were simulated for each thrust-bearing design. The ROMs were built over the parametric space as a function of the two input variables for each of the following engineering quantities: minimum film thickness, maximum temperature on the babbitt, temperature at the RTD probe inside the pad, maximum pressure, friction losses, percentage of pad surface subjected to cavitation, maximum stress on the babbitt surface, crowning and tilt of the pad. The ROMs were based on response surfaces constructed with a polynomial regression up to the third order. The form of the polynomials is given in Eq. (1), with V_{out} being the engineering quantity, V_1 the temperature of the oil tank and V_2 the axial thrust.

$$V_{out} = c_1 + c_2V_1 + c_3V_2 + c_4V_1^2 + c_5V_1V_2 + c_6V_2^2 + c_7V_1^3 + c_8V_1^2V_2 + c_9V_1V_2^2 + c_{10}V_2^3 \quad (1)$$

DOI: https://doi.org/10.26799/cp-sict-plasmatech-tribology-2023

A k-fold cross-validation technique was used to mitigate possible overfitting and select the necessary coefficients c_1 to c_{10} of the models. RMSE (root mean square error) values proved low enough and R2 values were all above 0.99, indicating good correlation of the model and the simulated points. Once the quality of the prediction was satisfactory, the coefficients of each model were exported and transferred to the continuous monitoring system platform, where the polynomials could be reconstructed. Oil tank temperature was directly accessible via the monitoring system. Axial thrust F_{axial}, on the other hand, which was measured during commissioning, first had to be approximated with the polynomial of Eq. (2), where Ov is the opening of the guide vanes, H the gross head of the power plant, H_{com} the gross head at commissioning and F_0 the weight of rotating parts.

$$F_{axial} = \frac{H}{H_{com}}(a_6 Ov^6 + a_5 Ov^5 + a_4 Ov^4 + a_3 Ov^3 + a_2 Ov^2 + a_1 Ov + a_0 - F_0) + F_0 \quad (2)$$

With all variables available from the continuous monitoring system, instantaneous and retrospective predictions could be obtained. Figure 1 shows a schematic of the ROM for minimum film thickness.

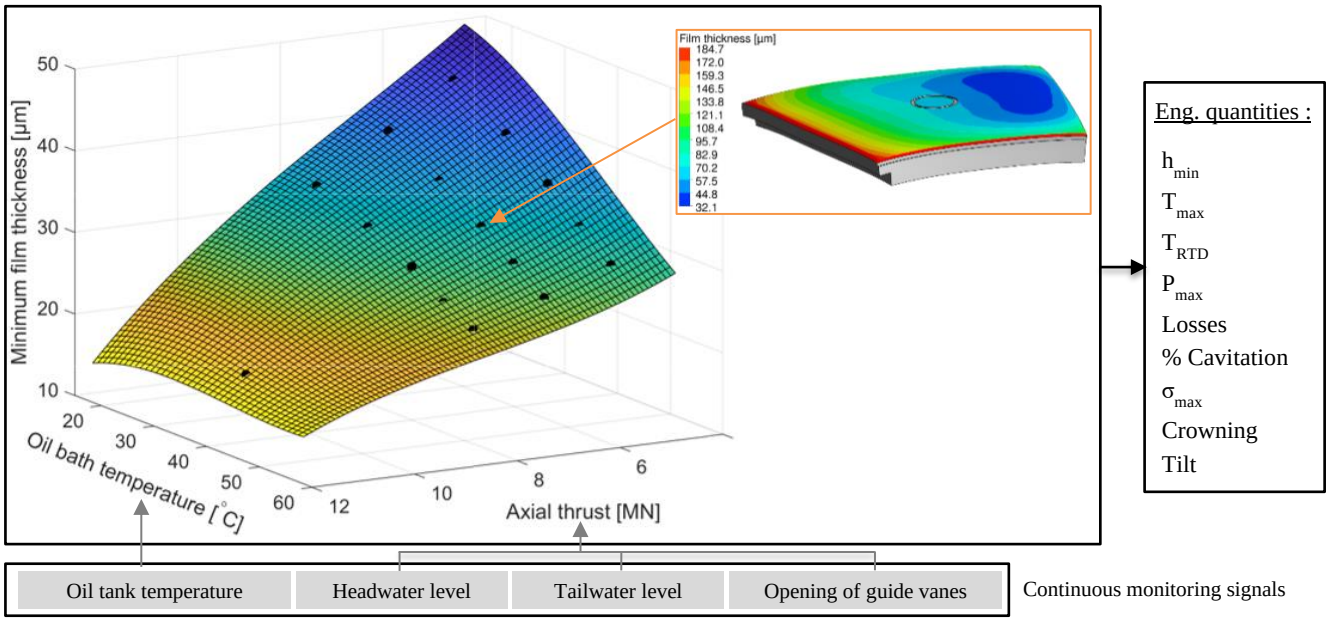

Fig. 1: Schematic of reduced order model (ROM).

To confirm model accuracy, predicted temperatures can be directly compared with measured temperatures at the RTD probe when the unit is operating, the sensors are all functioning and conditions are valid. Figure 2 shows such a comparison for the three thrust-bearing designs investigated in this study. As the figure shows, the models follow trends over time with precision. Temperatures agree very well for some bearings whereas discrepancies were noted for others, perhaps because the models don't consider possible defects in the thrust bearings (misalignment, wear, surface roughness or waviness, faulty assembly, inadequate oil, etc.). In addition, babbitt thermal conductivity was assumed to be the same for all bearings despite possible variation from one bearing to the next and RTD sensitivity to this variable. Finally, sensor signals can sometimes be questionable for all sorts of reasons.

DOI: https://doi.org/10.26799/cp-sict-plasmatech-tribology-2023

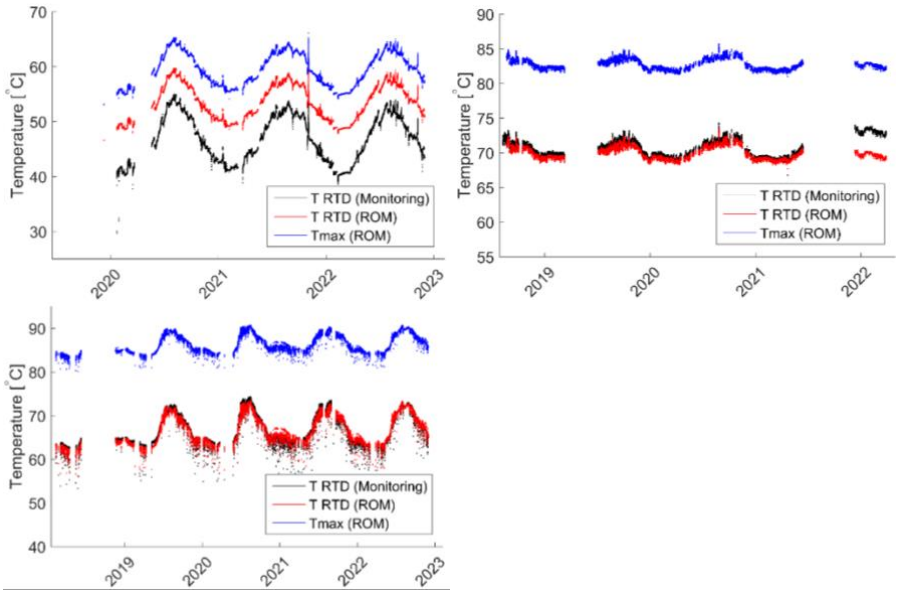

(a) Design #1 (b) Design #2 (c) Design #3

Fig. 2: Measured and predicted temperatures at the RTD probe as well as predicted maximum temperature.

Figure 2 also illustrates differences between measured RTD temperatures and real maximum temperatures, which are about 10ºC to 20ºC higher. The alarms that trigger machine shutdown when bearing temperatures run too high are based on RTD temperatures. It might be a good idea instead to use predicted maximum temperature or minimum film thickness to optimize and customize alarm thresholds, as these two parameters better represent the safety limits of the thrust bearing. In addition, it turns out that data on long-term trends are very valuable. In fact, deviations over time between predictions and measurements serve as warnings of performance degradation due to an ongoing failure mechanism or sensor issues.

4. Conclusion

This paper describes the development of a high-fidelity model with multiphysics coupling. A substantial number of TEHD simulations of eight different thrust-bearing designs were performed to create ROMs of 40 thrust bearings used in hydroelectric units. The ROMs were successfully connected to the continuous monitoring system of the units, allowing real-time and retrospective tracking of thrust-bearing performance. This study offers promising new avenues:

- Having continuous access to engineering quantities that better represent the safety limits of bearings could help in optimizing and customizing bearing alarm thresholds.
- Long-term trends in predictions and measurements can highlight deviations over time and make it possible to catch early symptoms of failure.
- While the high-fidelity models can be used in root cause analysis of problematic cases or for design improvement, the ROMs open the door to diagnosis and prognosis.

References

1. P. Monmousseau, M. Fillon and J. Frêne, “Transient thermoelastohydrodynamic study of tilting-pad journal bearings under dynamic loading,” in *International Gas Turbine & Aeroengine Congress & Exhibition*, 1997.
2. B. Huang, Z.D. Wu, J.L. Wu and L.Q. Wang, “2D THD and 3D TEHD analysis of large spindle supported thrust bearings with pins and double layer system used in the three gorges hydroelectric generators,” *IOP Conference Series: Earth and Environmental Science*, vol. 15, no. 7, 072025, 2012.
3. M. Wodtke, A. Olszewski and M. Wasilczuk, “Application of the fluid–structure interaction technique for the analysis of hydrodynamic lubrication problems,” *Proceedings of the IMechE, Part J: J. of Eng. Trib.*, vol. 227, no. 8, pp. 888-897, 2013.
4. P. Pajączkowski, “Simulation of transient states in large hydrodynamic thrust bearings,” Doctoral thesis, Gdansk Univ. of Tech., 2010.

DOI: https://doi.org/10.26799/cp-sict-plasmatech-tribology-2023

5. F.X. Borras, "Multiphysics modelling of spring-supported thrust bearings for hydropower applications," Master thesis, Luleå Univ. of Tech., 2012.
6. J.H. Yuan, J.B. Medley and J.H. Ferguson, "Spring-supported thrust bearings used in hydroelectric generators - laboratory test facility," Trib. Trans., vol. 42, no. 1, pp. 126-135, 1999.
7. S. Cupillard and P. Gauvin, "Behavior of spring supported thrust bearings: a CFD and experimental investigation," in *18th EDF/Pprime Workshop*, EDF Lab Paris-Saclay, 2019.

Proceedings of the SICT / Plasma Tech / Tribology 2023 International Joint Conferences
Lisbon, Portugal – April 26 – 28, 2023
DOI: https://doi.org/10.26799/cp-sict-plasmatech-tribology-2023

Smart Lubrication Management of Rolling Element bearings using a State-Estimation-Based Control Strategy

B. Mrak[1,*], B. Peremans[1], Y. Perremans[1], D. Fauconnier[2], Z. Tao[1], S. Schlimpert[1]
[1]Flanders Make, Core Lab MotionS, Lommel, Belgium
[2] Flanders Make, Core Lab MIRO, Ghent University, Ghent, Belgium
*branimir.mrak@flandersmake.be

Abstract

Majority of modern mechatronic systems feature a number of rolling element bearings as a cost effective and performant solution to support rotating shafts, and transfer the mechanical load between static and rotating machine components. Often, cooling and lubrication in multi-bearing systems is suboptimal due to the abundant supply of oil flow to constrain the bearing and increase viscosity and prevent early failures. In this work, however, we apply a state-estimation-based predictive control strategy on the simultaneous lubrication and cooling of a multi-bearing system such that the lubrication condition is actively adjusted to the variable operating conditions. Such strategy aims to increase the global operational efficiency of the system, by minimizing losses e.g. by drag. Preliminary simulation results demonstrate a reduction in bearing losses of from 3-33% for a given gearbox subject to a variable speed and load.

Keywords: rolling element bearings, active cooling and lubrication, control strategy, bearing frictional loss reduction

1. Introduction.

Nowadays, rolling element bearings facilitate the operation of a vast majority of mechatronic systems. Typically, the bearings are simultaneously lubricated and (passively) cooled by a single lubricant stream. The lubricant distribution in between different bearings is determined by the application-specific design (e.g. splash lubrication, oil recirculation, etc.), and the cooling and lubricating functions of the oil stream highly depend on the governing operational conditions (e.g. operating speed of the machine) and design constraints (e.g. bearing type, geometry, cooling paths). Despite the various bearing cooling and lubrication methods, most industrial systems rely on sump lubrication or recirculating lubrication. The latter is used to evacuate the frictional heat from the bearings and provide external cooling of the lubricant. Bearing cooling and lubrication conditions are generally tuned for a nominal operating point. As a result, cooling and lubrication conditions are suboptimal in other operating conditions, leading to increased bearing losses.

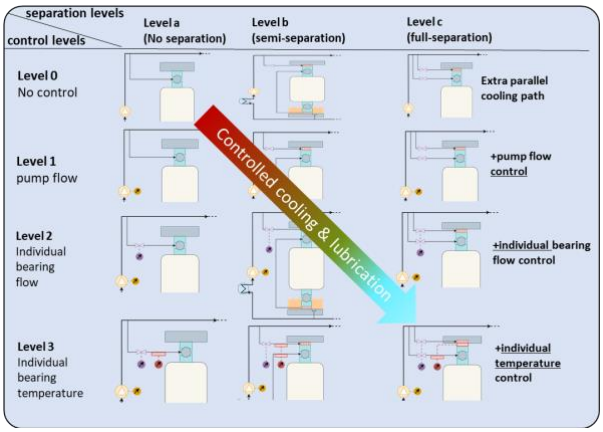

Figure 1: Overview of active cooling and lubrication concepts by splitting up the cooling and lubrication function (horizontal axis) and oil flow rate control and oil inlet temperature conditioning (vertical axis).

The bearing heat losses caused by oil drag and friction can be reduced by 1) controlling the oil flow rate and oil supply temperature towards the bearings [1] and 2) separating the cooling and lubrication function by using additional cooling methods [2]. Multiple active cooling and lubrication strategies can be defined based on the level of control and the level of separation of cooling and lubrication (see Fig. 1).

DOI: https://doi.org/10.26799/cp-sict-plasmatech-tribology-2023

In this work, a preliminary analysis of an actively controlled multi-bearing case is studied. The analysis is performed on a two-stage gearbox for variable operating conditions with oil flow rate control applied to two sets of bearings (low and high speed) while maintaining optimal lubrication conditions to ensure an optimal lifetime of the bearings.

2. Methodology

2.1. System level model of a gearbox use case

A gearbox use case is selected as a typical mechatronic subsystem with a complex cooling/lubrication circuit (see Fig. 2.a). This gearbox is designed with a two-stage configuration including two high speed shafts (left and right) and a single low speed shaft (middle), resulting in an internal reduction ratio of 1-to-5. The shafts are supported by deep groove ball, cylindrical, and tapered bearings with inner diameters of 50 mm, 120 mm, and 60 mm, respectively, on the left, middle, and right shafts.

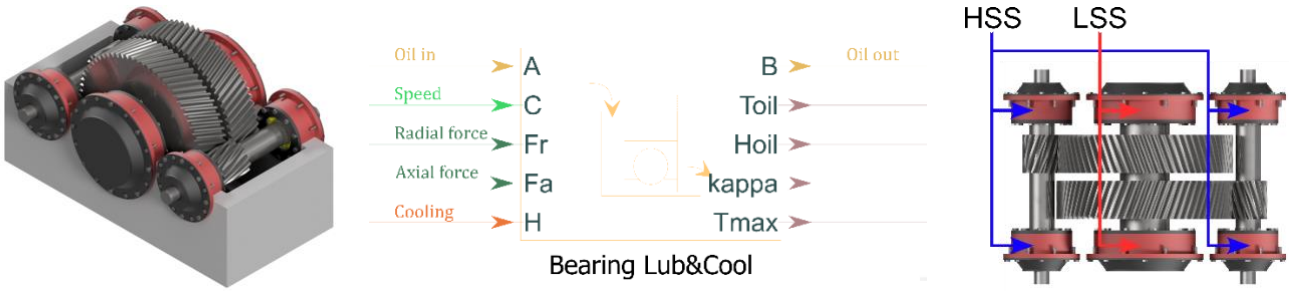

a) b) c)

Figure 2. Gearbox setup a) CAD rendering of the selected gearbox design, b) custom Simscape bearing block, c) hydraulic connection schematic (HSS = high speed shaft, LSS = low speed shaft).

Without loss of generality, every lubricated multi-bearing system design will have to consider and trade-off the interdependencies between the bearing type (and size), operating conditions (including temperatures), and lubrication conditions (including the selection of lubricants). The bearing size is determined based on load, speed, and lubrication conditions. Operating temperature can be considered as a dynamic equilibrium driven by load, size, rotational speed, lubrication conditions, and the heat transfer to the surroundings. Lubrication conditions depend on the orientation of the bearing, the supply efficiency of oil, oil and bearing temperatures, lubricant properties, and the rotational speed.

The temperature of the oil in the bearing greatly affects the application performance as it determines the oil viscosity which directly relates to 1) the lubricant film quality which is estimated using the viscosity ratio κ [3], and 2) the bearing drag losses [4]. Moreover, bearing drag and friction losses are influenced by the amount of oil being supplied to the bearings [4]. The oil temperature follows from the heat balance of the use case including heat generated by frictional losses, heat conduction and heat convection towards the forced oil flow and ambient. Furthermore, the thermal capacitance of the system determines the transient behaviour of the oil temperature in case of changing conditions, e.g. a changing load or speed.

For a proper performance analysis of a multi-bearing use case, a coupled transient thermal-hydraulic-mechanical system model which allows to determine the oil temperature in the individual bearings as well as the amount of oil flow rate towards the bearings is essential. allowing modularity for different systems of varying complexity. The system model is implemented in the Simscape environment using a custom Simscape block for the cooling and lubrication function of the bearing which is integrated in our in-house HYPERTHERM library [5]. The custom bearing block (Fig. 2.b) includes bearing lubrication and cooling with lubrication conditions determined by ISO281 correlations [3] and a bearing frictional model based on SKF correlations [4], and couples to bearing load conditions (radial force, axial force and rotational speed) and a cooling circuit. Furthermore, the bearing thermal behaviour is simplified using a bearing lumped thermal network model.

2.2. State estimation framework

DOI: https://doi.org/10.26799/cp-sict-plasmatech-tribology-2023

The steady-state lubrication condition for a bearing is represented typically by the viscosity ratio (κ). A higher value of κ corresponds to a better lubrication condition, i.e. increased lubricant film thickness in the contacts, resulting in an increased rated life of the bearing [3]. Secondary, the oil level within the bearing housing, indirectly influences the film formation in the contact, because it largely determines the distribution of lubricant in the rotating bearing and hence on the roller surfaces. Optimal EHL lubrication corresponds to a viscosity ratio κ = 4 and a minimum oil height equal to the half-height of a roller element $H_{oil} = \frac{1}{2} D_{roll}$.

Typically, κ cannot be measured directly and is derived based on the bearing speed and temperature [3], whereas the oil height is estimated based on the supplied oil flow rate.

2.3. MIMO control problem

Controlling the lubrication and cooling system of the gearbox is a multiple input multiple output (MIMO) control problem. Depending on the layout of the active cooling and lubrication system (as shown in Fig. 1), the dependencies and the controllability of this system will vary. Another aspect to consider when making this approach generic to other use cases is the number of active inputs to deal with multiple constraints in a single control input. As for the multi-bearing case, each bearing is constraint by a minimum κ-value and minimum oil height. By controlling the oil flow rate of the bearing, the bearing condition is pushed to either one or the other constraint, depending on thermal and loading conditions. Therefore, we propose the use of the consensus algorithm [6,7] as an approach to find an agreement between multiple constraints.

In our gearbox use-case, the bearings are grouped in two sets, i.e. the high speed bearings (left and right shaft) and low speed bearings (middle shaft), of which for each set the oil flow rate is controlled (see Fig. 2.c). This approach is advisable when the system is not fully controllable. As such, the control strategy determines which of the constraints is more critical (κ and H_{oil}) and adapt the flow command accordingly.

3. Simulation results

In this particular case study, simulations are performed on an active cooling and lubrication architecture with active flow rate control towards two groups of bearings (see Fig. 2c .). To simplify the analysis, a stepwise speed profile is applied with a total duration of 2000 seconds which jumps abruptly from 2000 rpm to 4000 rpm at t = 1000 s. The output torque is fixed at 1000 Nm. The oil supply temperature is set to $50°C$.

As shown in Figure 3, the results obtained from applying active control demonstrate notable reductions in bearing frictional torque. The results for the high speed bearings in Fig 3.a show that in this case the κ-values are always significantly higher than the set limit of κ = 4. The oil height H_{oil} is therefore the dominant value to control and is reduced by the control towards the minimum value $\frac{1}{2} D_{roll}$ by reducing the input flow. For the low speed bearings (see Fig. 3.b), κ is the dominant constraint during the lower speed operation ($t = 0 - 1000\ s$) as the low speed requires a high oil viscosity for sufficient lubrication. As a result, a relatively high oil volume is present. After $t = 1000\ s$, the increase in speed results in a higher κ which allows the flow rate to be reduced. Moreover, the active constraint shifts towards H_{oil}. It should be noted that due to controlling the oil flow rates in bearing groups, not all bearings are able to reach the minimum oil height. Individual bearing flow rate control would circumvent this and allow the friction losses to be reduced further. Overall, the actively controlled bearing lubrication leads to a friction torque reduction of 3.2%-4.5% on the high-speed shaft bearings and 20%-33% on the low-speed shaft bearings, respectively. This reduction can be attributed to the reduced oil flow rate which prevents bearings from overflooding and allows increased oil viscosity, i.e. higher oil temperature, for reduced drag losses.

4. Conclusions

In this study, an active control approach for systems of rolling element bearings with cooling and lubrication was presented. Simulation results demonstrated that the active control strategy yielded robust and improved performance across all load conditions. The results showed that the viscosity ratio (κ) is maintained above the minimum requirement of 4 for all speeds, indicating a significantly reduced risk of mixed lubrication and wear. The reduction in oil height H_{oil} resulted in decreased churning losses at lower speeds while still satisfying the minimum requirements. Based on 0-D phenomenological models of the frictional torque in steady-state

DOI: https://doi.org/10.26799/cp-sict-plasmatech-tribology-2023

conditions, a reduction in losses of 3.2%-4.5% was achieved for high-speed bearings and a remarkable reduction of up to 33% was achieved for low-speed bearings, in comparison to the SKF guideline benchmark.

Future work should focus on testing and validating the proposed approach using single bearing and multiple bearing setups. It is also essential to validate the model and state estimation for accurate prediction and control. Additionally, the applicability and accuracy of film thickness models in the context of rolling element bearings in oscillating machinery remain an open question and warrant further investigation. The models presented in [2,8] could serve as a starting point for addressing this issue.

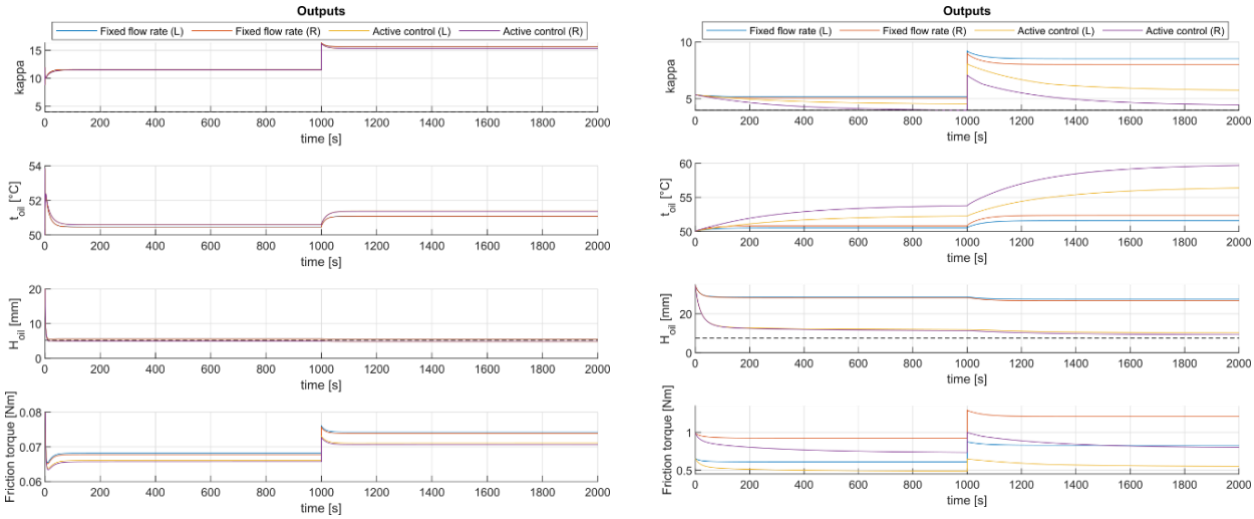

a) b)

Figure 3. Simulation results for the gearbox use case with and without active control for a) the high speed shaft bearings and b) the low speed shaft bearings.

Acknowledgements

This research is part of the ActiLub SBO project funded and supported by Flanders Make, the strategic research centre for the manufacturing industry

References

1. Janssens O., Rennuy M., Devos S., Loccufier MVan de Walle ., R. and Van Hoecke S., "Towards intelligent lubrication control: Infrared thermal imaging for oil level prediction in bearings," 2016 IEEE Conference on Control Applications (CCA), 2016, pp. 1330-1335, doi: 10.1109/CCA.2016.7587991.
2. Flouros, M.; Gloeckner, P.; Hirschmann, M.; Martin, M.; Cottier, F.; Papailia, D. Experimental and Numerical Investigation of the Outer Ring Cooling Concept in a Hybrid and in an All-Steel Ball Bearing Used in Aero-Engines by the Introduction of a Helical Duct. Aerospace 2018, 5, 23.
3. Rolling bearings – Dynamic load ratings and rating life. ISO 281:2007(E), 2007.
4. Rolling bearings – SKF Catalogue. PUB BU/P1 17000/1 EN, October 2018.
5. Advanced Cooling for Powertrains – blogpost. URL: https://www.flandersmake.be/en/blog/advanced-cooling-powertrains, Publication date: 30/11/2022, Access date: 30/05/2023.
6. Li, L., Fu, M., Zhang, H., & Lu, R. (2018). Consensus control for a network of high order continuous-time agents with communication delays.*Automatica*,*89*, 144-150.
7. Muñoz, F., Espinoza Quesada, E. S., La, H. M., Salazar, S., Commuri, S., & Garcia Carrillo, L. R. (2017). Adaptive consensus algorithms for real-time operation of multi-agent systems affected by switching network events. *International Journal of Robust and Nonlinear Control*,*27*(9), 1566-1588.
8. Hooke, C. J. The Minimum Film Thickness in Line Contacts During Reversal of Entrainment. *Journal of tribology*, 1993, Vol.115 (1).

Proceedings of the SICT / Plasma Tech / Tribology 2023 International Joint Conferences
Lisbon, Portugal – April 26 – 28, 2023
DOI: https://doi.org/10.26799/cp-sict-plasmatech-tribology-2023

Influence of different deterministic surface texturing processes on friction and tool life for load collectives in sheet metal forming

Philipp Schumann[1], Rik Lindner[1], Peter Groche[1]
[1]Institute for Production Engineering and Forming Technology
Otto-Berndt-Strasse 2, Darmstadt, Germany, philipp.schumann@tu-darmstadt.de

Abstract

Sheet metal processes such as blanking or deep drawing are usually characterized by high production volumes and dynamically stressed tools. These complex, time-variant tribological challenges can be partially mastered by tailored tool surfaces in the submillimeter range. A reduction in lubricant consumption, coefficient of friction, and an increase in service life are possible results. However, the production of textured surfaces is very challenging. Production time, the definition of texture geometry, reproducibility, and tool life for texturing processes are inhibiting factors for the introduction into industrial applications.

Therefore, this study investigates the benefits of deterministic surface texturing of a typical cold-forging steel by two different texturing processes in comparison with the industrial standard of manual polishing. The resulting deterministic topography of a laser-textured surface is compared with a machine hammer-peened surface structure using a micro-tip tool. Differences in the production time, as well as the resulting surface quality, are investigated. Using a continuous strip drawing test, the microtextured tool surfaces under varying levels of surface coverage are investigated. The resulting coefficient of friction and tool lifetime for changing contact normal stresses reaching from 5 to 25 MPa are compared with an industrial polished surface. Eventually, the influence of tribological performance is evaluated. A reduction of the coefficient of friction, as well as an improvement in surface hardness due to the investigated processes, are shown.

Keywords: sheet metal forming, surface texturing, micro dimple, friction, tool life, strip drawing, machine hammer peening

1 Introduction

Ecological and economic challenges in the mobility sector are leading to an increasing demand for higher-strength steels. The use of these steels allows structural components to be made significantly lighter, thus reducing emissions, and making more efficient use of the energy available for combustion driven and electric vehicles [1]. Therefore, in the automotive industry, the use of advanced high-strength steels plays an important role [2, 3]. The use of higher-strength materials also increases the load on the tools, which leads to accelerated wear and reduced service life [4]. The occurring wear may affect the forming results, the process limits, and the lifetime of sheet-metal working processes such as deep-drawing and stamping tools [5, 6]. Especially in areas with high contact normal stresses, such as radii or draw beads, increased wear can occur [7].

To improve the tribological properties of tools for boundary and mixed friction, this study considers the manipulation of frictional behavior by micro texturing using laser texturing and texturing by machine hammer peening using a strip drawing tribometer.

2 Materials and Methods

2.1 Tribological System

The wear behaviour of the microtextures is investigated using a continuous strip drawing test. This strip drawing test allows reproducing typical loads of sheet metal forming processes. The use of individual sheet metal strips as well as sheet metal coils for continuous testing is possible. In addition, a cleaning and oiling module is integrated so that identical surface conditions are guaranteed for all test series. In the test stand, the required normal force is

DOI: https://doi.org/10.26799/cp-sict-plasmatech-tribology-2023

applied by four hydraulic cylinders. After closing the tool holder and applying the force, the sheet is pulled through the closed tool by a gripper. Each stroke has a length of 100 mm, whereby the drawing speed is adjustable and amounts to a maximum of $100\,\mathrm{mm/s}$. The tool consists of two flat friction jaws with a size of $(40 \cdot 40)\ mm^2$ with rounded edges. It is therefore possible to generate load collectives that produce wear patterns relevant to industrial forming processes and make them accessible for extensive investigations [8]. The resulting coefficient of friction (COF) can be calculated as follows:

$$\mu = \frac{F_R}{2 \cdot F_N} \tag{1}$$

The test stand allows the generation of friction paths with a length of several thousand strokes. The tribological system used for the present study is shown in table 1.

Table 1: Tribological system used for strip drawing test

tool		**sheet**			**lubricant**		
material	hardness h [HRC]	material	strength Rm [MPa]	thickness s [mm]	type	viscosity ϑ [mm]	amount $g\ \left[\frac{g}{mm^2}\right]$
1.2379	60	HC420LA	530 ± 60	1.5	RhenusSU	200(40°C)	1

2.2 Laser Texturing

A pulsed frequency-doubled nanosecond laser with ND:YVO medium and a wavelength of $\lambda = 532\,\mathrm{nm}$ by *3D-Micromac* was used for texturing. In a preliminary parameter study, the optimal parameters for feed rate ($vf = 20\,\mathrm{mm/s}$), frequency ($f_{LT} = 20\,\mathrm{kHz}$), and power ($I = 8\,\mathrm{W}$) were determined for the tool material used. According to previous studies, an offset texturing pattern with equidistant spacing was chosen [9]. The smallest repeating texturing element thus corresponds to an isosceles triangle. The size of a single dimple was kept constant over all test series and corresponds to a depth of $d_{LT} = 49.13 \pm 7.3\ \mu m$ and a diameter of $w_{LT} = 7.83 \pm 0.47\ \mu m$ which results in an aspect ratio of $a_{LT} = 0.16$. To achieve different degrees of coverage, the spacing of the dimples was varied. In this study, both friction jaws of a dedicated pair were textured. For this purpose, the friction jaws were first ground and then polished. Afterwards, the jaws were textured. As a result of the laser texturing and material solidification, the surface of the imprint was polished again to remove any discontinuities.

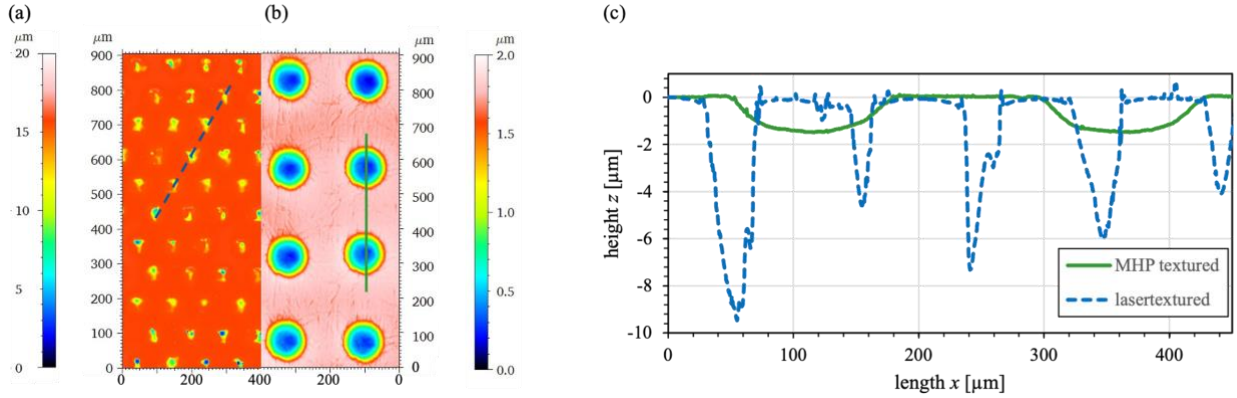

Figure 1: Surface topographies of (a) laser textured (b) MHP textured friction jaws and (c) corresponding profile sections

2.3 Texturing by Machine Hammer Peening

Machine hammer peening (MHP) was considered as an additional method for texturing surfaces. MHP is commonly used for smoothing technical surfaces and introducing residual compressive stresses as well as causing strain hardening in the surface layer of the components treated [10, 11]. The effects are caused by an oscillating

DOI: https://doi.org/10.26799/cp-sict-plasmatech-tribology-2023

hammerhead that is guided over the surface by a machining center. By using specially shaped micro-tip hammerheads, surface textures can be applied onto the surface in the same process step [12, 13]. The used electromechanical MHP system from *accurapuls* allows targeted control of the impact frequency f_I as well as the impact energy. In combination with the feed vf of the machining center and the stroke height h, the trajectory of the hammerhead can be fully controlled, and deterministic surfaces textures can be produced. The micro-milled microtip has a height of 10 µm, an upper diameter of 100 µm, and a flank angle of about 85°. This hammerhead was used to machine polished friction jaws at a frequency of $f_{MHP} = 100$ Hz and intensity of $I = 30$ % with an equidistant texturing. The resulting indentations have a diameter of $w_{MT} = 133 \pm 1.2$µm and a depth of $d_{MT} = 1.5 \pm 0.1$ µm. The aspect ratio thus generated is $a_{MT} = 0.01$. In addition, a conventional tungsten carbide hammerhead without microtip was used to smoothen a ground surface with a frequency of 150 Hz and an intensity of 50 %. MHP machining reduced the Rz value from the initial 8.3 µm to 1.2 µm. The resulting surface topographies are shown in Fig. 1.

2.4 Experimental Design

At the strip drawing test stand, MHP texturing was compared to laser texturing by a nanosecond laser as well as polished friction jaw pairs as an industrial standard. For this purpose, both different degrees of coverage and aspect ratios were considered for the texturing patterns. In order to map different load conditions of the sheet metal forming, after 30 strokes at a resulting contact normal stress (CNS) of 7 MPa the normal force F_N of the system was incrementally increased every 15 strokes up to a CNS of 14 MPa. Every combination of polished and laser-textured friction jaw pairs was manufactured and investigated three times for statistical validation. Due to heavy wear of the microtip of the MHP tool, only one friction jaw pair could be textured and examined. Polished surfaces have a roughness of $Rz = 32.2 \pm 0.6$ nm and $Ra = 3.5 \pm 0.3$ nm. The test matrix is shown in table 2.

Table 2: Texturing parameters used for strip drawing tests

parameter	laser texturing	MHP	polished
coverage [%]	8, 16, 24	smoothed, 22	-
aspect ratio [-]	0.16	0.011	-
CNS [MPa]		7, 8, 9, 10, 12, 14	

3 Results and Discussion

Fig. 2 shows the results of the continuous strip drawing tests with increasing CNS for laser texturing and MHP processing compared with polished friction jaws. One of the polished friction jaw pairs examined failed after only a few strokes, which is why it was not included in the illustration. It can generally be seen that the majority of the determined COF curves are below the polished reference. The ground pair of friction jaws smoothed by MHP also fails after a friction length of 1830 mm, while the pair of tools textured by micro-tip MHP shows a significantly reduced coefficient of friction compared to the polished reference. The earlier failure of the ground + smoothed specimen is mainly due to its comparatively high roughness and the associated micro-contacts as well as increased local CNS, which provoke severe wear.

DOI: https://doi.org/10.26799/cp-sict-plasmatech-tribology-2023

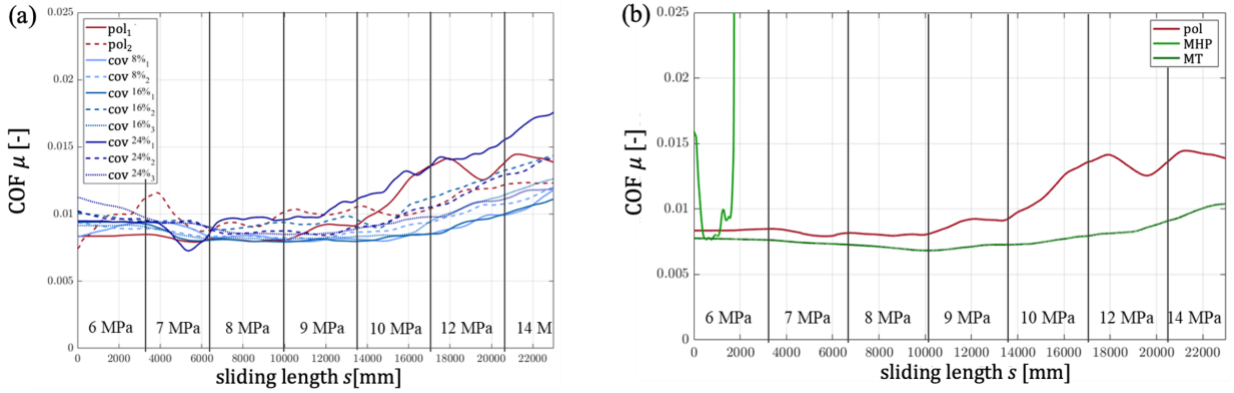

Figure 2: COF for continuous strip drawing tests of (a) laser textured friction jaws with different coverages and (b) MHP as well as MHP with micro texturing (MT) processed friction jaws

To get a more detailed picture, in Fig. 3 the COFs for the different stress levels are summarized as mean values and their relative change compared to the polished reference is shown. For the laser textured friction jaws, a coverage of 8 and 16 % reduces the COF. A coverage of 24 % leads to an increase in COF. It can also be seen that coverage of 8 % contributes to the highest reduction in the textured samples. The local minimum is −18 % at 12 MPa and for higher CNS the reduction decreases again.

The MHP textured (MT) sample with coverage of 22 % shows an analogous pattern for friction reduction for increasing CNS with a local minimum at 12 MPa. Although the coverage is significantly higher than the optimum of the laser textured tools, a reduction of the COF by 31 % can be achieved.

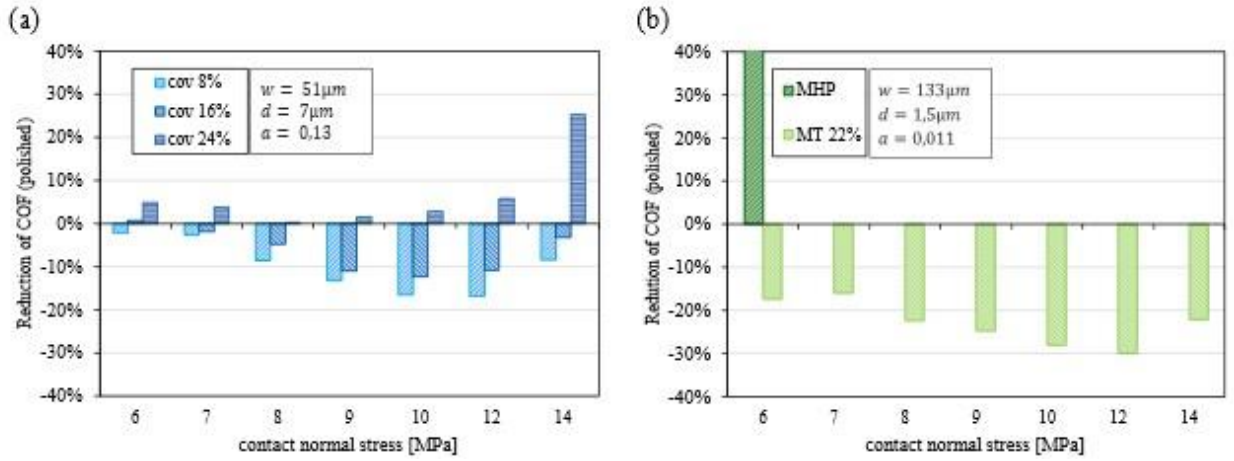

Figure 3: Relative reduction of COF compared to a polished surface for increasing CNS for (a) laser textured surfaces and (b) microtextured surfaces by MHP

The micro dimples introduced on the tool surfaces act as a lubricant reservoir [14]. In combination with the high relative velocities of 100 mm/s, they are able to form hydrodynamic pressure pockets, which contribute to a reduction of the COF compared to untextured surfaces [15, 16]. For cavities introduced by laser texturing, the optimum coverage appears to be around 8%. An increase leads to a decrease of the effect. In the case of cavities produced by MHP, on the other hand, a coverage of 22% could contribute to a significantly increased reduction of COF. Since in both cases symmetrical spheres were used as dimples, the reason for this development seems to be the aspect ratio. A lower aspect ratio favors better rheological pressure conditions in the tribological system due to the hydrodynamic lift effect, resulting in a significantly reduced COF [17]. The correlation of aspect ratio and degree of coverage needs to be investigated in detail in further work.

DOI: https://doi.org/10.26799/cp-sict-plasmatech-tribology-2023

4 Conclusion

The influence of lubricant pockets generated by laser texturing and MHP on the coefficient of friction were investigated. Therefore, a strip drawing test was used. From the results, it can be concluded that:

- the dimples created by MHP have a higher surface integrity and a more defined fine shape than those created by laser texturing
- a beneficial manipulation of the friction behavior with different texturing processes is possible
- for the tribological system considered, the optimum operating point of the structures is at a CNS of 12 MPa
- lower aspect ratios lead to a shift in optimal coverage to higher densities and can contribute to a higher reduction in COF compared to larger aspect ratios

5 Acknowledgements

The authors thank the European Research Association for Sheet Metal Working (EFB) and the German Federation of Industrial Research Associations “Otto von Guericke” (AiF) a well as all participating companies for their support in the project “Tribological optimization of stamping punches through microtexturing using machine hammer peening.”

6 References

[1] O. Bouaziz, H. Zurob, and M. Huang, “Driving force and logic of development of advanced high strength steels for automotive applications,” *Steel research international*, vol. 84, no. 10, pp. 937–947, 2013.
[2] J. Galán, L. Samek, P. Verleysen, K. Verbeken, and Y. Houbaert, “Advanced high strength steels for automotive industry,” *REVMETAL*, vol. 48, no. 2, pp. 118–131, 2012, doi: 10.3989/revmetalm.1158.
[3] American Iron and Steel Institute, *ULSAB Final Report*. Washington D.C., 1998.
[4] T. Trzepieciński, “Recent Developments and Trends in Sheet Metal Forming,” *Metals*, vol. 10, no. 6, p. 779, 2020, doi: 10.3390/met10060779.
[5] C. Herrera, A. Bauch, and D. Peterle, “Development of High-Mn High Strength Steel for Electric Vehicles,” *Berg Huettenmaenn Monatsh*, vol. 167, no. 11, pp. 526–529, 2022, doi: 10.1007/s00501-022-01293-5.
[6] M. Sigvant *et al.*, “Friction in sheet metal forming: influence of surface roughness and strain rate on sheet metal forming simulation results,” *Procedia Manufacturing*, vol. 29, pp. 512–519, 2019, doi: 10.1016/j.promfg.2019.02.169.
[7] H. Hoffmann, C. Hwang, and K. Ersoy, “Advanced Wear Simulation in Sheet Metal Forming,” *CIRP Annals*, vol. 54, no. 1, pp. 217–220, 2005, doi: 10.1016/s0007-8506(07)60087-0.
[8] M. Christiany and P. Groche, “Reproducibility of Wear Tests and the Effect of Load on Tool Life in Sheet Metal Forming,” *AMR*, vol. 1018, pp. 293–300, 2014, doi: 10.4028/www.scientific.net/AMR.1018.293.
[9] K. Kitamura, T. Makino, M. Nawa, and S. Miyata, “Tribological effects of punch with micro-dimples in blanking under high hydrostatic pressure,” *CIRP Annals*, vol. 65, no. 1, pp. 249–252, 2016, doi: 10.1016/j.cirp.2016.04.133.
[10] W. L. Chan and H. K. F. Cheng, “Hammer peening technology—the past, present, and future,” (in En;en), *Int J Adv Manuf Technol*, vol. 118, 3-4, pp. 683–701, 2022, doi: 10.1007/s00170-021-07993-5.
[11] V. Schulze, F. Bleicher, P. Groche, Y. B. Guo, and Y. S. Pyun, “Surface modification by machine hammer peening and burnishing,” *CIRP Annals*, vol. 65, no. 2, pp. 809–832, 2016, doi: 10.1016/j.cirp.2016.05.005.
[12] P. Sticht, J. Hohmann, and P. Groche, “Effects of Machine Hammer Peened Surface Textures on the Tribological Behavior of Stamping Tools,” in 2020, pp. 108–120. [Online]. Available: https://link.springer.com/chapter/10.1007/978-981-15-0054-1_12
[13] M. Steitz, P. Stein, and P. Groche, “Influence of Hammer-Peened Surface Textures on Friction Behavior,” (in En;en), *Tribol Lett*, vol. 58, no. 2, pp. 1–8, 2015, doi: 10.1007/s11249-015-0502-9.
[14] Shimizu, Kobayashi, Vorholt, and Yang, “Lubrication Analysis of Micro-Dimple Textured Die Surface by Direct Observation of Contact Interface in Sheet Metal Forming,” *Metals*, vol. 9, no. 9, p. 917, 2019, doi: 10.3390/met9090917.

[15] D. Gropper, L. Wang, and T. J. Harvey, "Hydrodynamic lubrication of textured surfaces: A review of modeling techniques and key findings," *Tribology International*, vol. 94, pp. 509–529, 2016, doi: 10.1016/j.triboint.2015.10.009.
[16] M. Wakuda, Y. Yamauchi, S. Kanzaki, and Y. Yasuda, "Effect of surface texturing on friction reduction between ceramic and steel materials under lubricated sliding contact," *Wear*, vol. 254, 3-4, pp. 356–363, 2003, doi: 10.1016/s0043-1648(03)00004-8.
[17] D. B. Hamilton, J. A. Walowit, and C. M. Allen, "A Theory of Lubrication by Microirregularities," *Journal of Basic Engineering*, vol. 88, no. 1, pp. 177–185, 1966, doi: 10.1115/1.3645799.

Proceedings of the SICT / Plasma Tech / Tribology 2023 International Joint Conferences
Lisbon, Portugal – April 26 – 28, 2023
DOI: https://doi.org/10.26799/cp-sict-plasmatech-tribology-2023

High-Fidelity Fluid-Structure Interaction Simulation of Elastohydro dynamically Lubricated Line Contact

Nicolas Delaissé[1,*], Peyman Havaej[2], Dieter Fauconnier[2,3], Joris Degroote[1,3]

[1]Department of Electromechanical, Systems and Metal Engineering, Ghent University
Sint-Pietersnieuwstraat 41, 9000 Ghent, Belgium
[2]Department of Electromechanical, Systems and Metal Engineering, Ghent University
Technologiepark Zwijnaarde 46, 9052 Zwijnaarde, Belgium
[3]Flanders Make @ UGent – Core Lab MIRO, Belgium

Abstract

This work simulates an elastohydrodynamically lubricated line contact using high-fidelity computational fluid dynamics (CFD) and computational structural mechanics (CSM) solvers. The hydrodynamic and thermal lubricant behaviour is accurately captured by inclusion of cavitation, an equation of state, a viscosity model, a shear thinning equation and models for the thermal conductivity and heat capacity. The software used in this work are open source.

Keywords: elastohydrodynamic lubrication (EHL), fluid-structure interaction (FSI), multi-physics coupling, partitioned algorithm, high-fidelity simulation, OpenFOAM, KratosMultiphysics

1. Introduction

The very thin films (50 nm – 1 µm) and extreme pressure values (1 – 3 GPa) in elastohydrodynamically lubricated contacts, render experimental research of the fundamental effects in the contact very challenging. For this reason, investigation of elastohydrodynamic behaviour is often numerical in nature. Due to the interaction between the local solid deformation and the pressure build-up in the lubricant, a coupled calculation is required, i.e., a fluid-structure interaction (FSI) simulation.

Historically, these simulations are conducted with lower order models, e.g., the Reynolds equations for the lubricant and the Boussinesq approach for the deformation [1-4]. Unavoidably, the corresponding assumptions introduce errors in the results [5]. This work aims for increased accuracy by using high-fidelity solvers both in soft EHL, through the inclusion of inertial effects absent in the Reynolds equations, and in hard EHL, since the Boussinesq approximation is inexact for large deformations. The focus is a two-dimensional simulation of a line contact using computational fluid dynamics (CFD) and computational structural mechanics (CSM) [6-8].

While this work focusses on the methodology, the final goal of this high-fidelity numerical approach is to gain insight into the physics of elastohydrodynamically lubricated contacts and to investigate their behaviour under varying load and varying speed.

The next section provides an overview of the governing equations in both the fluid and structure domain, as well as the coupling conditions on the common interface. Section 3 focusses on the implementation. Thereafter, some results are included in Section 4, and, finally, Section 5 presents the conclusion.

2. Governing equations

2.1. Flow equations

The flow velocity $\vec{v}$, pressure p and temperature T follow from the Navier-Stokes equations.

$$\frac{\partial \rho_f}{\partial t} + \nabla \cdot \rho_f \vec{v} = 0 \quad (1)$$

$$\frac{\partial \rho_f \vec{v}}{\partial t} + \nabla \cdot \rho_f \vec{v}\vec{v} = \nabla \cdot \vec{\tau} - \nabla p \quad (2)$$

$$\frac{\partial \rho_f h}{\partial t} + \nabla \cdot \rho_f h \vec{v} = \nabla \cdot \kappa \nabla T + \vec{\tau} : \nabla \vec{v} + \frac{Dp}{Dt} \quad (3)$$

The continuity equation (1) relates the variable density ρ_f to the velocity field. The momentum equation (2) balances the transport of momentum against the action of the stress tensor, which is split in a pressure and

DOI: https://doi.org/10.26799/cp-sict-plasmatech-tribology-2023

viscous contribution $\overleftrightarrow{\tau}$. The viscous stress tensor is assumed to the product of the pure shear tensor $\overleftrightarrow{\dot{\gamma}}$, which is the deviatoric part of $\nabla\vec{v}$, and 2μ, with μ the dynamic viscosity depending on pressure, temperature and shear rate. Note that gravity and other body forces are negligible. The energy equation is rewritten to express the conservation of thermal energy [9]: the transport of the product of ρ_f with enthalpy h is equated to the conduction with thermal conductivity κ, dissipation and pressure action. The material derivative $\frac{Dp}{Dt}$ equals $\frac{\partial p}{\partial t} + \vec{v} \cdot \nabla p$.

Cavitation is included using a homogeneous equilibrium model (HEM), which assumes that in every point of the continuum, the liquid and vapour phase are in mechanical and thermodynamic equilibrium, meaning they have equal velocity, pressure and temperature [10, 11]. With decreasing pressure, this model maintains a specified cavitation pressure in the cavitating region by converting liquid into vapour. The vapour and liquid volume fraction are denoted as α_v and α_l, respectively. The resulting density, viscosity, thermal conductivity, heat capacity and enthalpy are expressed as weighted average.

$$\rho_f = \alpha_l \rho_{f,l} + \alpha_v \rho_{f,v} \qquad (4)$$

$$\mu = \alpha_l \mu_l + \alpha_v \mu_v \qquad (5)$$

$$\kappa = \alpha_l \kappa_l + \alpha_v \kappa_v \qquad (6)$$

$$\rho_f c_p = \alpha_l \rho_{f,l} c_{p,l} + \alpha_v \rho_{f,v} c_{p,v} \qquad (7)$$

$$\rho_f h = \alpha_l \rho_{f,l} h_l + \alpha_v \rho_{f,v} h_v \qquad (8)$$

The density in function of p and T is given by the equation of state, here the Tait equation. The variation of viscosity with p and T is modelled with the Doolittle equation. For details on both, refer to [12] and [13]. Shear-thinning is included by a Carreau model with limiting stress [14]. Furthermore, also the variation of thermal conductivity κ and c_p with p and T is accounted for [15].

2.2. Structural equations

The displacement $\vec{u}$ of the structure follows the conservation of momentum from a total Lagrangian point of view under the assumption of small displacements.

$$\rho_s \frac{d^2\vec{u}}{dt^2} = \nabla \cdot \overleftrightarrow{\sigma} \qquad (9)$$

In this equation, $\overleftrightarrow{\sigma}$ is the Cauchy stress tensor, and the solid density ρ_s is considered constant. Note that no body forces are included. Stresses and strains are linked by a linear elastic material model with modulus of elasticity E and Poisson's ratio ν. In this work, simulations are two-dimensional and a plane strain approach is followed.

2.3. Coupling conditions

The coupling of the fluid and structure domain requires matching values of velocity and forces on the fluid-structure interface. These kinematic and dynamic equilibrium conditions on the interface are expressed by

$$\vec{v} = \frac{d\vec{u}}{dt} \quad \text{and} \quad \left(-p\overleftrightarrow{I} + \overleftrightarrow{\tau}\right) \cdot \vec{n}_f = -\overleftrightarrow{\sigma} \cdot \vec{n}_s, \qquad (10)$$

where $\vec{n}_f$ and $\vec{n}_s$ are the outward pointing normal of the fluid and structure domain, respectively.

Since no thermal equation is solved for the structure, no coupling conditions are required for temperature and heat flux. This way, it is assumed that the roller has a constant temperature, which is then used as boundary condition for the flow domain on the FSI-interface. Both the time scale of the thermal transport in the roller, which is significantly larger than the mechanical and hydrodynamic time scales, and the fact that, in reality, the contact point on the roller continuously changes due to its rotation support this assumption.

2.3. Partitioned approach

As opposed to the monolithic approach, in partitioned FSI, separate flow and structure solvers are coupled through the exchange of data on their common interface, such that the solvers can be considered black boxes. Fulfilling the coupling conditions on the fluid-structure interface, requires iterating between the flow and structure solver in every time step. With a Dirichlet-Neumann partitioning, the fluid mesh is moved according to a displacement of the fluid-structure interface. After calculating the flow problem, the resulting pressure and traction are applied as boundary condition to the structure solver on the fluid-structure interface. Running the structure solver results in a new displacement of the common interface.

DOI: https://doi.org/10.26799/cp-sict-plasmatech-tribology-2023

Convergence of the coupling loop in every time step is provided by a coupling algorithm that updates the displacement in between coupling iterations [16]. In this work, IQN-ILSM with reuse as surrogate model (reuse parameter q = 5) will be used [17].

3. Implementation

The open-source packages OpenFOAM 8 and KratosMultiphysics 9.1 Structural Mechanics application are used to model flow and structure respectively, and their coupling is achieved through the open-source package CoCoNuT [16]. The used meshes and boundary conditions are presented in Fig. 1.

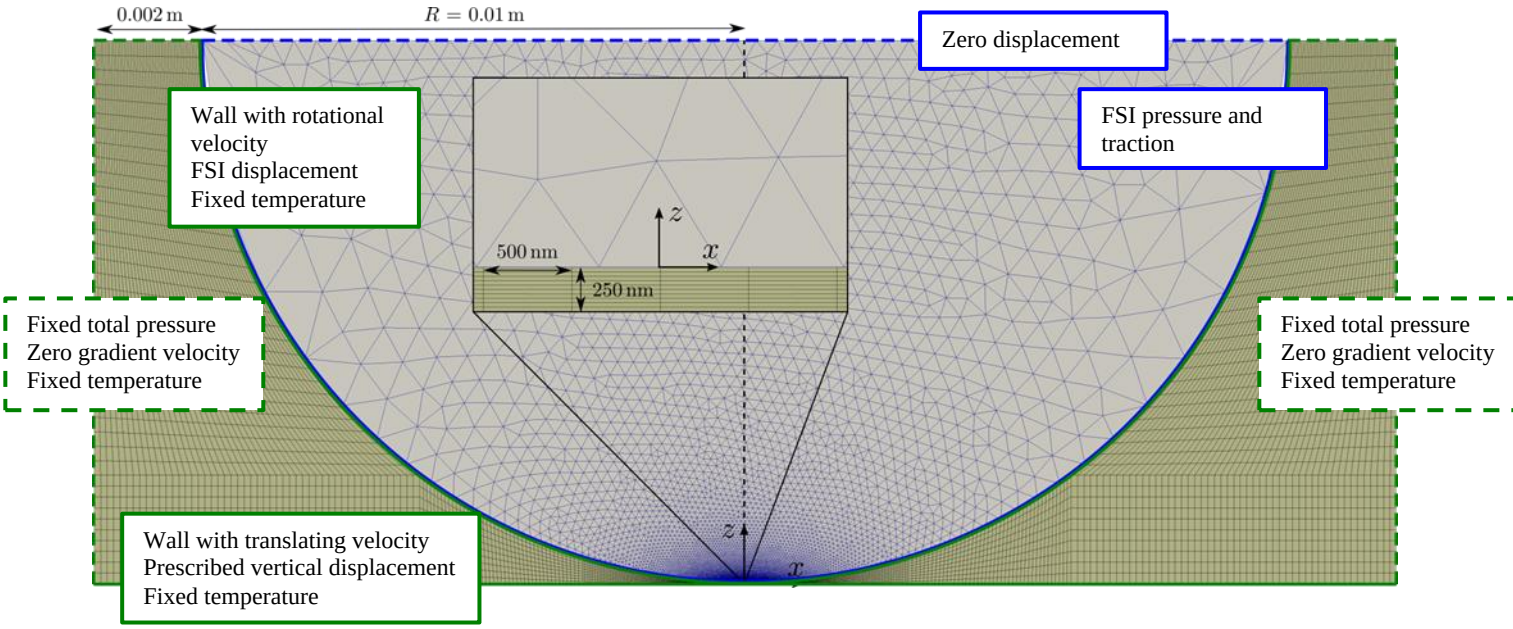

Fig. 1: Mesh and boundary conditions for the CFD and CSM solver. The fixed total pressure value is 10^5 Pa, and the fixed temperature value 313.5 K.

While the structure solver is out-of-the-box and rather straightforward, the flow solver requires modifying an existing solver. The OpenFOAM solver used to model the lubricant behaviour is an adaptation of cavitatingFoam, which is part of the standard OpenFOAM installation and includes an HEM model accounting for a constant compressibility ψ of both the liquid and vapour phase. While this approach is sufficient to model the vapour phase, it is not for the liquid phase. The implementation of the lubricant models from Section 2.1 necessitated the introduction of a variable density and a temperature equation. Moreover, new boundary conditions were required for the walls to combine a prescribed translating or rotating velocity with displacement, either prescribed or originating from the FSI coupling.

4. Results

The non-conformal line contact is simulated in two dimensions (2D) to reduce the computational cost. One of the contacting solids is assumed to be a rigid flat plate, and the other has an equivalent radius with a modified elasticity modulus of 105 GPa and Poisson's ratio 0.3, resulting in the so-called reduced geometry. The geometrical parameters are indicated in Fig. 1. The used lubricant is squalane (SQL). For its properties and corresponding parameters in the lubricant models refer to [18] and to [15] for κ and c_p. The prescribed velocity of the walls is 2.5 m/s for both surfaces (pure rolling). Instead of solving a load balancing loop to obtain the vertical displacement of the rigid plate from a prescribed force, in this simulation, the displacement has been specified directly.

After moving the plate upward to 1.735 µm above the initial position, with decreasing steps in a time of 0.21 ms, and holding it steady at that position for 0.16 ms, a steady state is reached. Fig. 2 shows the resulting pressure in the contact. The used time step size is 50 ns.

DOI: https://doi.org/10.26799/cp-sict-plasmatech-tribology-2023

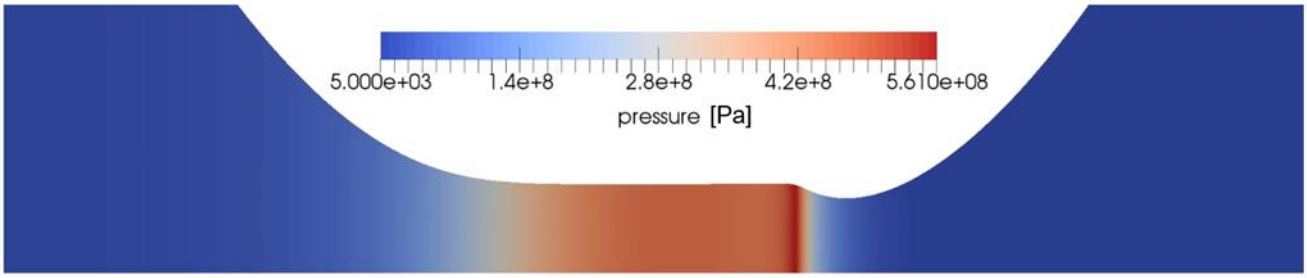

Fig. 2: Contour plot of pressure in the contact. The figure has been scaled in the vertical direction with a factor 100.

5. Conclusion

This works presents a new combination of high-fidelity open source solvers for the simulation of an EHL line contact. The ultimate goal is to use this approach to gain insight in the lubrication behaviour under variable load and rotational velocity, or provide accurate input for a faster model to be used in multi-body simulations.

References

1. D. Dowson and G. R. Higginson, *Elasto-hydrodynamic lubrication*. Pergamon Press, 1977, p. 235.
2. B. J. Hamrock, S. R. Schmid, and B. O. Jacobson, *Fundamentals of fluid film lubrication*. Marcel Dekker, 2004, p. 699.
3. C. H. Venner, "Multilevel solution of the EHL line contact," Universiteit Twente, 1991.
4. H. P. Evans and T. G. Hughes, "Evaluation of deflection in semi-infinite bodies by a differential method," *Proceedings of the Institution of Mechanical Engineers, Part C: Journal of Mechanical Engineering Science*, vol. 214, no. 4, pp. 563-584, 2000.
5. L. Scurria, T. Tamarozzi, O. Voronkov, and D. Fauconnier, "Quantitative analysis of Reynolds and Navier–Stokes based modeling approaches for isothermal Newtonian elastohydrodynamic lubrication," *Journal of Tribology*, vol. 143, no. 12, 2021.
6. M. Hartinger, M.-L. Dumont, S. Ioannides, D. Gosman, and H. Spikes, "CFD modeling of a thermal and shear-thinning clastohydrodynamic line contact," *Journal of Tribology*, vol. 130, no. 4, 2008.
7. A. Hajishafiee, A. Kadiric, S. Ioannides, and D. Dini, "A coupled finite-volume CFD solver for two-dimensional elasto-hydrodynamic lubrication problems with particular application to rolling element bearings," *Tribology International*, vol. 109, pp. 258-273, 2017.
8. K. Singh *et al.*, "Fluid–structure interaction modeling of elastohydrodynamically lubricated line contacts," *Journal of Tribology*, vol. 143, no. 9, 2021.
9. R. B. Bird, W. E. Stewart, and E. N. Lightfoot, *Transport phenomena*. Wiley, 2001.
10. H. B. Stewart and B. Wendroff, "Two-phase flow: models and methods," *J Comput Phys*, vol. 56, no. 3, pp. 363-409, 1984.
11. F. P. Kärrholm, H. Weller, and N. Nordin, "Modelling injector flow including cavitation effects for diesel applications," in *Proceedings of FEDSM2007, 5th Joint ASME/JSME Fluids Engineering Conference*, San Diego, 2007/01 2007: ASMEDC.
12. T. J. Zolper, S. Bair, and K. Horne, "Revisiting the ASME pressure-viscosity report using the Tait-Doolittle correlations," *Journal of Tribology*, vol. 143, no. 6, 2020.
13. P. Havaej, J. Degroote, and D. Fauconnier, "Sensitivity of TEHL simulations to the use of different models for the constitutive behaviour of lubricants," *Lubricants*, vol. 11, no. 3, p. 151, 2023.
14. S. Bair, C. McCabe, and P. T. Cummings, "Calculation of viscous EHL traction for squalane Using molecular simulation and rheometry," *Tribology Letters*, vol. 13, no. 4, pp. 251-254, 2002.
15. M. Björling, W. Habchi, S. Bair, R. Larsson, and P. Marklund, "Friction reduction in elastohydrodynamic contacts by thin-layer thermal insulation," *Tribology Letters*, vol. 53, no. 2, pp. 477-486, 2014.
16. N. Delaissé, T. Demeester, R. Haelterman, and J. Degroote, "Quasi-Newton methods for partitioned simulation of fluid-structure interaction reviewed in the generalized Broyden framework," *Archives of Computational Methods in Engineering*, 2023.

DOI: https://doi.org/10.26799/cp-sict-plasmatech-tribology-2023

17. N. Delaissé, T. Demeester, D. Fauconnier, and J. Degroote, "Surrogate-based acceleration of quasi-Newton techniques for fluid-structure interaction simulations," *Computers & Structures,* vol. 260, p. 106720, 2022.
18. S. Bair, "Reference liquids for quantitative elastohydrodynamics: selection and rheological characterization," *Tribology Letters,* vol. 22, no. 2, pp. 197-206, 2006.

Proceedings of the SICT / Plasma Tech / Tribology 2023 International Joint Conferences
Lisbon, Portugal – April 26 – 28, 2023
DOI: https://doi.org/10.26799/cp-sict-plasmatech-tribology-2023

Dedicated Hybrid Turbo GDI Engine with Low Friction Loss

Q. Zhou
Changan UK R&D Centre, 3700 Parkside, Birmingham Business Park, B37 7YG, UK

Abstract

The Dedicated Hybrid Engine (DHE) development attracted increased attentions from OEMs. With the reduced engine power demand and narrowed engine operating speed range, it created a friendly environment for the low friction technologies to be implemented without further cost implication. This paper presented the friction road map from the current production engine to the new dedicated hybrid engine. Extensive analyses were run to optimize the crankshaft design so the small bearings can be used without compromising the durability. The valvetrain was re-designed to enable the use of the lightest valve spring. Furthermore, the new turbo selection allowed the use of low viscosity oil of 0W12. The combined effort of these changes, plus the use of electric oil pump helped the DHE to reach the lowest friction level of 0.29 bar FMEP at 2000 rpm under the motored stripped condition

Keywords: Low friction valvetrain & cranktrain, thin oil.

Introduction

There is big shift in the global vehicle production towards the battery electric vehicle (BEV), hybrid electric vehicle (HEV), plug-in hybrid electric vehicle (PHEV) and range extender (REEV) in recent years. Especially in 2022 China market, the massive surge of BEV, HEV, PHEV and REEV sales made the conventional internal combustion engine (ICE) powered vehicle much less attractive. To meet this fast changing market demand, there is an increasing demand to develop the dedicated hybrid engine (DHE) with high thermal efficiency for HEV, PHEV and REEV platforms[1-3]

The DHE has a very different operating environment, compared with the conventional engine. For example, the conventional gasoline engines' typical operation range covers from idle (~600 to 750 rpm) to max speed of 6300 to 7000 rpm. Usually, the moving parts, such as the piston, conrod, bearing, spring, valve, cam, tappet or follower etc., are designed to survive the maximum speed and maximum power condition. For the DHE specially used on P13 platform, the operating speed range is much narrower, typically between 1200 and 4800 rpm. That means, those components designed for conventional gasoline engine are likely over-engineered for DHE.

Figure 1 shows the torque curves of the conventional gasoline engine NE14 and the proposed DHE. Apart from the speed range change, the torque requirement is much reduced for DHE. The reason for the reduced torque requirement was due to the use of powerful twin e-motors. The low speed torque of the vehicle is now supplied by the e-motor.

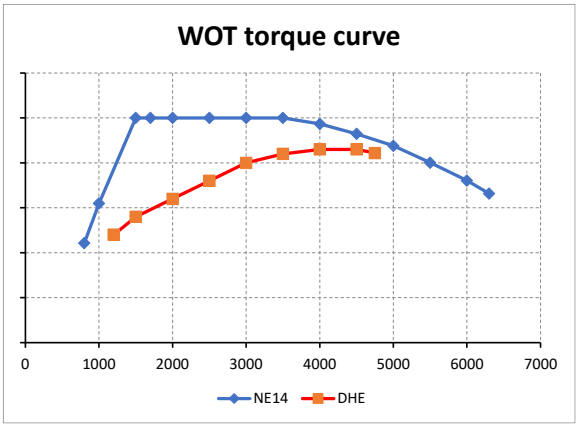

Figure1: NE14 and DHE torque curve

DOI: https://doi.org/10.26799/cp-sict-plasmatech-tribology-2023

To maximise the benefit of the reduced operating speed range and reduced torque of the DHE, all the moving parts, such as the crankshaft, bearing, conrod, piston, intake and exhaust valves, cam, follower, oil pump, fuel pump (including tappet and spring) and turbocharger etc., must be re-designed. The focus when re-designing these parts is on the change of the inertial load due to the speed change, the reduced fuel flow at the low speed and the introduction of thin oil (0W12). In all cases, components' durability standard must be maintained.

Friction reduction road map:
Most of the engine's friction loss comes from the cranktrain, valvetrain, water pump and oil pump. The Figure 2 shows the production NE14 engine friction loss breakdown at 1000 and 5500 rpm, with 0W20 at 90 °C coolant and oil temperature. The NE14 engine has 73.5 mm bore diameter and 82 mm stroke, making it 1.4L for a four-cylinder engine.

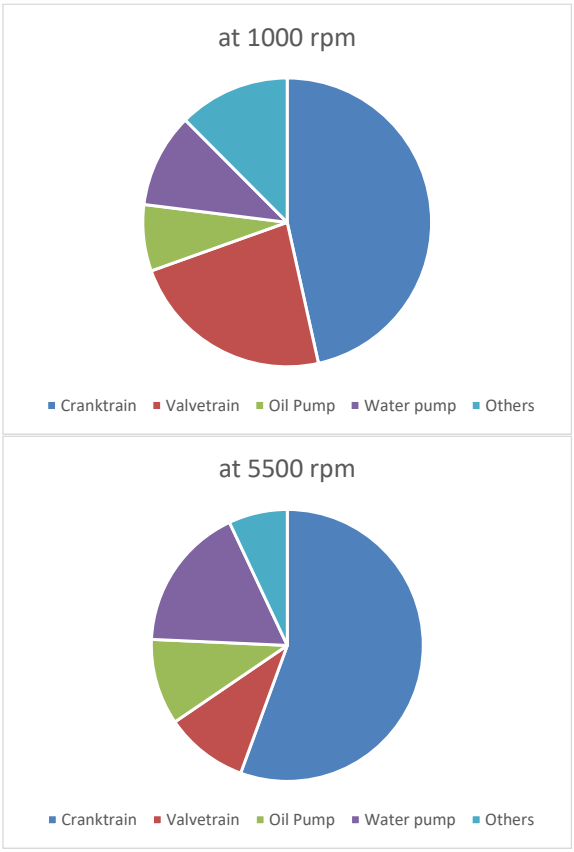

Figure 2: Friction breakdown of NE14

DOI: https://doi.org/10.26799/cp-sict-plasmatech-tribology-2023

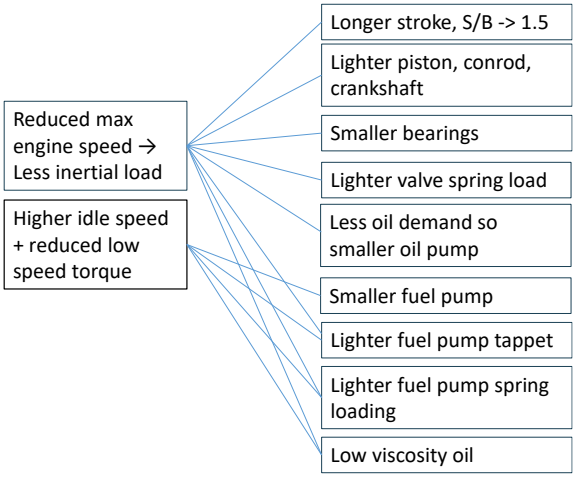

Figure 3: Effect of engine operating boundary changes on system/component design

Migrating from a conventional gasoline engine to a dedicated hybrid engine will create opportunities for component and system optimization. Figure 3 shows the potential affected components for re-designing. Since the decision was taken to use electric water pump and electric oil pump for the DHE project, this left the cranktrain and valvetrain to be focused on for the re-designing exercise.

Cranktrain:

For NE14, the engine was designed with the max engine speed at 6300 rpm. The crankshaft main journal bearing diameter is 48 mm, conrod big end bearing diameter 44 mm, making the crankshaft bearing overlap to be 1.12. For the DHE, the following product assumptions were proposed considering the new speed range and torque requirement.

Firstly, the stroke to bore was increased from NE14's 1.12 to DHE's 1.45 (bore diameter 69 mm and stroke 100 mm). Although this change is mainly driven by improving the combustion efficiency, it also has positive impact on friction. The piston diameter reduction from 73.5 to 69 mm reduced the gas loading on piston by 12% under the same in-cylinder gas pressure. The smaller diameter piston also makes the piston lighter. This, combined with the reduced maximum engine speed, makes the inertial loading on conrod, piston pin and crankshaft much smaller. This is the big enabler for the smaller conrod big end bearing diameter.

Secondly, to balance the crankshaft stiffness requirement and friction reduction aspiration, the main bearing diameter was maintained to be 48 mm while the conrod big end bearing diameter was reduced from 44 to 40 mm for DHE. Figure 4 shows the crankshaft CAD model. Although this reduced the crankshaft bearing overlap to 0.88, the analysis showed crankshaft torsional behavior and bearing minimum oil film thickness (MOFT) are all within healthy level. Additionally, the small end used DLC coated pin without brass bush. The main and conrod big end journals are all superfinished with Ra < 0.05 micron. The three piston rings total tangential load is 22% less than that of production NE engine. These positive changes, together with the conrod big engine diameter reduction and low viscosity oil helped the cranktrain friction to reach a new low level.

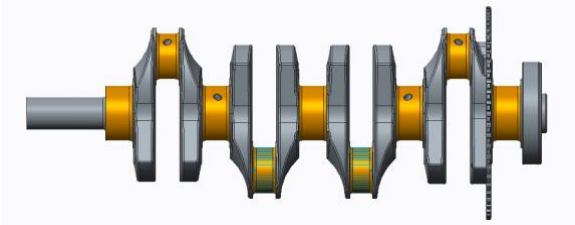

Figure 4: DHE crankshaft

Valvetrain:

DOI: https://doi.org/10.26799/cp-sict-plasmatech-tribology-2023

The biggest friction improvement of this DHE engine came from the re-design of the valvetrain layout. Although both NE and DHE were designed with roller finger follower (RFF) and hydraulic lash adjuster (HLA), the two designs differed from each other in many aspects.

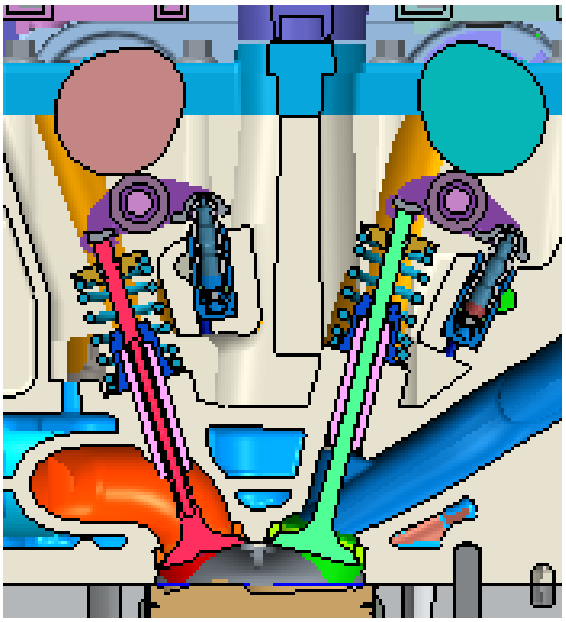

(a) NE14 valvetrain layout

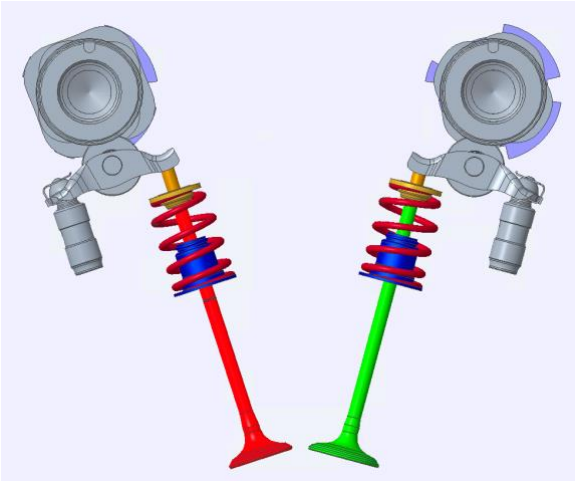

(b) DHE valvetrain layout

Figure 5: Valvetrain layouts of NE to DHT

Firstly, the new valvetrain layout plus the reduced max engine speed enabled the valve spring preload to be reduced from production NE engine's 190 N to 107 N, a reduction of 44%. Secondly, thanks to the new valve acceleration profile, the valve spring's stiffness was reduced from 25 to 9.8 N/mm, 60.8% reduction. For the maximum valve lift of 10 mm, the peak spring load of the DHE is 205 N only, a 53% reduction from the production engine's 440 N peak valve spring load. These changes converted to a 28% friction reduction for the valvetrain alone at 2000 rpm engine speed. The old and new valvetrain layouts are presented in Figure 5.

Table 1: NE vs DHE valvetrain design parameters

DOI: https://doi.org/10.26799/cp-sict-plasmatech-tribology-2023

	NE	DHE	**Reduction, %**
spring preload, N	190	107	**43.68**
Spring stiffness, N/mm	25	9.8	**60.80**
Max spring load, N	440	205	**53.41**

Table 1 listed the key design parameter difference between NE and DHE valvetrain.

Figure 6 shows the valve lift profiles and velocity curves. For the intake valve, a constant lift of 10 mm lasting around 48.5 deg crank angle was introduced. During this period, the intake valve was kept open at the constant 10 mm maximum lift, leading to low friction as the intake valve is stationary. During the whole engine operating range, the conventional valve spring safety factor of 1.4 was maintained.

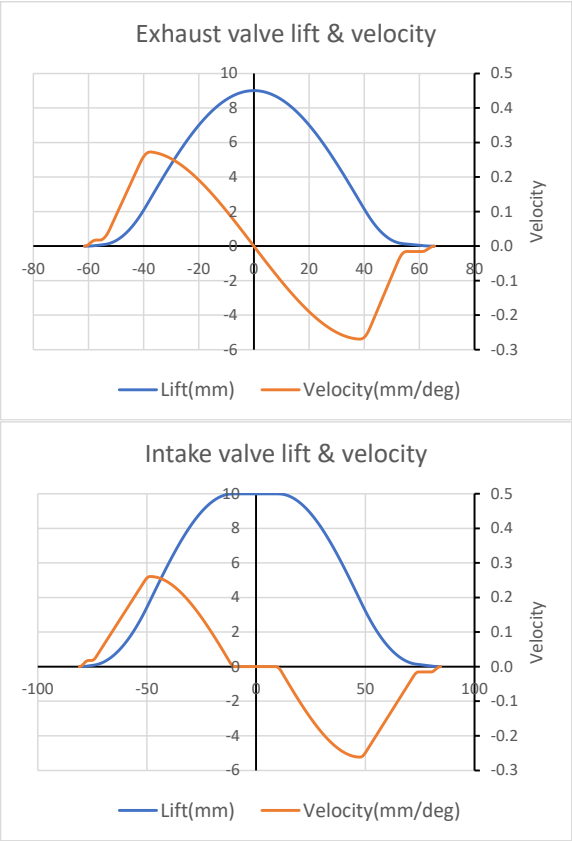

Figure 6: Exhaust & intake valve lift & velocity

Another friction reduction technique with the valvetrain is the use of smaller fuel pump plunger. After sharing the fuel flow map with the fuel system supplier, it was agreed the 6 mm diameter plunger is sufficient for this DHE project. The small plunger not only significantly reduced the fuel pressure loading on tappet but also reduced the inertial loading so a smaller tappet and light spring could be used. Table 2 listed some key design parameters to compare.

Table 2: Fuel pump & tappet parameters

	NE	DHE	Reduction, %
Plunge dia, mm	8	6	25.00
Tappet mass, g	75	49	34.67
Spring preload, N	219	128	41.55
Spring stiffness, N/mm	44.5	18.8	57.75

The main reason a smaller plunger can be used was the fuel flow requirement change (Figure 7). As mentioned before, this DHE has no power/torque requirement below 1200 rpm (Figure 1). Due to the powerful dual e-motor on board, the torque demand at the low speed (<1500 rpm) is much lower than

DOI: https://doi.org/10.26799/cp-sict-plasmatech-tribology-2023

that of the replacement engine. These changes in operating boundary reduced the fuel delivery requirement of the engine. Figure 7 shows the predicted fuel flow of NE14 and DHE. The fuel flow demand of DHE is nearly halved at low speed.

From the Table 2, the 25% reduction is plunger diameter is equivalent to 44% area reduction. This enabled the 49g tappet (35% lighter than that of NE14 fuel pump tappet) to be used. They were matched with 42% lower spring preload and 58% lower spring stiffness. They are all good for friction reduction and durability due to reduced maximum Hertzian stress.

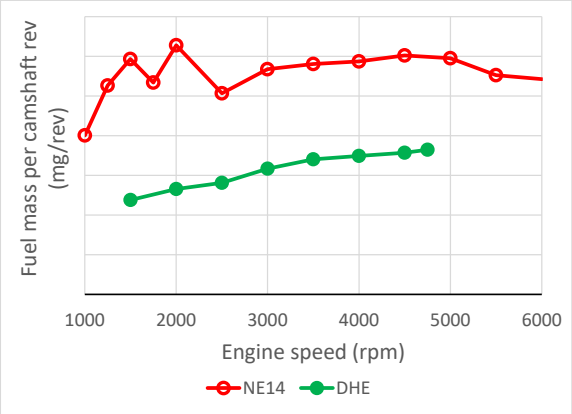

Figure 7: Fuel flow of NE14 and DHE

Figure 8 shows the fuel pump cam lift and velocity curves. This lift curve helped to keep the negative part of the acceleration small so the negative inertial force acting against the spring loading is minimised.

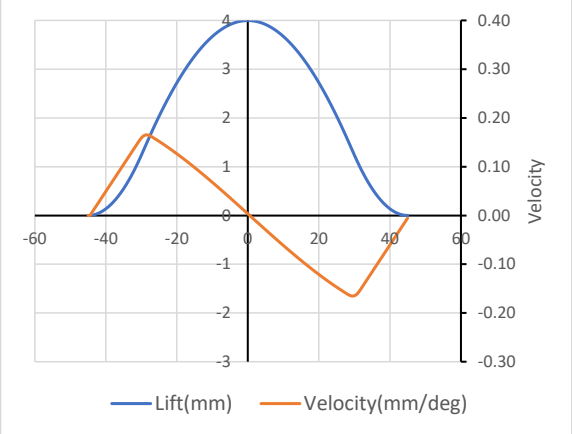

Figure 8: Fuel pump cam lift & velocity

Oil pump and water pump:

Fully variable mechanical vane oil pumps are commonly used to tackle the excessive loss on modern passenger car engines. When optimized, it can significantly reduce the parasitic loss compared with the fixed flow oil pump (vane type or gerotor type). However, as shown in Figure 2, oil pump and water pump combined consumed sizable parasitic loss, typically ~0.1 bar at 2000 rpm.

Nowadays, the use of electric water pump is very common and mature. However, the use electric oil pump is still new. The purpose of using an electric oil pump for this phase of DHE development was (1) to evaluate the suitability of the technology; (2) to gain the performance and pump durability data; (3) to study its impact on friction. It is fair to say that the electric oil pump selected for this DHE project proved to be good sized and performed well. The friction benefit is about 0.04 bar FMEP (Friction Mean Effective Pressure).

DOI: https://doi.org/10.26799/cp-sict-plasmatech-tribology-2023

The other friction reduction related technologies implemented in this DHE included the use of 0W12 oil. The 0W12 oil selected has 20 and 4.2 mPaS dynamic viscosity at 40 and 100 °C respectively. The 0W20 oil used for NE platform had 31.3 and 6.4 mPaS dynamic viscosity at 40 and 100 °C respectively. All the major friction interfaces, such as the main and big engine bearings, cam to RFF roller, RFF to valve stem top, piston ring and skirt to liner, were analysed using the dedicated commercial software FLOAT and all passed the safety criteria.

Friction benefit:
The other powerful function of FLOAT is the friction loss prediction of major friction pairs in internal combustion engine. Since 2000, FLOAT and its predecessor have been used to predict friction loss from piston ring/liner, piston skirt/liner, cam to tappet, cam to RFF, RFF to valve stem top, bearings, fuel pump to tappet and oil pump for many Jaguar and Land Rover, Ford and Changan engines [4-5]. Within engines analysed by FLOAT, there are 4 engines have been measured by FEV using their well-known friction stripped procedures. These four engines are Jaguar and Land Rover 4.4L V8 (AJ41), Jaguar and Land Rover 5.0L V8 (AJ133), Ford 3.0L V6 and Changan NE14 (1.4L I4). Correlations between FLOAT predicted system friction (cranktrain, valvetrain, oil pump etc.) matched well with the FEV measured data [5-6].

Figure 9 shows the FEV friction strip method measured friction of NE14 and FLOAT predicted friction loss at the same operating condition. Based on the good correlation foundation, FLOAT was used again to predict the DHE's friction loss based on the design parameter changes mentioned in previous sections.

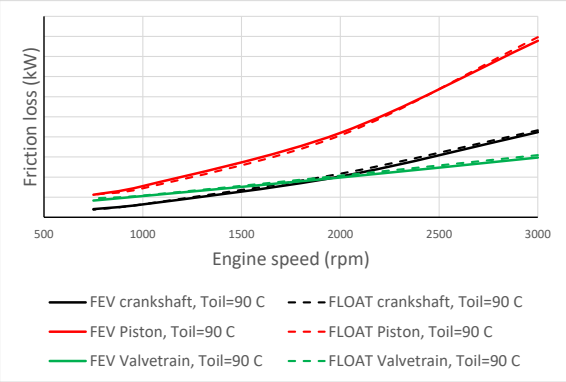

Figure 9: FEV measured and FLOAT predicted NE14 friction loss [6].

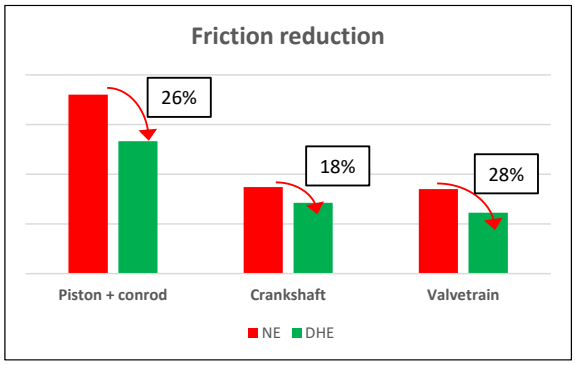

Figure 10: Major friction reduction from moving parts, 2000 rpm

Figure 10 shows the predicted friction from piston + conrod, crankshaft and valvetrain of the production NE14 engine and new DHE. The prediction was done with 0W20 for NE14 and 0W12 oil for DHT at 90 °C, under 2000 rpm motored engine condition but without in-cylinder gas pressure (i.e. FEV friction stripped down method) acting on the piston top.

DOI: https://doi.org/10.26799/cp-sict-plasmatech-tribology-2023

The 26% friction reduction on piston and conrod bearing was mainly due to the lower piston tangential force, smaller big end bearing diameter and low viscosity oil. For the crankshaft alone, the main bearing diameter of NE14 and DHE is same. However, DHE main bearings have lighter loading due to smaller piston diameter. This together with the thinner oil and narrower main bearing helped the friction reduction of 18% from main bearings alone.

For valvetrain, lower loading between cam and RFF roller, lower loading between RFF pad and valve stem top face, and lower loading between fuel pump cam and tappet all helped to drive down the valvetrain friction. As such, the DHE's valvetrain friction decreased by 28% compared with that of NE14 engine.

Adding these changes, plus the use of electric oil pump and electric water pump, the estimated total engine FMEP for DHE is less than 0.29 bar (see Figure 11), making it the lowest friction engine in company's engine portfolio.

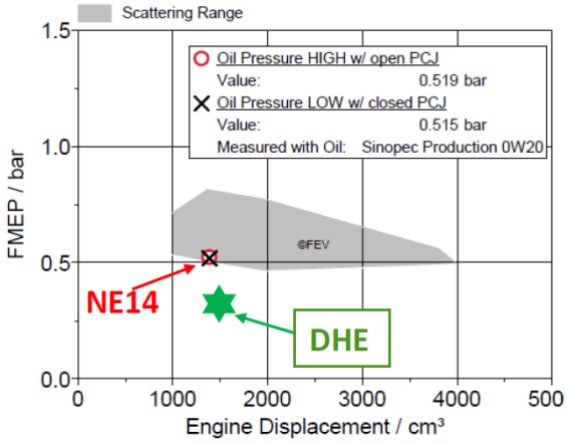

Figure 11: FMEP or NE14 and DHE, O, X for NE14, ★ for DHE

Conclusions:

For the DHE, it is crucial to re-design the moving parts considering the operating boundary changes. In this particular example, following friction benefits were achieved:

- 26% reduction of piston and conrod bearing friction
- 18% reduction of crankshaft main bearing friction
- 28% reduction from the valvetrain
- Replaced the mechanical oil pump with the electrical oil pump
- Replaced the mechanical water pump with the electric water pump
- Successful introduction of 0W12 oil
- Lowest FMEP in company's product portfolio.

Overall, the DHE exceeded designed target of exceptional high brake thermal efficiency. The friction reduction was one of the big enablers. The engine proved durable with no mechanical failure reported during the development process.

References:

1. Branny, S., Gehrke, S., Hoffmeyer, H., Hentschel, L., Blumenröder, K., Helbing, C. and Dinkelacker, F. (2019) Maximum Efficiency Concept of 1.5L TSI evo for Future Hybrid Powertrains, 28th Aachen Colloquium Automobile and Engine Technology, pp99-120.
2. Zhang, G., Wang, Q., Chen, G., de Oliveira, D., Park, J., Wei, M., Zhang, S., Lu, W., Zhao, F. and Scholten, I. (2020) Geely Hybrid Engine: World Class Efficiency for Hybrid Vehicle, 29th Aachen Colloquium Sustainable Mobility, pp65-95.

DOI: https://doi.org/10.26799/cp-sict-plasmatech-tribology-2023

3. Kitadani, H., Kaneda, R., Mizoguchi, S., Shinohara, Y. and Takeuchi, J. (2020) The new 1.5L gasoline engine from TNGA* series, 41st Internationales Wiener Motorensymposium.
4. Zhou, Q. and Richardson, S. (2000) Piston ring pack tribological analysis of Jaguar AJ27 4.0L engine, ASME paper 2000-ICE-336. Proceedings of the 2000 Fall Technical Conference of the ASME Internal Combustion Engine Division, pp1-13.
5. Zhou, Q., Shilling, I. and Richardson S. (2003) Prediction of total engine friction power loss from detailed component models Tribology Series 41, Ed. by Dowson et al.
6. Zhou, Q., Zhang, X. (2018) From Low Friction Concept to Reality–Changan NE14 Engine, *2018 Wuxi ICE Congress, China*